Decentralized Ambient System Identification of Structures

by

Ayan Sadhu

A thesis
presented to the University of Waterloo
in fulfillment of the
thesis requirement for the degree of
Doctor of Philosophy
in
Civil Engineering

Waterloo, Ontario, Canada, 2013

I hereby declare that I am the sole author of this thesis. This is a true copy of the thesis, including any required final revisions, as accepted by my examiners.

I understand that my thesis may be made electronically available to the public.

Abstract

Many of the existing ambient modal identification methods based on vibration data process information centrally to calculate the modal properties. Such methods demand relatively large memory and processing capabilities to interrogate the data. With the recent advances in wireless sensor technology, it is now possible to process information on the sensor itself. The decentralized information so obtained from individual sensors can be combined to estimate the global modal information of the structure. The main objective of this thesis is to present a new class of decentralized algorithms that can address the limitations stated above.

The completed work in this regard involves casting the identification problem within the framework of underdetermined blind source separation (BSS). Time-frequency transformations of measurements are carried out, resulting in a sparse representation of the signals. Stationary wavelet packet transform (SWPT) is used as the primary means to obtain a sparse representation in the time-frequency domain. Several partial setups are used to obtain the partial modal information, which are then combined to obtain the global structural mode information.

Most BSS methods in the context of modal identification assume that the excitation is white and do not contain narrow band excitation frequencies. However, this assumption is not satisfied in many situations (e.g., pedestrian bridges) when the excitation is a superposition of narrow-band harmonic(s) and broad-band disturbance. Under such conditions, traditional BSS methods yield sources (modes) without any indication as to whether the identified source(s) is a system or an excitation harmonic. In this research, a novel under-determined BSS algorithm is developed involving statistical characterization of the sources which are used to delineate the sources corresponding to external disturbances versus intrinsic modes of the system. Moreover, the issue of computational burden involving an over-complete dictionary of sparse bases is alleviated through a new underdetermined

BSS method based on a tensor algebra tool called PARAllel FACtor (PARAFAC) decomposition. At the core of this method, the wavelet packet decomposition coefficients are used to form a covariance tensor, followed by PARAFAC tensor decomposition to separate the modal responses. Finally, the proposed methods are validated using measurements obtained from both wired and wireless sensors on laboratory scale and full scale buildings and bridges.

Acknowledgements

I express my deepest sense of gratitude to my thesis supervisor, Dr. Sriram Narasimhan, for his valuable guidance and encouragement. I wish to thank him for introducing me to the challenging field of research. This dissertation would not have been possible without the support and guidance of Prof. Narasimhan. I would like to express my sincere gratitude towards my co-supervisor Dr. Mahesh Pandey, and my committee members, Dr. Giovanni Cascante, Dr. Scott Walbridge, and Dr. Eihab Abdel-Rahman. I would like to thank Prof. Srinivasan Keshav from the Department of Computer Science and Prof. Guang Gong from the department of Electrical and Computer Engineering for their guidance on wireless sensor issues. I am grateful to Prof. Billie F. Spencer from the University of Illinois-Champaign Urbana, for agreeing to serve on my thesis committee as an external examiner.

Special recognitions are reserved for Dr. Budhaditya Hazra for his valuable suggestions and inspiration throughout this work. I am grateful to Dr. Hazra for his input, and his willingness to help me on various aspects of this research. I would like to express my thanks to Mr. Bo Hu who guided me in developing skills to deal with and to troubleshoot wireless sensors. I would also like to thank the current and former members of the Structural Dynamics, Control, and Identification Group: Dr. Aaron Roffel, Mr. Chad Van der Woude, Mr. Asim Rustum, Ms. Ann Sychterz, Ms. Pampa Dey, Ms. Shilpa Pantula, and Mr. Arun Veeramany, for making my stay an enjoyable learning experience. I express my sincere thanks to my friends Dr. XuFang Zhang and Dr. Jian Deng for their emotional support.

Financial support provided by the Natural Sciences Engineering Research Council of Canada (NSERC) through their Collaborative Research and Development (CRD), Discovery Grants (DG), and NSERC-UNENE programs is gratefully acknowledged.

I take this opportunity to thank my parents, my wife Manashi, and my parents-in-law

for bestowing me with all the patience and courage to undertake this work. Without their love, support and sacrifice, this work could not have been possible.

Dedication

To Manashi, my parents, and my sister Sujata.

Contents

List of Tables

List of Figures

Chapter 1

Introduction

1.1 General Introduction

System identification is an inverse problem, where the primary purpose is to extract system information from measurements. System identification is necessary to undertake tasks such as: (i) to assess the condition of an existing structure to carry out either the performance or safety functions, (ii) to identify and quantify the onset of damage due to extreme hazards such wind-storms, earthquakes, or due to in-service loads and, (iii) for model validation and model updating. In system identification involving dynamically sensitive structures, the system properties such as the natural frequencies and modes are derived using the spectral information regarding the input excitation and the output responses. In many large civil structures, measurement of excitations can be prohibitively difficult, whereas outputs can be measured relatively easily through an a collection of sensors. Extracting system information through the knowledge of output alone is referred to as ambient system identification, or Blind Identification (BI). A majority of BI algorithms in the literature are geared towards centralized processing of measurement data, i.e., processing all the measurement data together in a centralized location. This is both capital-intensive as well

as computationally expensive. Furthermore, the centralized architecture in these methods do not allow us to fully harness the capabilities of next generation wireless sensors. The main objective of this research proposal is to develop novel BI algorithms specifically tailored to harness the power and flexibility of decentralized processing in wireless sensor networks.

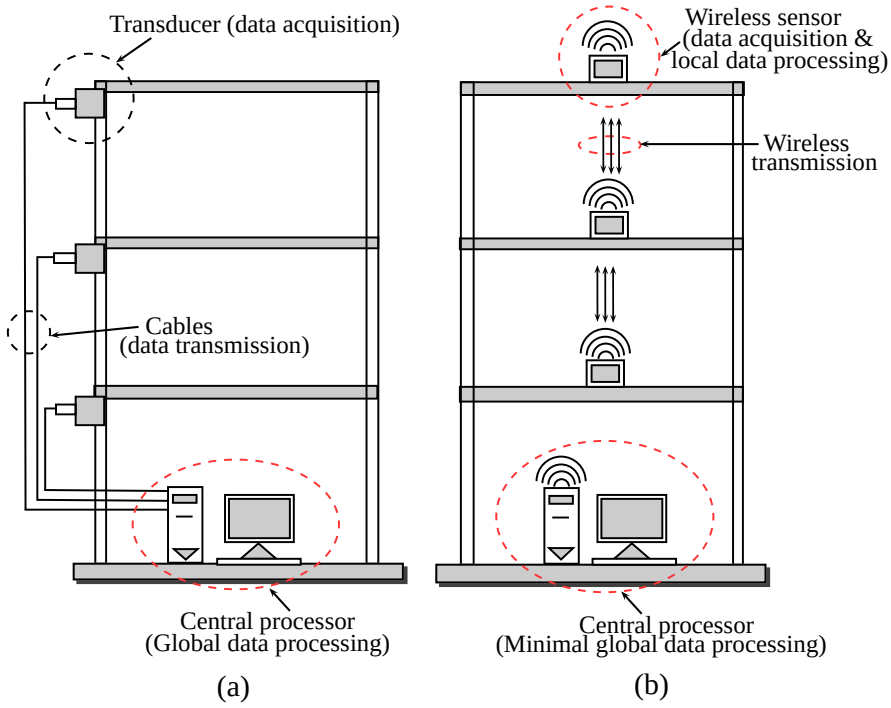

Figure 1.1: Data sensing system, (a) wired network and (b) wireless network

Measurements are an integral component of the system identification process. Traditionally, a measurement system comprises of a large array of sensors distributed throughout the structure. These sensors are connected to a central processing unit via cables, and depending on the size of the structure they can be quite long and expensive to install (as shown in Fig. 1.1(a) and Fig. 1.2). This results in a large amount of data communication and processing at a single location, thereby requiring massive storage, power, bandwidth and computational effort [96]. Despite its robustness, the trade-offs in such a centralized scheme are high cost, massive computations, and installation time. In the event of an earthquake

or other extreme events, the wired links are prone to damage, and hence can result in interrupted data transmission. Advances in wireless technology and embedded processing have resulted in relatively cheap wireless smart sensor networks (WSSNs) (as shown in Figure 1.1(b)). With on-board processing capability, these devices provide a superior alternative to the traditional wired sensing systems [136, 22, 79, 82, 151, 78, 141, 152, 26, 122, 156, 116].

Most of the system identification algorithms in the literature are geared towards centralized batch processing [53, 139, 57, 21, 23, 96]. In other words, the algorithms use the information gathered from all the sensors simultaneously and process them in an unified fashion. Hence, studies utilizing these algorithms for WSSNs have basically used only the wireless capability of WSSNs, without harnessing the processing capability of the sensors [82, 39, 102, 160, 122, 159, 156, 121, 36, 76, 58]. There have been a few attempts to decentralize the aforementioned algorithms to suit WSSNs [160, 159, 122, 121]. However, the process is fraught with computational complexity. There is a clear need to develop new algorithms that are specifically geared towards decentralized implementation, thereby harnessing the local sensor processing capabilities in addition to the wireless transmission of data.

Figure 1.2: Instrumentation issues in wired sensing [56]

At the core of the methods to be proposed for decentralized processing are a powerful class of methods grounded in the concepts of information theory, known as Blind Source Separation (BSS). Unlike purely matrix-decomposition based methods, these meth-

ods (called sparse-BSS) allow the user more control and pre-processing ability to handle vibration data. In doing so, it allows us to overcome the main problem in decentralized processing, namely the issue of underdetermined source separation (described later in subsequent chapters). Other issues pertinent to structures such as the issue of narrowband excitations (e.g., pedestrians in lightweight bridges) are also addressed in this work.

1.2 Objectives

The main objectives of the current research are summarized as follows:

- Develop new algorithms for modal identification of structures, specifically tailored to suit decentralized implementation in wireless networks.
- Address and overcome the mathematical complexities involved in the identification using a truly decentralized implementation.
- Demonstrate the proposed techniques by applying them to both laboratory and full-scale structures.

1.3 Assumptions

The key assumptions in the proposed methods are summarized as follows:

- The system is linear and the law of modal superposition is valid.
- The modes are assumed to be normal and complex modes are not considered.
- The excitation is assumed to be wide-band in nature. However, this condition is relaxed in Chapter 4 where narrow-band disturbances are included within the source of excitation.

- It is assumed that the external disturbance harmonics are well separated from the resonant frequencies of the system. Thereby the effect of resonance is excluded.

1.4 Organization

This thesis contains seven chapters and is organized as follows:

1. **Chapter 1** provides a brief introduction to the basic ideas of this thesis, along with a summary of research objectives.

2. A detailed background on the various methods of system identification, specifically related to modal identification is presented in **Chapter 2**. Traditional modal identification methods are reviewed first, followed by the more recent ones which belong to the family of BSS methods. The concept of decentralized sensing network is reviewed next. During the course of relevant literature review, the basic demerits of the traditional and modern modal identification methods as applied to decentralized sensing are highlighted to underscore the importance of the proposed research.

3. **Chapter 3** presents the theoretical development of a new BSS method for structural system identification using partial measurements. The method is developed based on concepts of sparsity with the aid of wavelet packet transform and principal component analysis. The proposed method is illustrated with the aid of a numerical example.

4. A novel sparse BSS method is developed in **Chapter 4** to delineate modal harmonics in the presence of narrowband external harmonics. Time-series analysis based statistical characterization is employed to separate the disturbance harmonics from the sparse wavelet packet coefficients and retain the modal responses.

5. In order to increase the computational efficiency of the proposed sparse BSS method presented in Chapters 3 and 4, a novel tensor algebra based tensor decomposition

in conjunction with sparse BSS method is proposed in **Chapter 5**. The proposed method is illustrated with a suite of simulation models.

6. **Chapter 6** presents experimental validation of the proposed decentralized modal identification methods using ambient vibration data from UCLA Factor building and a pedestrian bridge located in Montreal, Canada. The details of the wireless sensor network is presented first followed the identification results.

7. Finally, the main conclusions from this work are discussed in **Chapter 7**. Several recommendations for extending the present work are also discussed. Finally, a list of publications resulting from this work are included.

Chapter 2

Background

In this chapter, several popular system identification techniques are reviewed in the context of modal identification of structural and mechanical systems. The conventional methods are presented first, followed by the more recent ones belonging to the family of Blind Source Separation (BSS) methods. Basic ideas and key features of these methods are discussed, followed by their merits and demerits in the context of the decentralized system identification. A brief overview of wireless sensor networks is introduced, and their recent applications in the field of system identification are reviewed.

2.1 Traditional System Identification Methods

Since early 1970's, various modal identification techniques [84] have been developed for structural and mechanical systems. Most of these methods operate either in the time or in the frequency domain. Gradual technical developments in these methods progressed from single-input single-output (SISO) systems to single-input multiple-output (SIMO) systems and finally to the general case of multiple-input multiple-output (MIMO) systems. Various popular time domain methods are reviewed first, followed by the frequency domain

techniques.

Of all the time-domain methods [125, 53, 61, 139, 57, 4], complex exponential (CE) algorithm based on Prony's method [125] is perhaps the first important parametric identification technique for a SISO system. The basic premise of this method is to extract frequencies and damping from a uniformly sampled signal using impulse response functions (IRFs) by creating a series of damped complex exponentials, or sinusoids. A combination of CE algorithm with least-squares (LSCE) is available for SIMO systems [4].

Extending the concept of Prony's method, Ibrahim time domain (ITD) method [53] was proposed for SIMO systems. Instead of using the IRFs, the ITD method uses free acceleration responses to estimate the modal parameters. However, this method is computationally expensive and the appropriate choice of model order is one of its key prerequisites. The ITD method in conjunction with random decrement technique (RDT) [9] was implemented for the modal identification of structural systems [74]. Poly-reference CE technique [4] was formulated as an extension of the LSCE algorithm. This was perhaps the first general identification technique for a MIMO system. This method reduces the possibility of mode-missing when a node of the structure is excited.

Eigensystem realization algorithm (ERA) [61] was developed based on the general state-space description using the IRFs of a linear dynamic system. This algorithm is an extension of system realization theory. The modal parameters are estimated using the eigen-value decomposition of the Hankel matrix formed by the IRFs. However, the method is limited by the need to obtain free or impulse responses of the structures, which is not always feasible in civil engineering applications due to size, safety concerns and the continuous presence of ambient vibrations. To overcome this limitation, Natural Excitation Technique (NExT) [57] was developed. This technique demonstrates that, when forced vibration data are available the cross-correlation functions between the response measurements and a single reference measurement satisfies the homogeneous differential equation of motion

and therefore, can be treated as free responses. In the recent-past, NExT in conjunction with ERA was successfully applied for structural system identification [21, 23, 96].

Stochastic Subspace Identification (SSI) method, developed in the early to mid 1990′s [139, 140], provides a powerful means of output-only system Identification. Linear stochastic state space system is used as the framework of the SSI method. This method performs particularly well when the number of outputs is relatively large [123]. However, this technique is computationally expensive and time consuming. The use of stability diagrams and modal assurance criteria further affect its suitability for onboard processing in a decentralized setting. The separation between numerical and stabilized frequencies may require a great deal of expertise and user discretion, which is cumbersome for on-line applications.

Unlike time domain techniques, frequency domain methods [111, 153, 17] are based on frequency response functions (FRFs). Ewins-Glesson method and rational fraction polynomial based method [111] were primary developed for SISO systems. The SIMO based frequency domain technique was proposed using the concept of differential FRF. In the same year, another classical method such as power spectral density (PSD) based peak picking (PP) [153] was developed. However, this technique was found to be inaccurate, especially in estimating the mode shapes and damping ratios.

A new frequency domain technique, called frequency domain decomposition (FDD) [17] was developed to resolve the difficulties encountered in peak picking, while retaining the advantages of the classical PP method. This technique is user-friendly in terms of simplicity and processing speed. However, due to averaging of temporal information, often some details are discarded. In case of heavily damped systems with closely spaced modes, there is a possibility of obtaining unreliable damping estimates. Moreover, picking peaks is a subjective task. The classical FDD was extended [19] to identify symmetrical structures with closely-spaced modes, however the user-discrimination and standard issues associated with FFTs are still present.

In most modal identification methods, the excitation is assumed to be broadband [91, 7, 92, 106, 6, 32, 90, 110]. This means that the identified sources are certain to belong to the modal harmonics. However, if disturbances themselves contain narrow-band frequencies, the excitation harmonics are also identified along with the structural modes. Such a presence of excitation harmonics in structural vibration measurements occur in mechanical systems with rotating machineries, e.g., engines, motors, windmills and turbines [8, 106, 108], in civil structures such as gravity dams comprising of turbines and generators [6], human-induced narrow-band vibrations in pedestrian bridges [11, 38, 98, 55], and when dynamic interactions with surrounding structures exist in buildings [110]. The issue of excitation harmonics contaminating ambient vibration results has previously been dealt with in the literature, e.g., [91, 92, 106, 6, 32, 90, 110]. The harmonic frequency is assumed to be known *a priori* in many of these methods [91, 92, 106, 6]. Recently, an algorithm applied to the random decrement method was proposed in the context of delineating harmonics from modal components [90]. The conditional probability density function is used to estimate the harmonic sources by the author, and was shown to perform well within the random decrement framework. Delineating excitation harmonics from source harmonics has also been dealt with in the context of signal processing [120, 154], where a modified principal component analysis is introduced. The underlying architecture in all these methods involves batch processing of sensor measurements, i.e., in a centralized architecture, where the number of measurements is more than the number of sources to be identified. This requires the measurements from a number of sensors to be processed together in order to identify the modes. To the knowledge of the author this problem has not been addressed in decentralized settings.

2.1.1 Drawbacks and Limitations of the Traditional methods

1. Most of the traditional techniques are based on the premise that the sensor measurements are available at all key locations, and the data are processed centrally (a few variations exist, which will be discussed later). In such methods, the cost of instrumentation and processing increases with the increase in sensor density and complexity of the algorithms. Moreover, it is not always feasible to achieve full measurements due to cost and installation reasons in the traditional sensing system, or due to communication issues in WSSNs.

2. One of the key pre-requisites of previously described identification algorithms (ITD and SSI) is the model order pre-selection. In order to achieve a suitable model order, additional information in terms of stability charts and modal assurance criteria are needed. This process is computationally expensive and time consuming, and hence not suitable for on-line implementations. Over-determination of model order generates spurious modes, which is a serious issue when dealing with noisy response data.

3. While computationally faster and user-friendly, FDD method is unable to perform well in high damped systems with closely spaced modes. This situation commonly arises in flexible tall structures equipped with supplemental devices such as tuned mass dampers (TMDs). Due to averaging of the temporal information, some details are implicitly discarded. Moreover, the peak peaking technique in FDD is a subjective task and requires a great deal of user experience.

4. Majority of output-only modal identification methods (e.g., ITD, SSI and FDD) assume that the underlying excitation is white and does not contain narrow band excitation frequencies. However, this assumption is not satisfied in many practical situations when the excitation is a superposition of narrowband harmonic(s) and broad-

band disturbance, e.g., rotating machinery fixed to flexible structures, human incited vibration in pedestrian bridges, or dynamic interaction with surrounding structures. Due to contamination of such external harmonics, it becomes difficult to delineate narrowband harmonics from the inherent modal responses of structures.

2.2 Modern Schemes in Inverse Problems

In last decade, significant advances in information theory and signal processing have led to the development of powerful system identification and time-frequency analysis tools. Empirical Mode Decomposition (EMD) [50] is a versatile signal processing algorithm that has shown significant promise in the area of output only system identification of structures in non-stationary environments [147, 146, 46, 113, 135]. EMD reduces a signal into intrinsic mode functions (IMFs) that admit a well-behaved Hilbert transform [50]:

$$\ddot{r}_p(t) = \sum_{j=1}^{m} c_{pj}(t) + \epsilon_p(t) \tag{2.1}$$

in which $c_{pj}(t)$ for $j = 1, 2, ..., m$ are the m IMFs of the free acceleration response $\ddot{r}_p(t)$ of any dynamical system and $\epsilon_p(t)$ is the residue. The power of EMD lies in its decomposition capability, even in non-stationary environments, in an adaptive manner without the need of choosing a predetermined basis. Recently, a new ensemble EMD (EEMD) [144] was proposed to eliminate the need for prior intermittency selection criteria, which is a source of difficulty in the original EMD.

Blind Source Separation (BSS) is a powerful tool that is extensively used in speech and audio processing [28]. BSS allows for a set of linearly mixed sources (static or convolutive) to be recovered solely from their observed mixtures. Interestingly, this is achieved without any knowledge about the mixing process [13, 52, 28], thereby eliminating the need of any system information except the output. This concept was utilized in inverse problems

related to ambient structural system identification [7, 62, 109, 44, 45, 46, 48, 47]. A brief description of various approaches based on BSS are reviewed in the next section.

2.3 Blind Source Separation

The separation of original source waveforms from their observed mixtures, without the knowledge of system information and the sources, is known as BSS. For most applications, the sources are related to mixtures by simple linear mixing models. This principle is illustrated in Fig. 2.1. Depending on the specific application, the mixing processes of the unknown input sources may have different mathematical or physical models. In general, there are two ways to represent the mixing of sources: (a) static or instantaneous and (b) dynamic or convolutive. In both the instantaneous and convolutive mixture models, BSS methods aim to recover the un-mixing matrix and the corresponding sources using the information contained in $\mathbf{x}$ only, without knowing the mixing system. Hence, the term *blind* is commonly used.

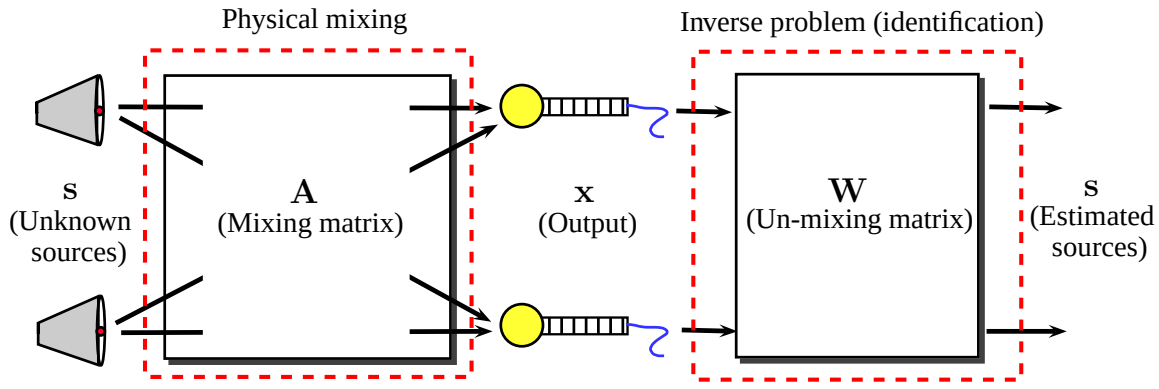

Figure 2.1: Illustration of BSS

Instantaneous mixing

The instantaneous mixing model is the most rudimentary model where sources arrive instantly at the sensors but with differing signal intensities, and is expressed as:

$$\left.\begin{aligned} \mathbf{x}(k) &= \mathbf{A}\mathbf{s}(k) \\ \hat{\mathbf{s}}(k) &= \mathbf{y}(k) = \mathbf{W}\mathbf{x}(k) \end{aligned}\right\} \tag{2.2}$$

- $\mathbf{s}(k) = \{s_j(k)\}$ $j = 1, 2, ...n_s$ actual sources (system input)
- $\mathbf{x}(k) = \{x_i(k)\}$ $i = 1, 2, ...n_m$ sensor measurements (system output)
- $\mathbf{y}(k) = \{y_j(k)\}$ $j = 1, 2, ...n_s$ estimated sources
- n_m and n_s are the total number of measurements (sensors) and sources respectively.
- $\mathbf{A} = [a_{ij}]_{n_m \times n_s}$ is the instantaneous mixing matrix
- $\mathbf{W}_{n_s \times n_m}$ is the un-mixing matrix, which is obtained by the pseudo-inverse of $\mathbf{A}$ (if $n_m > n_s$) or by a matrix inversion of $\mathbf{A}$ (if $n_m = n_s$)

Eq. 2.2 represents the static mixing problem ($x_i(t) = \sum_{j=1}^{n_s} a_{ij} s_j(t)$), which does not explicitly use time properties. Therefore, it is not necessary for the sources and the outputs to be a function of time.

Convolutive mixing

In the instantaneous mixing case, an important assumption is that there are no time delays involved in the mixing of independent signals. This model is useful for certain applications such as modal identification using wired sensors, but becomes unrealistic when applied elsewhere, e.g., acoustic environments, wireless channels [132, 100, 72]. An obvious case in which it is necessary to account for time delays in signal mixing is in the separation

of speech signals recorded in a real environment. Sound wave propagation is relatively slow and the waves are subject to reflections so that time delays are introduced in the mixing process. To separate sources mixed in this fashion, a technique called convolutive BSS [60, 150, 100, 101, 117] was developed which extends the standard instantaneous BSS model by treating signal mixing as a convolution, allowing time delays to be accounted for. A convolutive model can be of two types *echoic* or *anechoic*.

An echoic convolutive mixture can be expressed as:

$$x_i(t) = \sum_{j=1}^{n_s} \left(\int_{\infty}^{\infty} a_{ij}(\tau) s_j(t-\tau) d\tau \right) \tag{2.3}$$

Eq 2.3 represents a dynamic problem where the sources and the outputs have well defined time properties and the coefficients of the un-mixing system are essentially the coefficients of a deconvolution filter (e.g., finite impulse response (FIR) filter). It is obvious that the instantaneous mixing model is a special case of the convolutive model, where the filter coefficients are constrained to be proportional to delta function $a_{ij}(t) = a_{ij}\delta(t)$. Compared to the echoic (full convolutive) model, anechoic mixture model linearly combines time-shifted and scaled versions of the sources, without permitting multiple occurrences of the same source in the mixture. These models are equivalent to convolutive models for which the filter kernels are constrained to the form $a_{ij}(t) = a_{ij}\delta(t - \tau_{ij})$ [101], resulting in the equation:

$$x_i(t) = \sum_{j=1}^{n_s} a_{ij} s_j(t - \tau_{ij}) \tag{2.4}$$

In time domain, it is similar to the instantaneous mixing model but now the source signals are shifted by the delay terms. Thus the anechoic mixing model describes the convolution of each source signal with a simple delay and attenuation term, i.e., this model describes the propagation of source signals upon single non-dispersive paths to each of the sensors and neglects the existence of any reflective paths (as in the echoic model). A summary of

various linear operators and mixing matrix components specific to the different types of mixing cases of blind source separation is presented in Table 2.1. For the purposes of this thesis, we will restrict ourselves to the instantaneous mixing model.

Table 2.1: Linear operator and mixing parameters of different types of BSS mixing

Mixing	**Linear operation**	**Mathematical model**	**Mixing coefficient**
Instantaneous	Matrix multiplication	$\mathbf{x}(t) = \mathbf{A}\mathbf{s}(t)$	$a_{ij}\delta(t)$
Anechoic	Delay	$\mathbf{x}(t) = \mathbf{A} * \mathbf{s}(t)$	$a_{ij}\delta(t - \tau_{ij})$
Echoic	Convolution	$\mathbf{x}(t) = \mathbf{A} * \mathbf{s}(t)$	$\sum_{k=1}^{L} a_{ij}^{k}\delta(t - \tau_{ij}^{k})$

At present, there exists a variety of BSS algorithms for the instantaneous mixing model depending on their potential applications, such as in speech processing, digital communication, or biomedical processing [28]. They can be categorized using the following three properties.

1. Second-order (temporal structure) or higher-order (mutual information) statistics of sources.

2. Sparse representation of sources achieved through transformations (typically, time-frequency).

3. Tensor decomposition based source separation.

The first category belongs to *non-sparse* methods, the second one to *sparse* methods [100], whereas the last one involves a powerful multi-linear algebra tool, i.e., *parallel factor* (PARAFAC) decomposition [43, 24, 20]. The non-sparse methods are usually implemented when $n_m \geq n_s$, and primary based on statistics of the signals. On the other hand, underdetermined problems ($n_m < n_s$) are pursued with the aid of sparse methods, and is based on the structure of the mixtures. The PARAFAC BSS methods are applicable to both over-determined as well under-determined problems with some restrictions. In non-sparse methods, the higher order statistics based independent component analysis (ICA)

[52] exploits the marginal non-Gaussianity and statistical independence of sources without using the time structure of sources. On the other hand, second order statistics-based second-order blind identification (SOBI) [13] utilizes multiple co-variance matrices of the responses, for the case when the sources are spatially uncorrelated but temporally correlated [28]. Recently, the concept of BSS has been extended to the ambient system identification of structural systems [7, 109, 62, 44, 45, 48, 47]. A brief overview of non-sparse, sparse, and PARAFAC BSS methods is presented next followed by the recently developed BI [46, 48, 47, 112, 149, 148] techniques for structural systems.

2.3.1 Non-sparse BSS

Independent component analysis (ICA) is one of the most popular non-sparse BSS methods in the literature [31, 12, 52]. This method assumes that the observed data are linear combinations of statistically independent (or as independent as possible) sources. The sources are termed as independent components (IC's), and the ICA basis vectors are the ICA modes, which are linearly independent. The independence is measured by an information-theoretic cost function such as minimization of mutual information [31] or maximization of entropy [12] or maximization of non-gaussianity [52]. In terms of application, ICA is simple and straight forward. It has been observed that ICA fails to perform adequately in the presence of even relatively small amounts of damping [62, 45].

Second order BI (SOBI) [13] based methods use the time information contained in the signals, as opposed to treating them as mere random variables, as in ICA. If the ICs are time signals, they usually contain a much better defined structure than ordinary random variables. For example, the auto-covariances for several time lags have well-defined statistics. The SOBI family of methods do not make any prior assumptions regarding statistical independence or non-gaussianity of sources. They rely purely on second-order temporal statistics. The basic assumptions include full rank of the matrix $\mathbf{A}$, existence of

autocorrelation function of the sources, spatial non-correlation of the sources, stationarity of the sources, and the presence of independent noises.

SOBI estimates the mixing matrix using simultaneous diagonalization of several covariance matrices with different time lags. The performance of SOBI in identifying simple systems has been clearly demonstrated [109, 155]. SOBI holds lot of promises in modal identification in presence of moderate to high damping. Unlike higher-order statistics based ICA, second-order statistics based SOBI is much more simpler to implement. However the performance of SOBI is affected by the presence of low energy modes. A prior knowledge of noise covariance is one of the prerequisites of SOBI, which could be difficult to achieve in practical applications.

An extension of SOBI —Modified Cross-Correlation method (MCC) —was developed [44, 45] in order to eliminate the short-comings of the traditional SOBI method. MCC method deviates from SOBI in two key respects: (i) whereas SOBI method operates directly on the responses (measurements) $\mathbf{x}(t)$, the MCC method operates on the correlation of the responses (vector, $\mathbf{r}(t)$) calculated at all time lags; (ii) whereas the diagonalization procedure in SOBI involves several time-lagged covariance matrices of the responses, covariance matrices obtained from multiple non-overlapping windows are used in the MCC method [44]. As in SOBI, the noise variance needs not be known *a priori*, which is an additional advantage in using the MCC method [45]. Recently an improved version of SOBI is proposed [112] by the author indue to earthquake applications.

A key assumption in the MCC method is that the number of outputs is greater or equal to the number of identifiable modes. In order to address this issue, a hybrid approach combining the MCC with the EMD was proposed [47, 48]. This is accomplished in two stages; (i) extracting the intrinsic mode functions (IMFs) using the EMD and, (ii) treating the IMFs as pseudo-sources in an iterative procedure within the framework of the MCC method. The major advantage of this approach is that the estimated mode-shape matrix is

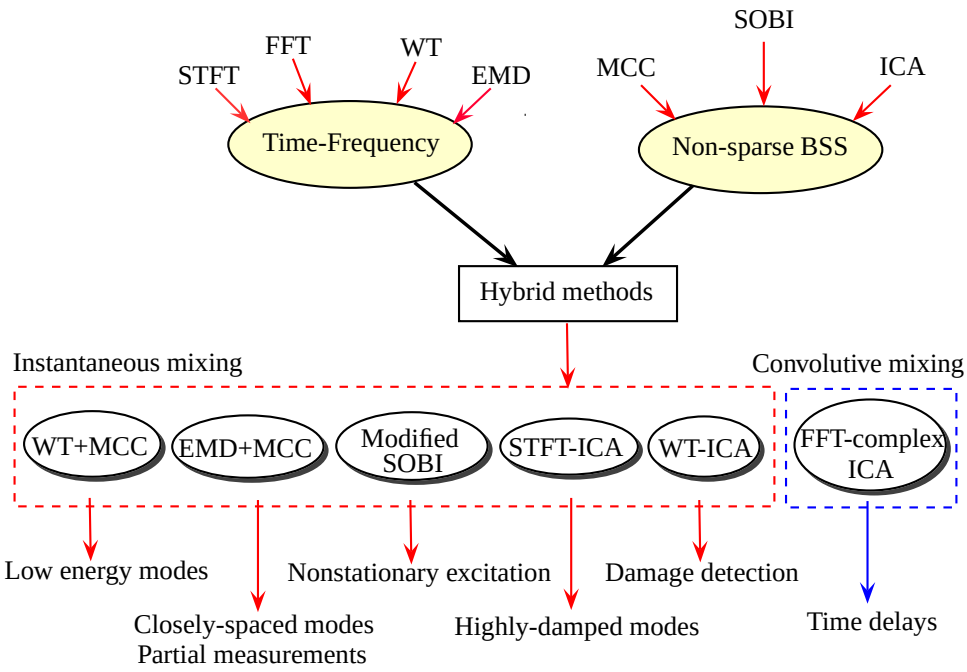

Figure 2.2: Summary of non-sparse BSS methods

square and spatially dense. However, an initial estimate for the mixing matrix is assumed using shape functions that satisfy the prescribed boundary conditions for the problem, and this estimate is adjusted iteratively based on an energy criterion [47].

Another hybrid approach [46] in conjunction with the EMD and the MCC was recently proposed for blind identification in special cases of structures equipped with TMDs. In this approach, EMD is first utilized to separate the closely-spaced modes, and then the remaining modes are separated using MCC method. However, this approach uses an interpolation based technique for estimating the mode shapes, which is cumbersome to implement on WSSNs. Recently another family of hybrid BSS methods employing ICA are proposed in conjunction with time-frequency transformation to deal with highly-damped modes [149] and time-varying systems [148]. All the hybrid non-sparse BSS methods are summarized in Fig. 2.2.

2.3.2 Sparse BSS

Estimating modal information for the full-rank case of Eq. 2.2 is well-known [13, 7, 62, 45, 46, 112, 149, 148]. The BSS problem applied in the context of partial measurement results in the under-determined case, i.e., $n_m < n_s$ (i.e., $\mathbf{A}$ is non-square) [15, 158, 66, 2]. Hence, $\mathbf{A}$ is non-invertible, and estimating $\mathbf{W}$ and $\mathbf{s}$ is fraught with difficulties. One way to deal with the under-determined case is to assume that under frequency or time-frequency transformations, the signals can be transformed using a *sparse* basis (sources). Consequently, when the sources are sparse, a majority of data will be aligned along the direction of basis vectors, where the directions of the maximum data density will yield the partial modal information. Therefore the essence of the sparse approach is the identification of line of orientation vectors (also termed as basis vectors) from the mixtures.

Clustering using topographic maps [51] is a popular approach in sparse BSS methods. In image processing, feature detection techniques [75] using Hough transform have also been used to locate line of orientations. The estimation of mixing matrix and sources of speech signal was achieved [158] based on maximum a posteriori and maximum likelihood estimation. A fuzzy-C-means clustering approach [157] was also used to exploit sparseness of speech in the wavelet domain. This multi-scale method provides a number of different classes of coefficients that represent the same signal. The selection of the most appropriate class is determined by the sparsity of the coefficients. Kernel based L_1 norm minimization approach [33] is another clustering approach for the speech signals. Recently, several algorithms for achieving sparsity in the transformed domain, such as wavelet transforms [66, 73] and short-time Fourier transform (STFT) [2, 3], have been proposed. All these algorithms are primarily developed for image or acoustic signals.

The essence of sparse separation is to perform identification in a transformed signal space (e.g., Fourier, wavelet) such that the sources are rendered sparse by the transformation, with at most one source active at any time [15, 158]. Notion of sparsity can be easily

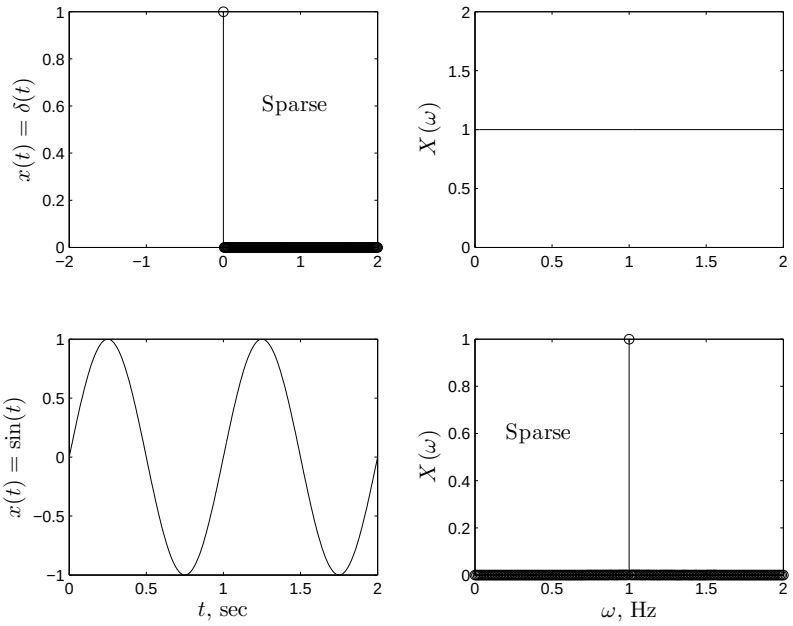

Figure 2.3: Notion of sparsity

understood through a simple example as shown in Fig. 2.3, where two signals namely impulse and sine wave are considered. It is seen that the impulse function is sparse in the time domain with a non-zero value only at $t = 0$. On the other hand, the sine wave is dense in time domain. However when we transform the sine wave from time to the frequency domain, it appears to be sparse in frequency domain. Therefore the notion of sparsity can be achieved through an appropriate time-frequency transformation.

Sparsity is typically difficult to achieve in ambient system identification problems. For very lightly damped and flexible structures, sparsity is difficult to realize. Furthermore, low energy and substantial measurement noise present difficulties in delineating in the Fourier domain. Unlike image or speech signals, damping in the structural response introduces an additional level of complexity. Hence, several clustering techniques developed in speech processing literature [15, 73, 2, 100, 65] cannot be used directly for the problem of ambient system identification. Recently, a time-frequency decomposition procedure based on STFT to achieve sparsity was proposed in the literature [3]. This algorithm was subsequently

applied to structural system identification [25] with good results. In this paper, the authors search the time-frequency space to determine the coordinate where only one source is active. The eigen-value decomposition of the spectral data at this instant then allows them to calculate the partial mixing coefficients. For low frequency systems, achieving sparsity may be computationally expensive; the next section on PARAFAC is relevant in this context.

2.3.3 PARAFAC Decomposition

When a signal is expressed as a multi-dimensional array, then its tensor representation allows the use of multi-linear algebra tools, which is more powerful than linear algebra tools [124]. A vector $\mathbf{t} = t_i \in \Re^{n_1}$ is a first-order tensor, whereas a matrix $\mathbf{T} = t_{ij} \in \Re^{n_1 \times n_2}$ is second-order tensor. In general a p^{th} order tensor is written as:

$$\underline{\mathbf{T}} = t_{ijk\ldots p} \in \Re^{n_1 \times n_2 \times n_3 \times \ldots \times n_p} \tag{2.5}$$

A third-order tensor is primarily decomposed into a sum of outer products of triple vectors as shown in Fig. 2.4 [124]:

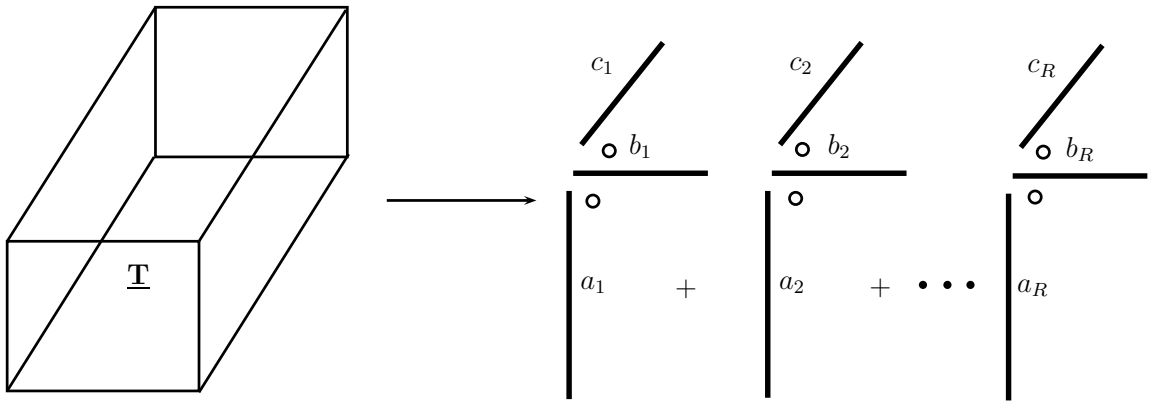

Figure 2.4: Tensor decomposition

$$\underline{\mathbf{T}} = \sum_{r=1}^{R} \mathbf{a_r} \circ \mathbf{b_r} \circ \mathbf{c_r} \Longleftrightarrow \underline{T}_{ijk} = \sum_{r=1}^{R} a_{ir} b_{jr} c_{kr} \tag{2.6}$$

where $\circ$ represents outer product and $i \in [1\ \mathrm{I}]$, $j \in [1\ \mathrm{J}]$ and $k \in [1\ \mathrm{K}]$. This is termed as a trilinear model of $\underline{\mathbf{T}}$, $\underline{\mathbf{T}} = [[\mathbf{A}, \mathbf{B}, \mathbf{C}]]$, where the matrices are given by $\mathbf{A} = (\mathbf{a_1}, \mathbf{a_2}, ..., \mathbf{a_R})$, $\mathbf{B} = (\mathbf{b_1}, \mathbf{b_2}, ..., \mathbf{b_R})$, and $\mathbf{C} = (\mathbf{c_1}, \mathbf{c_2}, ..., \mathbf{c_R})$. Therefore, Eq. 2.6 represents the summation of R rank-1 tensors or PARAFAC components that are needed to fit the tensor. PARAFAC components are usually estimated by minimization of the quadratic cost function:

$$g(a, b, c) = \|\underline{\mathbf{T}} - \sum_{r=1}^{R} \mathbf{a_r} \circ \mathbf{b_r} \circ \mathbf{c_r}\|^2 \tag{2.7}$$

This technique was introduced in two different works; canonical decomposition (CANDECOMP) [24] or parallel factor analysis (PARAFAC) [43]. The algorithms fitting the PARAFAC model are usually classified in three main groups [138]: (a) alternating least squares (ALS), which updates only a subset of parameters at each step; (b) derivative-based methods; which seeks an update for all the parameters simultaneously by successive approximations, and (c) direct or non-iterative approaches. Out of these, ALS method has several advantages, including easier implementation, guaranteed convergence, and better handling capability of higher order tensors [138]. Finally the algorithm finds a tensor $\hat{\underline{\mathbf{T}}} = \sum_{r=1}^{R} \mathbf{a_r} \circ \mathbf{b_r} \circ \mathbf{c_r}$ such that Eq. 2.7 is satisfied. A unique decomposition is obtained if the following Kruskal condition [68] is satisfied:

$$k_A + k_B + k_C \geq 2R + 2 \tag{2.8}$$

where k_A, k_B and k_C are the $k-$rank of the matrices $\mathbf{A}$, $\mathbf{B}$ and $\mathbf{C}$ respectively (k-rank is defined as maximum number k such that every set of k columns of the matrix is linearly independent [68]). PARAFAC decomposition can be used within the context of sparse BSS to reduce the computational burden associated with source separation, as will be described

in later chapters.

2.4 Sensor Networks

Sensors are the key components in the distributed identification methods being proposed here. Traditional sensors are wired with physical connections between the sensing unit and the data acquisition system. Recent developments in the area of MEMS and wireless technologies have resulted in self-contained distributed wireless networks. In the present section, traditional centralized sensing systems and the more recent smart decentralized (distributed) sensing systems are reviewed within the context of BI.

2.4.1 Traditional Centralized Sensing System

Most of the popular system identification methods [53, 139, 57, 74, 21, 147, 23, 83, 96] described in previous sections utilize measurements that are simultaneously collected from a dense array of sensors, and processed centrally off-line. In such a setting, all the key locations on the structure are instrumented with sensors, and connected to a central processing unit using coaxial cables. This setup involves a global processing unit, called a centralized data repository (CDR). This centrally off-line wired sensing system is commonly known as *centralized* (global) sensing system [78, 96]. In this system, measurements are collected first by the data acquisition system at sensor nodes, then transmitted simultaneously to the CDR from all the sensors using cables. Finally, the central processor performs the data processing tasks.

In large civil structures, using long cables to communicate sensor measurements to the central processor involve high cost, labor-intensive installations and time [122]. Moreover, the central processor deals with the global measurement of all sensors, thereby requiring massive storage, power, bandwidth and computational effort [96]. In locations with

extreme weather conditions as in North America, the cost associated with large scale monitoring systems is generally higher as a result of their size and the need to place cables in weatherproof conduits [78]. As reported in some studies, nearly 25% of the total system cost and 75% of the total installation time can be attributed to cable installations [130]. For a large inventory of systems, such as a portfolio of bridges, alternate means of rapid modal assessment is required, one that can be performed rapidly with minimum installation effort.

2.4.2 Modern Decentralized Sensing Systems

Wireless Smart Sensor Networks

Recent advances in Micro-Electro-Mechanical system (MEMS) has enabled low cost wireless smart sensor networks (WSSNs) to be seriously considered as an attractive alternative to wired data acquisition systems. In fact, a WSSN is an intense network consisting of intercommunicating tiny computers equipped with MEMS sensors. Each tiny computer represents a node of the network and is denoted as sensor nodes or motes. The communication within the network is established using powerful radio frequency transmission protocols.

A typical wireless sensing unit primarily includes three subsystems [80, 143] (see Fig. 2.5).

1. The sensing interface (converts an analog signal to digital form).
2. Computational core, or an on-board microprocessor (digital data processing and local storage).
3. Wireless communication system (data transmission with other sensors or a data server).

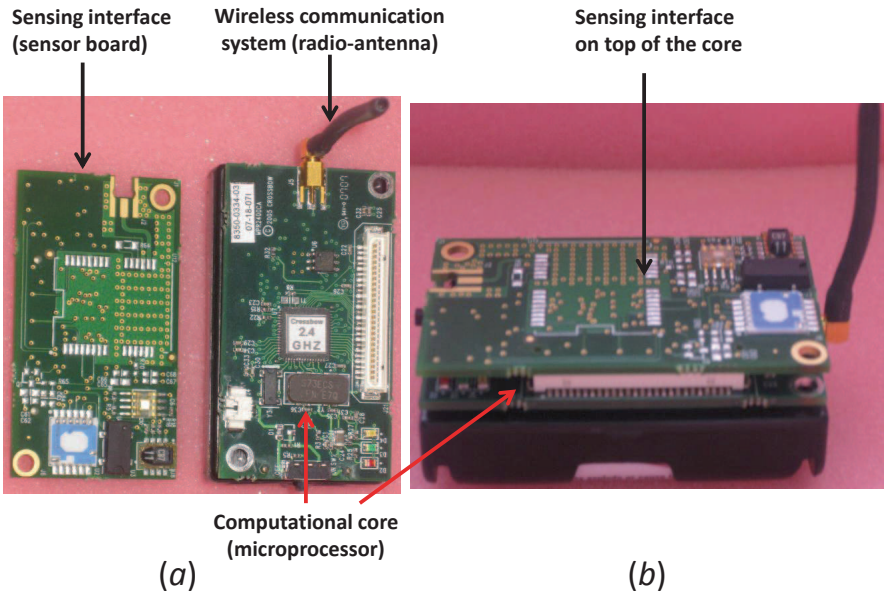

Figure 2.5: Three subsystems of a wireless sensor (a) sensing interface, core and wireless communication system, (b) assembly of three subsystems

In particular, a sensor node in WSSN performs the local data acquisition, data processing, and communication with other nodes in the network and a central base station (see Fig. 2.6).

A variety of commercially available motes (i.e., micaZ [102, 54], wireless modular monitoring system (WiMMS) [81, 82, 26, 159], Narada sensors [133], iMote2 [121, 76] or Lotus motes [89, 119]) have been recently used in several structural health monitoring applications. WSSNs can remedy the cabling problem of the traditional monitoring system and significantly reduce the maintenance cost associated with cabling [130]. Therefore, WSSNs provide a promising alternative to traditional wired sensor networks. However, WSSNs face a unique set of challenges, often not found in traditional wired networks. The advantages and the challenges in using WSSNs are discussed in the ensuing sections.

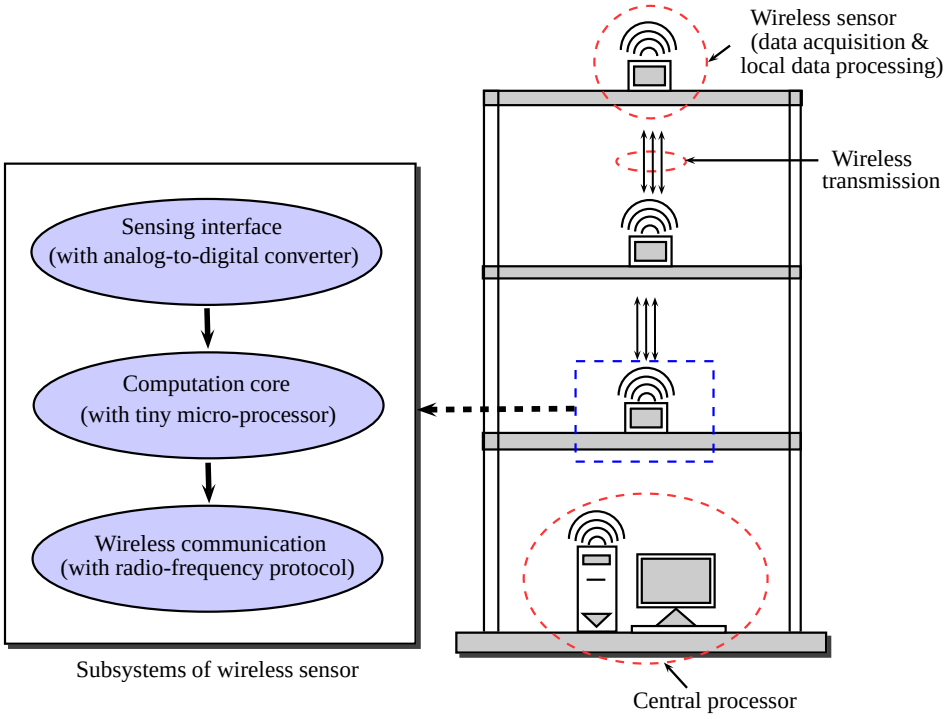

Figure 2.6: Key elements of WSSNs

Decentralized Sensor Networks

If one were to simply replace all the wired sensors with wireless units, then the data collection procedure changes; however, it has little or no effect on the processing algorithms and their use. While the use of wireless sensors in this setting is still attractive, it will be particularly advantageous if one were to use either just a fraction of the number of sensors and concatenate the information gathered from each set up, or to undertake local processing at the sensor level. The latter is made possible in WSSNs, as they are equipped with an onboard computing facility to enable local data processing within the network. The on-broad processor allows smart sensors to make decisions, perform computations, and save data locally. By conducting a portion of the computation at the sensor level, the volume of communication within the network is reduced, while retaining useful information. Either the use of limited sensors in multiple setups, or local processing, involves a decentralized

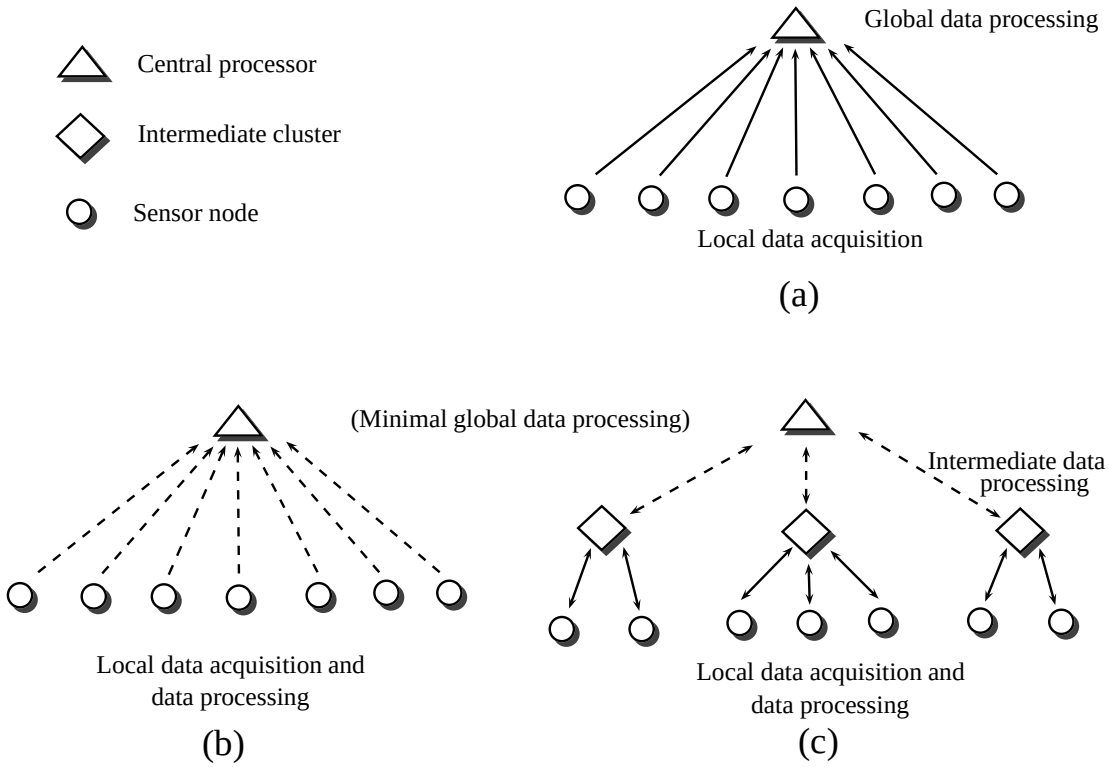

Figure 2.7: Various sensing system [121]: (a) centralized sensing system, (b) independent data processing, (c) coordinated computing strategy

architecture and most of the existing algorithms either need to be substantially modified, or need to be replaced with a *decentralized* system.

Various strategies [130, 136, 81, 22, 77, 151, 39, 93, 160, 122, 159, 156, 121, 36, 76, 58] of decentralized sensing systems have been implemented within the framework of SHM. One of them, popularly named as independent data processing (as in Fig. 2.7(b) [136, 22, 82, 99]), utilizes the local sensor nodes to process data, thus reducing the amount of data transferred throughout the network. However the spatial information is lost, thereby the mode shape cannot be extracted. Another decentralized approach is based on a coordinated computing strategy [39] to capture the local information. In this scheme (as in Fig. 2.7(c)), the network is divided into hierarchial communities in which the nodes within each community communicate with each other. Communication between each community is conducted

through a manager node. Similar types of coordinated computing strategies [93] have been implemented using the Imote2 sensor platform for damage detection. From Fig. 2.7(b) and (c), it is quite clear that local communication between fewer sets of wireless sensors imposes another challenge in identification within the context of BI, namely the underdetermined problem.

Recent wireless sensors have onboard processors that allow us to automate some of the SHM procedures [80]. This type of data interrogation presents several benefits. For example, reduced costs of these sensors allow for large-scale deployment. While, centralized processing in such cases would mean managing enormous amounts of data, on-board processing of measurement data can be an effective means to manage and minimize this effort. Furthermore, local data processing can be more energy efficient than transmitting raw time-history data wirelessly, which needs relatively large power. For example, according to [81] the amount of power consumed by the wireless sensor to perform on-board FFT and communicating just the peak frequencies is only 2% of the energy needed to transmit the original time series.

Recently, significant effort has been geared towards the development of on-board processing of WSSNs. The Cooley-Tukey implementation of the FFT has been successfully embedded and validated in the computational core of a wireless sensing unit [81] in instrumented structures. Lynch et al. (2004) [82] proposed embedding the complete AR-ARX time series method of damage detection in a wireless sensing unit for autonomous execution. The methodology allows sensor nodes to be computationally independent so that they can collect raw time-history records and generate results without node-to-node interaction or the exchange of time-history data. Recently, another decentralized method of detecting damage using a network of motes installed in a structural system has been proposed [22]. Once the modal frequencies and modal signal energy contributions are calculated using FFT at each sensor location, they are wirelessly transferred to a centralized data repository. Using on-board data compression by discrete wavelet transform, time histories are

then transmitted [82] through the wireless channels.

While most of the decentralized schemes [82, 39, 102, 160, 122, 159, 156, 121, 36, 76, 58] were developed for SHM, comparatively little effort is devoted for modal identification [160, 159, 122, 121]. The sequential decentralized sensing system in conjunction with a suite of conventional system identification methods (i.e., peak picking (PP) method, random decrement technique (RDT) and frequency domain decomposition (FDD) method) [160] is perhaps the first attempt in this regard. However this approach requires a linear network topology and may result in substantial accumulation of error in the global mode shapes. The decentralized technique in conjunction with FDD demands significant amount of memory as compared to PP method, which is a major constraint in WSSNs. Moreover, the accuracy of the results are sensitive to the choice of the topology. Recently stochastic optimization method is proposed in the parallel processing of data on WSSNs to efficiently utilize the distributed resources [159] of WSSNs. An automated hierarchial decentralized approach in conjunction with eigensystem realization algorithm [122] and stochastic subspace identification [121] was leveraged to reliably estimate modal parameters. However, these approaches involve several least-squares iterations, which is computationally expensive. These computations increase with increasing number of target modes and with increasing number of overlapping sensor groups. to address the issue of decentralized identification based on the principles of Blind Source Separation (BSS) [7, 115, 118] is presented and implemented in a pedestrian bridge at Montreal.

2.4.3 Challenges in decentralized modal identification

The following set of challenges are unique to decentralized modal identification.

1. **Availability of partial measurements:** In the framework of distributed sensing, various local sensor nodes communicate with each other or respond to an intermediate

cluster node, which finally communicate with the central node. Therefore, intermediate cluster nodes execute the communications between few or partial local sensors before transferring the data to a central node. From a modal identification point of view, the interaction between partial sensors to estimate the structural modes introduces a challenging mathematical problem, known as the *underdetermined* problem. Unlike full-rank problem, non-sparse BSS approaches or traditional methods (e.g., least-squares) are incapable of dealing with the under-determined problem. Hence, new methods need to be developed to handle this issue.

2. **Presence of narrowband excitation:** Most BSS methods in the context of modal identification assume that the excitation is white and does not contain narrow band excitation frequencies. However, this assumption is not satisfied in many situations when the excitation is a superposition of narrow-band harmonic(s) and broad-band disturbance, e.g., rotating machinery fixed to flexible structures, human induced vibration in pedestrian bridges, or dynamic interaction with surrounding structures. Under such conditions, traditional BSS methods (such as SOBI) yield sources (modes) without any indication as to whether the identified source(s) is a system or an excitation harmonic.

3. **Computational issues:** Tiny motes pose serious limitations to on-board processing. Most of the motes carry low power processors with limited storage and computation capabilities. New methods need to be computationally efficient such that low-cost wireless sensors can be utilized.

4. **Autonomous implementation:** User-intervention in decentralized implementation can be cumbersome and sometimes not possible. Hence, algorithms need to be simple and to a large extent, autonomous.

2.5 Summary

This chapter presented a survey of various traditional and modern system identification methods, followed by a brief introduction to WSSNs. The BSS based methods perform significantly better or similar to several existing time and frequency methods; this has been verified independently in the published literature. While the advantages of BSS methods is clear when applied to traditional batch processing algorithms, their advantage when applied within the context of WSSNs remains to be seen. Furthermore, WSSNs pose a unique set of challenges both physically as well as mathematically. These issues remain to be solved within the context of BSS methods.

Chapter 3

Sparse Blind Source Separation

In this chapter, a new decentralized algorithm is presented, geared towards modal identification using multiple sensor setups. The algorithm is based on the concept of sparsity, where measurement signals are transformed from time to the time-frequency domain. It is assumed that the model is one of static instantaneous mixing. In the transformed domain, the signals are expressed using a sparse basis, where the sources are referred to as the bases. The chapter is organized as follows. An introduction to the proposed method is presented first wherein the general problem is cast in a BSS framework. The formulation of the proposed algorithm is presented next, followed by a numerical study using a 5-DOF building example.

3.1 Introduction

Previous research in our group has resulted in several powerful algorithms based on BSS [45, 46, 48, 47, 112]. These methods are primarily geared towards the case of full-rank or over-determined modal identification. Extending these methods to the case of decentralized WSSNs is not straight-forward. Specifically, the case of decentralized implementation

results in a non-square mixing matrix as the number of available measurements is significantly lower than the number of identifiable modes. In this chapter, all these issues are addressed using the concept of sparsity, employing time-frequency transformations, followed by statistical signal processing operations.

3.1.1 Background on Sparsity

Sparsity can be explained by considering the two-dimensional case of Eq. 2.2, which in an expanded form is as follows:

$$\begin{bmatrix} x_1(k) \\ x_2(k) \end{bmatrix} = \begin{bmatrix} a_{11} & a_{12} \\ a_{21} & a_{22} \end{bmatrix} \begin{Bmatrix} s_1(k) \\ s_2(k) \end{Bmatrix} \tag{3.1}$$

In this example, if we assume that only one of the sources s_1 is present, then Eq. 3.1 can be expressed as:

$$\begin{bmatrix} x_1(k) \\ x_2(k) \end{bmatrix} = s_1(k) \begin{bmatrix} a_{11} \\ a_{21} \end{bmatrix} \tag{3.2}$$

¡in such a situation, a plot of x_1 versus x_2 results in the direction vector of partial mixing matrix coefficients. However, achieving sparsity directly in the time domain is difficult. In the simplest case, transformation into the frequency domain results in a sparse representation. For example, the time-domain and frequency domain transformations for a linear mixture of two harmonic signals with additive Gaussian noise are shown in Fig. 3.1. The line of orientation corresponding to the two harmonic sources are clearly realized in the frequency domain scatter plot. The aim of sparse approach is to perform transformations from the original signal space to a transformed space such that the sources are sparse, with at most one source active at any time. Although, in this example, a straight-forward Fourier transformation enabled the separation of partial mixing coefficients, the presence of noise and low-energy sources makes delineation difficult.

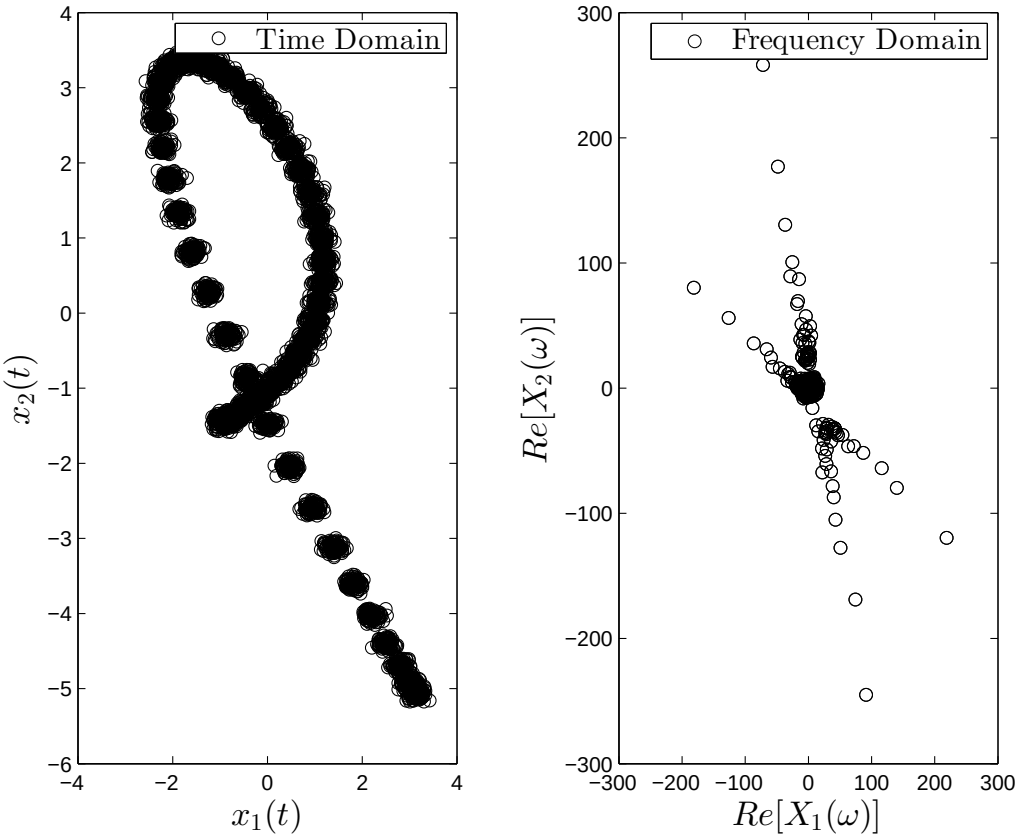

Figure 3.1: Sparsity under transformation

In the context of structural dynamics, the mixing coefficients and sources correspond to the modal matrix and modal responses, respectively. Let us consider a linear, lumped-mass and classically damped n_s DOF structural system, subjected to an excitation force, $\mathbf{F}(t)$.

$$\mathbf{M}\ddot{\mathbf{x}}(t) + \mathbf{C}\dot{\mathbf{x}}(t) + \mathbf{K}\mathbf{x}(t) = \mathbf{F}(t) \tag{3.3}$$

where, $\mathbf{x}(t)$ is a vector of displacement coordinates at the DOF. The solution to Eq. 3.3 can be written in terms of an expansion of vibration modes. In matrix form,

$$\mathbf{x} = \mathbf{\Phi}\mathbf{q} = \sum_{l=1}^{n_s} \phi_l q_l(t) \tag{3.4}$$

where, $\mathbf{x} \in \Re^{n_m \times N}$ is the trajectory matrix composed of the sampled components of $\mathbf{x}$, $\mathbf{q} \in \Re^{n_s \times N}$ is a matrix of the corresponding modal coordinates, and $\mathbf{\Phi}_{n_m \times n_s}$ is the modal transformation matrix or the mode shape matrix. Note the similarity between Eq. 3.4 and Eq. 2.2. Under the conditions where the modal coordinates are mutually uncorrelated with non-similar spectra, the normal coordinates can be regarded as the most uncorrelated sources [7]. Thus, the modal coordinates $\mathbf{q}$ are a special case of general sources $\mathbf{s}$ with time structure, and the mixing matrix is the mode-shape matrix. Therefore, exploiting sparsity to extract the modal information essentially comprises of transformations that render only one mode to be active at any time. This is undertaken using wavelet packet transforms (WPT), as discussed next. In the present study, the stationary WPT (SWPT) of the noisy mixtures at different scale levels are used to sparsify the signal.

3.1.2 Wavelet Transform

Wavelet Transform (WT) provides a useful way of representing signals through the use of basis functions that satisfy certain properties of linear vector spaces in $\Re^3$. It has found significant use in structural applications [40, 69, 64, 49, 128]. The use of sinusoidal basis

in the Fourier transform (FT) does not allow a meaningful representation of the non-stationary response of system response, thus limiting its application to ambient system identification. As the Fourier basis functions are localized only in frequency, an alternative to accommodate the time information was introduced via the short-time Fourier transform (STFT). However, due to the fixed nature of the windows used in STFT, resulting time and frequency resolutions are considerably limited. Analogous to Hiesenberg's uncertainty principle, it is impossible to achieve good time and frequency resolutions, simultaneously. This motivated the development of an alternative transform, namely WT, which provides better time-frequency representation of the signals in a multi-resolution framework.

The wavelet basis, due to its smoothness, compactness, rapid decaying characteristics and vanishing higher order moments, provides a sparse representation of vibration measurements. Under such transformations, the useful information content of the signal is retained, while the unnecessary contributions from noise are discarded. This provides better time-frequency representation of the signals, and makes them more localized, compact, smooth and noise free [142]. The WT of a signal $y(t)$ is a linear transform defined as [85]:

$$w_k^j(y) = \frac{1}{\sqrt{j}} \int_{-\infty}^{\infty} y(t)\, \psi_k^{j*}(t)\, dt \tag{3.5}$$

where the function ψ is commonly known as the mother wavelet and $*$ stands for complex conjugation. j and k denote scale and translation parameters, respectively. Therefore, WT decomposes a signal $y(t)$ using basis functions that are primarily scaled and translated versions of the mother wavelet. WT can be performed as redundant and non-redundant versions. Discrete wavelet transform belongs to the former category, while continuous wavelet transform and stationary wavelet transform belong to the latter. A brief background of various WTs is presented next.

Continuous Wavelet Transform

Continuous wavelet transform (CWT) of a signal *y(t)* is mathematically defined as:

$$c_k^j(y) = \int_{-\infty}^{\infty} y(t)\psi^* \left(\frac{t-k}{j}\right) dt \tag{3.6}$$

The inverse continuous wavelet transform (ICWT) is defined as :

$$y(t) = \frac{1}{C_\psi} \int_{-\infty}^{\infty} \int_{-\infty}^{\infty} \frac{1}{\sqrt{|j|}} c_k^j(x)\psi^* \left(\frac{t-k}{j}\right) \frac{dk\,dj}{j^2} \tag{3.7}$$

Where C_ψ is defined as :

$$C_\psi = \int_{-\infty}^{\infty} \frac{|\psi(\omega)|^2}{|\omega|} d\omega < \infty \tag{3.8}$$

Eq. 3.8 —known as the admissibility condition —restricts the class of functions that can represent wavelets. In addition, the CWT satisfies following regularity conditions [85].

$$\begin{aligned} \int_{-\infty}^{\infty} \psi(t)dt = 0 \\ \int_{-\infty}^{\infty} |\psi(t)|^2 dt < \infty \end{aligned} \tag{3.9}$$

The CWT as described so far has two features that makes it difficult to use directly in the form of Eq. 3.6. The first is redundancy. The CWT is calculated by shifting a continuously scalable function, not necessarily orthogonal, over a signal and calculating the correlation between them. The wavelet coefficients thus obtained are highly redundant. Another problem is that the CWT has no analytical solution for most of the functions, and only numerical ones can be obtained. Hence, fast algorithms are needed to exploit the full capabilities of WT.

Discrete Wavelet Transform

Discrete wavelet transform (DWT) is an orthogonal WT which takes care of the redundancy aspect of the CWT, thereby facilitating easy computation of WTs, and is defined as:

$$d_k^j(y) = \langle y(t), \frac{1}{2^{j/2}}\psi(\frac{t}{2^j} - k)\rangle = \frac{1}{2^{j/2}} \int_{-\infty}^{\infty} y(t)\psi^*(\frac{t}{2^j} - k)\ dt = \frac{1}{2^{j/2}} \int_{-\infty}^{\infty} y(t)\psi_k^{j*}(t)\ dt \quad (3.10)$$

The transform is computed at discrete values on a grid corresponding to dyadic values

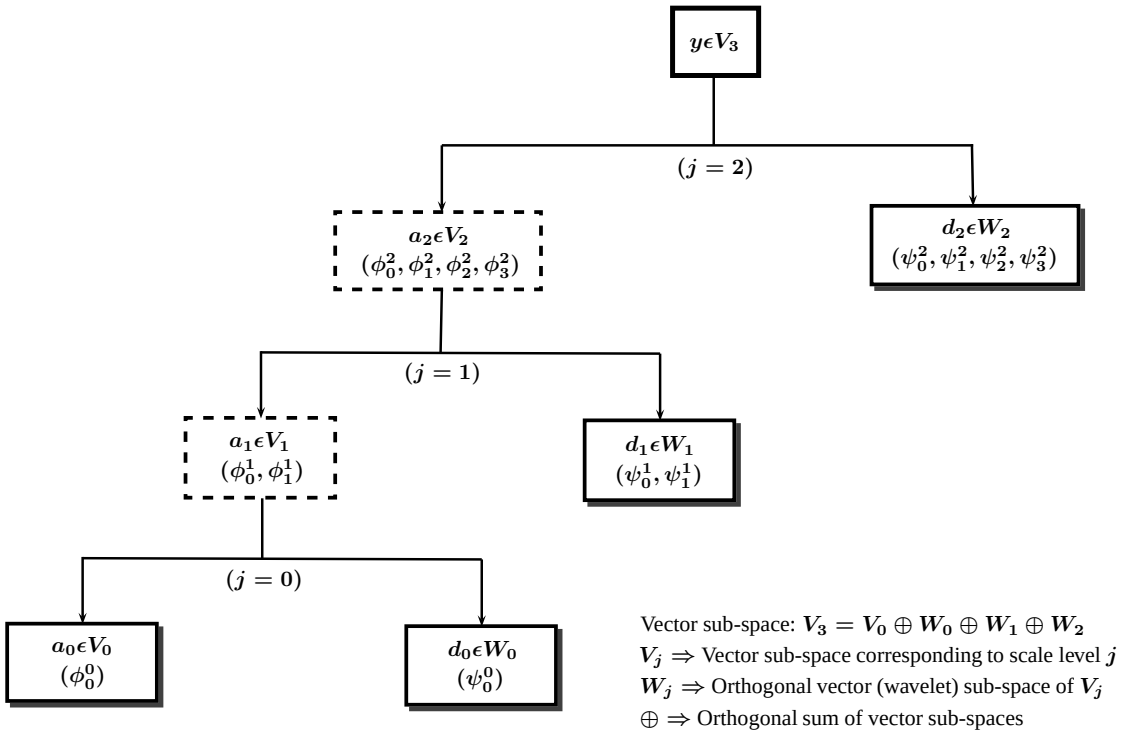

Figure 3.2: Multi-resolution analysis

of scales (2^j) and translations (k), where $k,\ j \in Z^2$ i.e., integers. A signal *y(t)* can be expressed in terms of wavelet coefficients d_k^j as:

$$y(t) = \sum_j \sum_k d_k^j \psi_k^j \quad (3.11)$$

The basis function ψ and its integer translates $\psi(t-k)$ satisfy the condition of orthogonality using the framework of multi-resolution as shown in Fig. 3.2. For fast implementation, the integration procedures are replaced by successive application of filter banks [85]. Implementation of DWT to any signal involves simultaneous low-pass (LP) and high-pass (HP) filtering operations using appropriate filters, known as quadrature mirror filters (QMF).

The coefficients resulting from these filtering operations are known as *approximation* and *detail* coefficients. However, since half of the frequencies of the signal have now been removed, half of the samples can be discarded according to the Nyquist criterion. The filter outputs are then down-sampled by a factor 2 [85]. For example, as shown in the Fig. 3.3(a), the DWT of signal $x(n)$ containing N data points, is performed up to scale level, $j = 2$. Data length of the approximate (a_d^j) and detail coefficients (d_d^j) at scale level j, are reduced by a factor 2^j. The data length of the decomposition coefficients becomes $N/2$ and $N/4$ at the decomposition level 1 and 2, respectively. L_d^j and H_d^j represent the LP and HP filters at the j^{th} scale level of DWT. Details of the DWT implementation are beyond the scope of this work and the readers are referred to seminal works [85] on the topic for details.

Although non redundant, the fundamental drawback of the discrete wavelet transform is *non-invariance* in time. To see this, let the shifted version of the signal *y(t)* signal $y(t-t_m)$ be considered. For shift k the time invariance would imply : $d_k^j\{y(t-t_m)\} = d_{k+t_m}^j\{y(t)\}$. Substituting $d_k^j\{y(t-t_m)\}$ in the Eq. 3.10 and replacing the integral by summation, the following expressions are obtained :

$$\begin{aligned} d_k^j\left\{y(t-t_m)\right\} &\approx 2^{-j/2}\sum_n y(n-m)\,\psi(2^{-j}n-k) \\ &= 2^{-j/2}\sum_n y(n)\,\psi(2^{-j}n-\{k-m2^{-j}\}) \\ &\approx d_{k-m2^{-j}}^j\{y(t)\} \end{aligned} \tag{3.12}$$

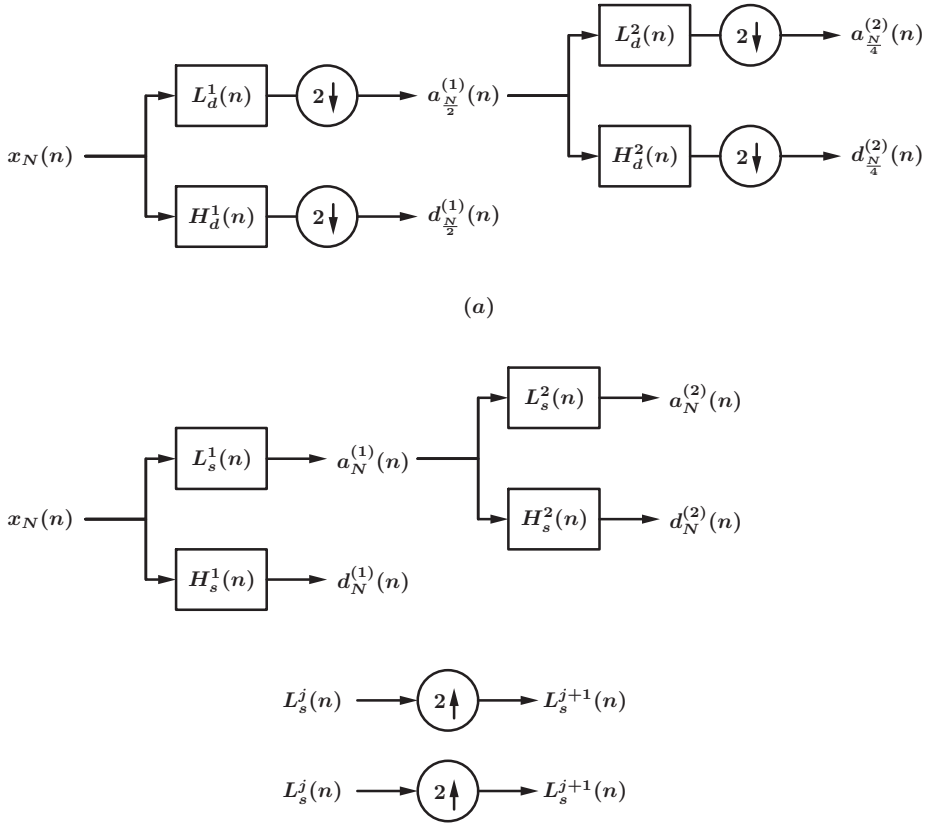

Figure 3.3: Filter bank implementation (a) DWT, (b) SWT

Where, m signifies the discrete value corresponding to the time point t_m. This means that the wavelet coefficients of a time shifted signal, say $y(t-\tau)$, are not delayed versions of the transform of the original signal. That is:

$$d_k^j(y(t-\tau)) \neq d_{k-\tau}^j(y(t)) \tag{3.13}$$

Eq. 3.13 clearly shows the time non-invariance of DWT. The invariance issue shown above can be addressed through a redundant version of the DWT, as explained in the following.

Stationary Wavelet Transform

Consider the following transform, known as the stationary wavelet transform (SWT), of $y(t)$ [95, 35].

$$w_k^j(y) \triangleq \left\langle y(t) \;\middle|\; 2^{-j/2}\psi\left(\frac{t-k}{2^j}\right)\right\rangle = \frac{1}{2^{j/2}}\int_{-\infty}^{\infty} y(t)\psi^*\left(\frac{t-k}{2^j}\right)dt \tag{3.14}$$

The basic idea of the SWT is similar to the DWT. The time sequence whose transform is to be carried out is applied through appropriate high and low pass filters to produce two sequences at the next level. But unlike the DWT, the filtered sequences are not decimated, rather filter coefficients of the j^{th} scale level are up-sampled to form their counterparts at $(j+1)$ level. Hence the filtered sequences have the same length as the original sequence irrespective of the scale level. The implementation of the SWT is illustrated in Fig. 3.3(b).

The most important property of the SWT is time-invariance. Considering again, the shifted version of the signal *y(t)* signal $y(t-t_m)$ and substituting $w_k^j\{y(t-t_m)\}$ in Eq. 3.14, the following expressions are obtained:

$$\begin{aligned} w_k^j\left\{y(t-t_m)\right\} &\approx 2^{-j/2}\sum_n y(n-m)\,\psi(2^{-j}n - 2^{-j}k) \\ &= 2^{-j/2}\sum_n y(n)\,\psi\left(\frac{n-\{k-m\}}{2^j}\right) \\ &\approx w_{k-m}^j\left\{y(t)\right\} \end{aligned} \tag{3.15}$$

which means that the coefficients of a delayed signal are a time shifted version of those of the original signal. Unlike DWT, SWT retains its time structure and therefore does not affect the sample size. This is an important property that is utilized in the proposed method. This is illustrated using the following examples.

Change in sample length – DWT vs. SWT

• ***Numerical illustration – mixture of sine waves***

A mixture of two sine waves is considered with $\omega = 1.0$ Hz and $\omega_2 = 3.5$ Hz. A white Gaussian noise (WGN) with SNR = 10 is added and the noisy mixture is shown in Fig. 3.4. The sampling frequency is 200 Hz and the total data length is 2048.

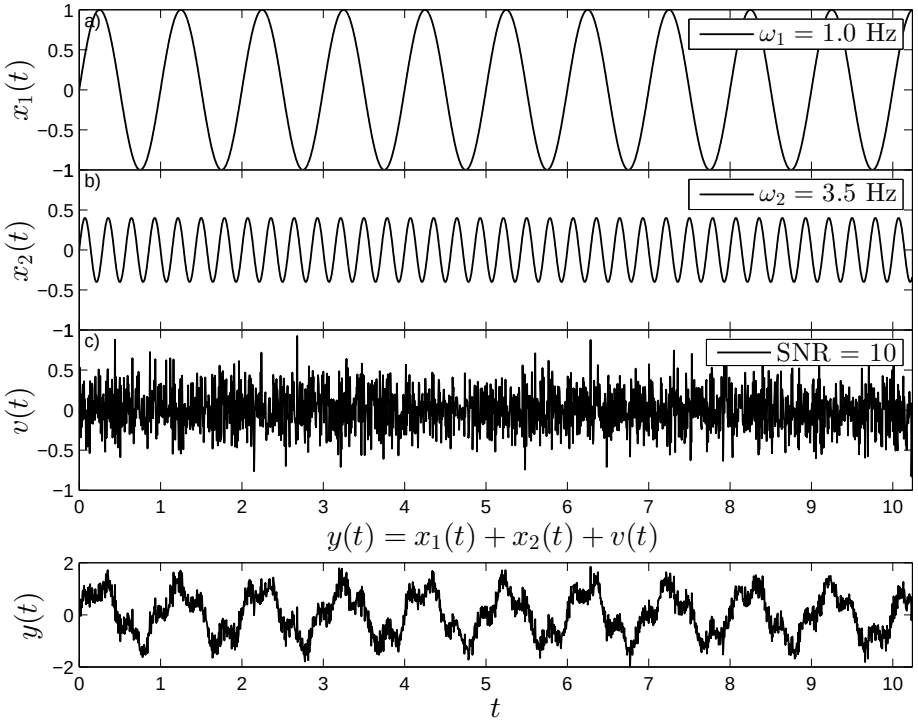

Figure 3.4: Mixture of sine waves and noise

DWT and SWT are performed up-to a scale level of 6. *db*5 is chosen as the wavelet basis. The approximate coefficients at each scale level (a_j) are shown in Fig. 3.5. It is noted that the sample length of a_j decreases by a factor 2^j in case of DWT, whereas it remains unchanged in SWT. In order to see the effect of change in the data length, the approximate coefficients at the last scale level, a_0 as obtained using DWT and SWT are compared. a_0 contains the sine wave with $\omega_1 = 1.0$ Hz. As shown in Fig. 3.6, there is

significant deterioration in the time structure of a_0 in the case of DWT, however SWT retains the original time structure of the sine wave.

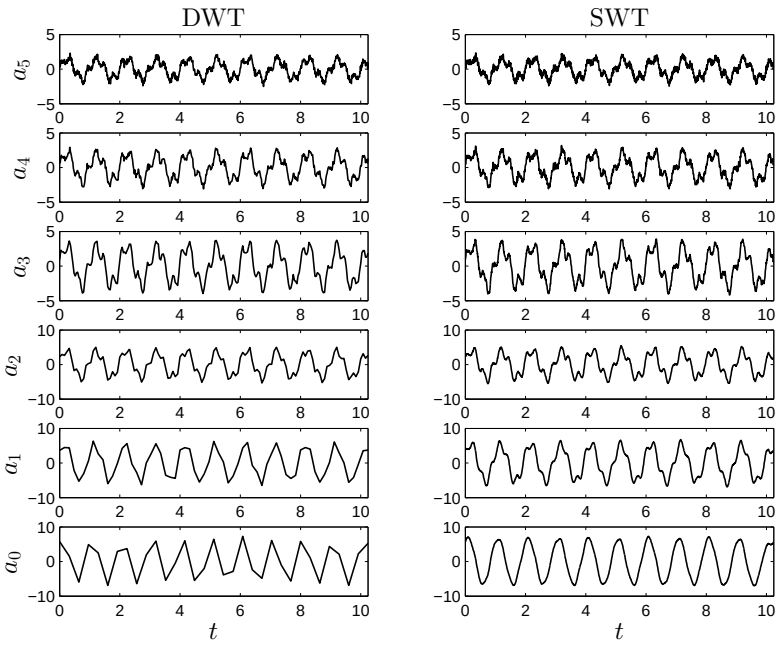

Figure 3.5: DWT and SWT coefficients of the noisy mixture

• ***Numerical illustration – response of a building model***

The roof acceleration of an example building is considered. A WGN with SNR = 10 is added and a similar analysis is performed using DWT and SWT, as described in the previous section. The DWT and SWT are performed up-to a scale level 6 as in Fig. 3.7. *db*5 is chosen as the wavelet basis. In order to see the effect of change in the data length, the approximate coefficients at the last scale level, a_0, are compared between DWT and SWT. a_0 contains the source corresponding to $\omega_1 = 0.91$ Hz. As shown in Fig. 3.8, there is a significant deterioration in the time structure of a_0 in the case of DWT, however SWT retains the original time structure of the source.

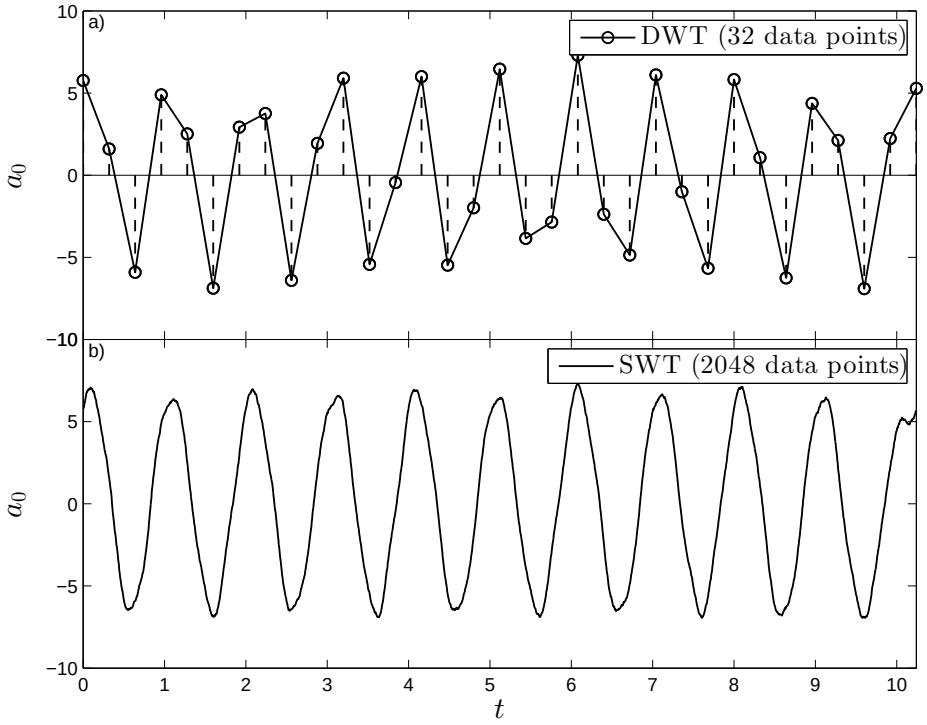

Figure 3.6: Comparison of last scale level coefficient of DWT and SWT of the noisy mixture

3.1.3 Wavelet Packet Transform

In the filter-bank implementation of WT, the low frequency coefficients of j^{th} level are decomposed into low and high frequency coefficients at the next level, while the high frequency coefficients of the j^{th} level remain un-filtered. Thus, the resolution of WT is rather poor in the high-frequency content of the signal, as it does not offer sufficient sub-bands. Hence, WT is not suitable for discriminating signals containing poorly excited non-sparse high and/or intermediate frequencies commonly occurring in structural applications [131]. The wavelet packet transform (WPT) [30, 142, 107] is an extension of WT that offers a complete level-by-level decomposition, where both the details as well as the approximations are filtered. As a result, the information in both the low and high frequency sub-bands are captured. Both the redundant version of DWT, stationary wavelet transform (SWT) and the DWT can be implemented in the form of packet transforms.

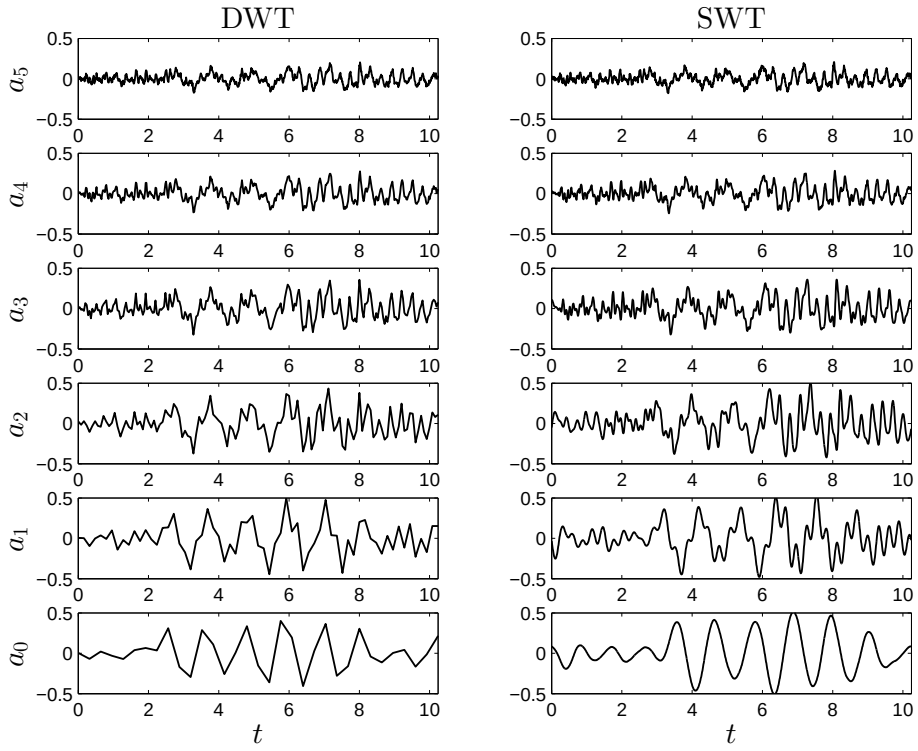

Figure 3.7: The DWT and SWT coefficients of the roof acceleration

Although non-redundant, DWT creates artifacts around the discontinuities of the input signal [29] and is shift-variant. Moreover, the length of the signal reduces with increasing scale levels. Therefore the time resolution reduces significantly at higher scale levels. This could pose a serious issue while dealing with non-stationary ambient vibration data, as well as in estimating the damping of the time series of the modal responses. Unlike DWT, SWT has the important shift-invariance property and the original time structure which is particularly useful for modal analysis, specially for estimation of modal damping. If SWT is implemented in the form of packets, all the sub-bands are shift-invariant and each sub-band provides a shiftable description of signal at a specific scale, which is similar to SWT [95]. In doing so, this improves not only the frequency resolution, but also maintains the temporal resolution. Thus the stationary WPT (SWPT) is adopted as the time-frequency tool for the present study. The details of the SWPT are explained next.

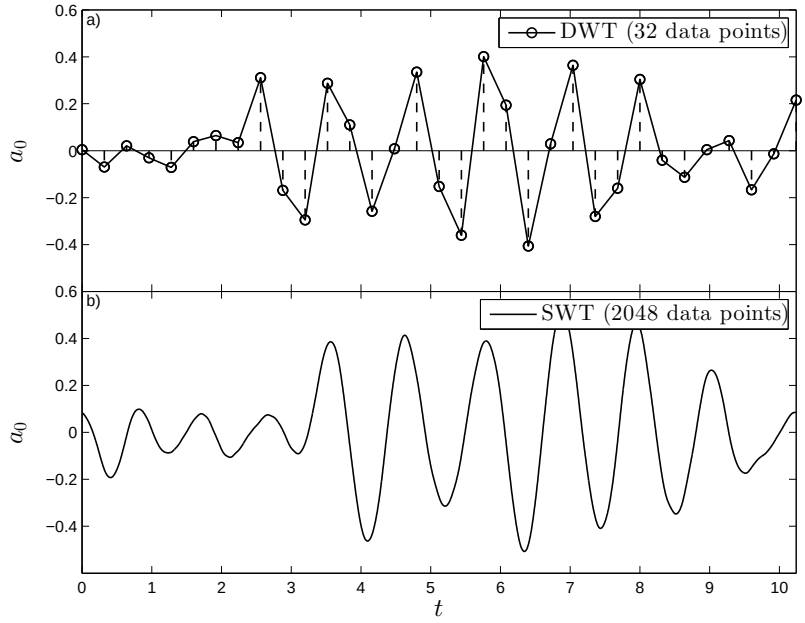

Figure 3.8: Comparison of the last scale level coefficient of DWT and SWT of the roof acceleration

WPT is an extension of the wavelet transform and can be carried out by a generalization of the pyramidal algorithm [30, 107]. A wavelet packet is a triple-index function $\psi_k^{j,v}(t)$, where j, k and v can be interpreted as scale, shift and frequency parameter [142, 85, 126] and a SWPT basis is represented as [107]:

$$\psi_k^{j,v}(t) = \frac{1}{2^j}\psi^v\left(\frac{t-k}{2^j}\right) \tag{3.16}$$

where $\psi^{1,0}(t) = \phi(t)$ and $\psi^{1,1}(t) = \psi(t)$ represent the scaling (father) and wavelet (mother) function respectively. At a given scale level j, a binary tree as shown in Fig. 3.9 can be formed using the basis functions, $\psi_k^{j,v}(t)$, whose nodes are indicated by the scale level, j and the frequency parameter, $v = 0, 1, 2, ..., (2^j - 1)$. The wavelet packet coefficients at each node (j, v) are written as:

$$w_k^{j,v}(y) \triangleq \left\langle y(t) \;\middle|\; 2^{-j/2}\psi^v\left(\frac{t-k}{2^j}\right)\right\rangle = \frac{1}{2^{j/2}}\int_{-\infty}^{\infty} y(t)\psi^v\left(\frac{t-k}{2^j}\right)dt \tag{3.17}$$

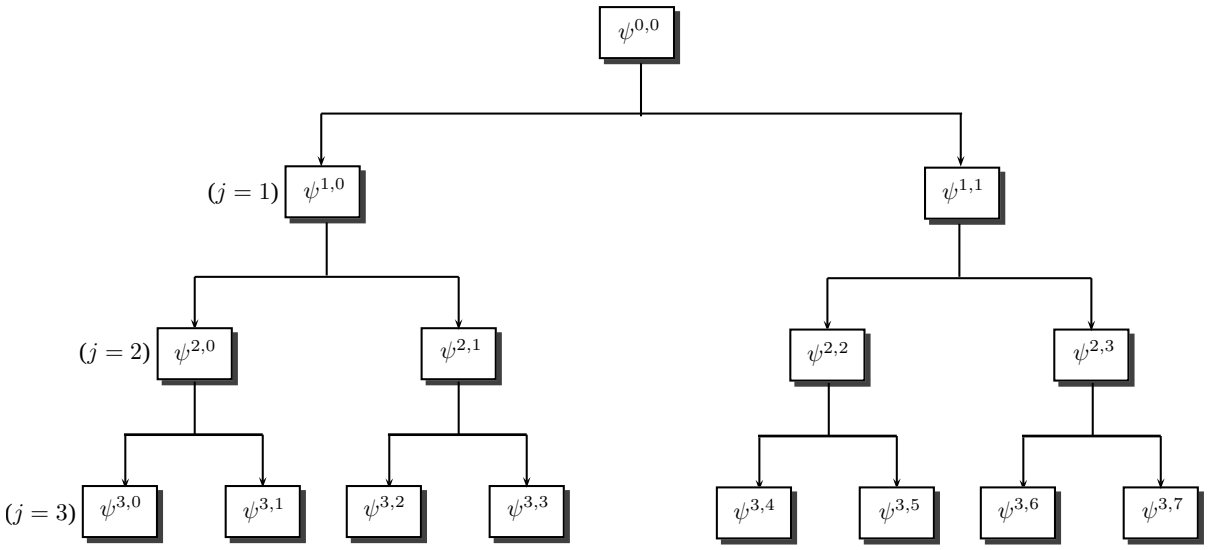

Figure 3.9: SWPT binary tree: Indexing of $\psi^{j,v}$ at different j and v

The wavelet packet component signal $y^{j,v}(t)$ at each node (j, v) (the component associated with each node of the binary tree shown in Fig. 3.9) can be expressed as a linear combination of wavelet packet basis functions $\psi_k^{j,v}(t)$:

$$y^{j,v}(t) = \sum_k w_k^{j,v} \psi_k^{j,v}(t) \tag{3.18}$$

At a j^{th} level of decomposition, the original signal $y(t)$ can be represented as the summation of all wavelet packet component signals, $y^{j,v}$:

$$y(t) = \sum_{v=0}^{2^j-1} y^{j,v} = \sum_{v=0}^{2^j-1} \sum_k w_k^{j,v} \psi_k^{j,v}(t) \tag{3.19}$$

Thus, the WP is a generalization of wavelets in that each frequency band of the wavelet spectrum is further sub-divided into finer frequency bands by using the dyadic scale decomposition.

3.2 Details of the Proposed Algorithm

Having explained the underlying principles of time-frequency transformations using SWPTs, the details of the algorithm as applied to the case of decentralized identification is explained next. Please note that a decentralized implementation results in the underdetermined case, i.e., $n_m < n_s$ (i.e., $\mathbf{A}$ is non-square). Hence, $\mathbf{A}$ is non-invertible, and estimating $\mathbf{W}$ and $\mathbf{s}$ through conventional BSS tools is not possible. Hence, as explained previously, when the sources are sparse, the majority of the data will be aligned along the direction of basis vectors, and the directions of the maximum data density will then yield the partial mixing coefficients [115, 118].

Assuming the measurements can be represented in the form expressed in Eq. 3.4, The measured signal at the i^{th} sensor location can be expressed as:

$$x_i(t) = \sum_{l=1}^{n_s} A_{il} s_l(t) \qquad i = 1, 2, ..., n_m \tag{3.20}$$

where i and l are the sensor and source index respectively.

In case of partial measurements corresponding to q^{th} and r^{th} sensors ($n_m = 2$ and $n_m < n_s$; $\mathbf{x}_m = \{x_q, x_r\}^T$), we get:

$$\begin{aligned} x_q(t) &= \sum_{l=1}^{n_s} A_{ql} s_l(t) \\ x_r(t) &= \sum_{l=1}^{n_s} A_{rl} s_l(t) \end{aligned} \tag{3.21}$$

Considering the orthogonal wavelet decomposition of the sources using Eq. 3.18, we can express the individual source signal in terms of its decomposition coefficients:

$$s_l^{j,v}(t) = \sum_k e_{k,l}^{j,v} \psi_k^{j,v}(t) \qquad l = 1, 2, ..., n_s \tag{3.22}$$

where j, k, and v represent scale, shift, and frequency index respectively. $e_{k,l}^{j,v}$ denotes the wavelet packet coefficient of l^{th} source at a specific node (j, v). $\psi(t)$ is the chosen mother wavelet. Similarly, i^{th} component of the measurement $\mathbf{x}_m$ can be also expressed as:

$$x_i^{j,v}(t) = \sum_k f_{k,i}^{j,v} \psi_k^{j,v}(t) \qquad i = 1, 2, ..., n_m \tag{3.23}$$

where $f_{k,i}^{j,v}$ represents the wavelet packet coefficient of the i^{th} sensor at a specific node (j, v).

Considering the wavelet packet coefficients of the responses measurements and sources at any specific node (j, v), inserting Eq. 3.22 and 3.23 in Eq. 3.20, and finally applying the orthogonality condition for wavelets, we get:

$$f_{k,i}^{j,v}(t) = \sum_{l=1}^{n_s} A_{il} e_{k,l}^{j,v}(t) \tag{3.24}$$

From the definition of WPT, the coefficients at highest scale level ($j = s$, where s is the last, or highest scale level) are most likely to be mono-component and thereby sparse in nature [66]. The appropriate choice of s depends on the sampling rate and the lowest frequency content of the signal. Thus when s is properly chosen, and only the coefficients corresponding to the highest scale level are considered, various coefficients of the s^{th} scale level contain the sparse modal responses and high frequency noise components. Thus, assuming the existence of only l^{th} source component in the $f_{k,i}^{s,v}$, Eq. 3.24 becomes:

$$f_{k,i}^{s,v}(t) = A_{il} e_{k,l}^{s,v}(t) \qquad i = 1, 2, ..., n_m \tag{3.25}$$

Above expression relates the SWPT coefficient of i^{th} sensor response with the SWPT coefficient of l^{th} source (modal response). Therefore, following the same logic for $i = q$ and $i = r$ in Eq. 3.21, the partial mixing matrix coefficient of q^{th} floor normalized w.r.t the r^{th}

floor can be obtained as:

$$\frac{f_{k,q}^{s,v}}{f_{k,r}^{s,v}} = \frac{A_{ql}e_{k,l}^{s,v}(t)}{A_{rl}e_{k,l}^{s,v}(t)} = \frac{A_{ql}}{A_{rl}} = |\widehat{a_{ql}}|; \qquad l = 1, 2, ...n_s \tag{3.26}$$

Then $\widehat{a_{ql}} = \frac{A_{ql}}{A_{rl}}$ represents the estimated normalized mixing matrix coefficient of l^{th} mode at q^{th} DOF. In this way, the normalized partial mixing matrix coefficients are estimated using the SWPT coefficients of the partial sensor measurements at the highest scale level of WPT decomposition.

It is plausible that the wavelet packet coefficients originating from higher values of v indicate noise, and contain lower energy compared to the physical structure modes. In order to get rid of these coefficients, one might consider only those coefficients that have significant amount of energy, and thereby maximizing the sparsity of the response data. This can be implemented using any standard thresholding technique [29, 41]. In the current research, a thresholding based on average root-mean-square (RMS) value of the coefficients is utilized. The coefficients with RMS value less than the average RMS value (μ_{RMS}) of all coefficients are discarded and the remaining coefficients are retained for further analysis. This noise removal process makes the algorithm fast and efficient and at the same time does not ignore coefficients with significant energy contributions.

Filter banks established out of the wavelet packets have overlapped frequency contents due to imperfect digital filtering operation [37, 85]. This creates the possibility of having multi-component sources in the WPT coefficients at the last scale level. However, Eq. 3.25 and Eq. 3.26 are legitimate only when the coefficients comprises of mono-component signals. In order to detect the mono-component sources in the wavelet coefficients, principal component analysis (PCA) [59] is performed using these coefficients. This enables the determination of the direction of maximum variance of the coefficients. PCA is an orthogonal transformation that converts a $N \times p$ data matrix $\mathbf{X}$ to a matrix $\mathbf{M}$, by combining the

vectors of $\mathbf{X}$ according to the linear relationship:

$$\mathbf{M}^T = \mathbf{P}\mathbf{X}^T \tag{3.27}$$

where $\mathbf{P}$ is the transformation matrix, which represents the direction of maximum possible residual variance in the measured variables, while maintaining orthonormality with the transformed vectors.

However, imperfect filtering will result in mode mixing of wavelet coefficients (at the highest scale level). Assuming a mode mixing of n_m sources, Eq. 3.25 in the matrix vector form as:

$$\mathbf{f}_\alpha^{s,v} = \mathbf{A}\mathbf{e}_\alpha^{s,v} \tag{3.28}$$

Multiplying both sides by $\mathbf{f}_\alpha^T$ and taking the mathematical expectation on both the sides, we obtain:

$$E\{\mathbf{f}_\alpha^{s,v}\mathbf{f}_\alpha^{Ts,v}\} = \mathbf{A}E\left[\mathbf{e}_\alpha^{s,v}\mathbf{e}_\alpha^{Ts,v}\right]\mathbf{A}^T \tag{3.29}$$

Using Eq. 3.29, we have:

$$\mathbf{R}_\mathbf{f}(0) = \mathbf{A}\mathbf{R}_\mathbf{e}(0)\mathbf{A}^T \tag{3.30}$$

PCA is an orthogonal transformation in which $\mathbf{R}_\mathbf{f}(0) = (1/N)(\sum_{k=1}^{N} \mathbf{f}_\alpha^{s,v}(k)\mathbf{f}_\alpha^{Ts,v}(k))$ is diagonalized using singular value decomposition, $\mathbf{R}_\mathbf{f}(0) = \mathbf{V}_{\mathbf{f}_\alpha^{s,v}}\mathbf{\Lambda}_{\mathbf{f}_\alpha^{s,v}}\mathbf{V}_{\mathbf{f}_\alpha^{s,v}}^T$, where $\mathbf{V}_{\mathbf{f}_\alpha^{s,v}}$ are the eigenvectors of the co-variance matrix of $\mathbf{f}_\alpha^{s,v}$. Then, the classical linear transformation expressed as:

$$\mathbf{f}_\alpha^{s,v_p}(k) = \mathbf{V}_{\mathbf{f}_\alpha^{s,v}}^T\mathbf{f}_\alpha^{s,v} \tag{3.31}$$

PCA results into the major and minor principal components (PC), principal directions and their respective variances (σ_1^2 and σ_2^2). The ratio of major and minor variances is defined as the condition number (CN) [59]. In the present study, the reciprocal of the conditional number (RCN) as defined below is utilized as a parameter to identify the

mono-component coefficients.

$$\text{RCN} = \frac{\sigma_2^2}{\sigma_1^2} \tag{3.32}$$

A relatively small value of RCN (RCN$\ll$ 1) indicates mono-component coefficients. However, if the coefficients are multi-component, the minor PC will exhibit significant variance. Eq. 3.26 is strictly true for the mono-component coefficients containing lower value of RCN. Therefore, the principal direction of the WPT coefficients at last scale level with small RCN values yields the partial matrix. If the number of target modes is n_t, the coefficients with first n_t lowest RCN values are selected as sources. The advantage of using PCA lies in the fact that the corresponding major principal component readily yields the dominant modal response, from which the natural frequency and damping of the corresponding mode are estimated. This procedure is repeated for two sensor measurement locations at-a-time with a common reference sensor. The partial mixing coefficients obtained in each subset of measurements are concatenated to yield the complete modal mixing matrix.

The key steps involved in the proposed method are shown using a flowchart in Fig. 3.10 [115]. The steps in Fig. 3.10 are repeated for two sensors at-a-time and the partial modal information are then concatenated to yield the complete modal information.

Once the modal responses are identified, the modal frequencies and damping are estimated from the SWPT coefficients by treating them as single-degree-of-freedom systems. Due to the shift-invariance property of SWPT coefficients [95], the time structure of SWPT coefficients i.e., the modal responses, are unaffected. Modal frequencies are identified by using the Fourier transform of the modal responses as selected by the proposed method. For the damping estimation, autocorrelation functions of the modal responses are first estimated. Modal damping is then identified by fitting an exponential decay to the relative maxima of the auto-correlation function [69, 127]. Subsequently, the partial mode shape coefficients $\Phi_{2\times n_s}$ are estimated using Eq. 3.26 by utilizing the relevant SWPT coefficients

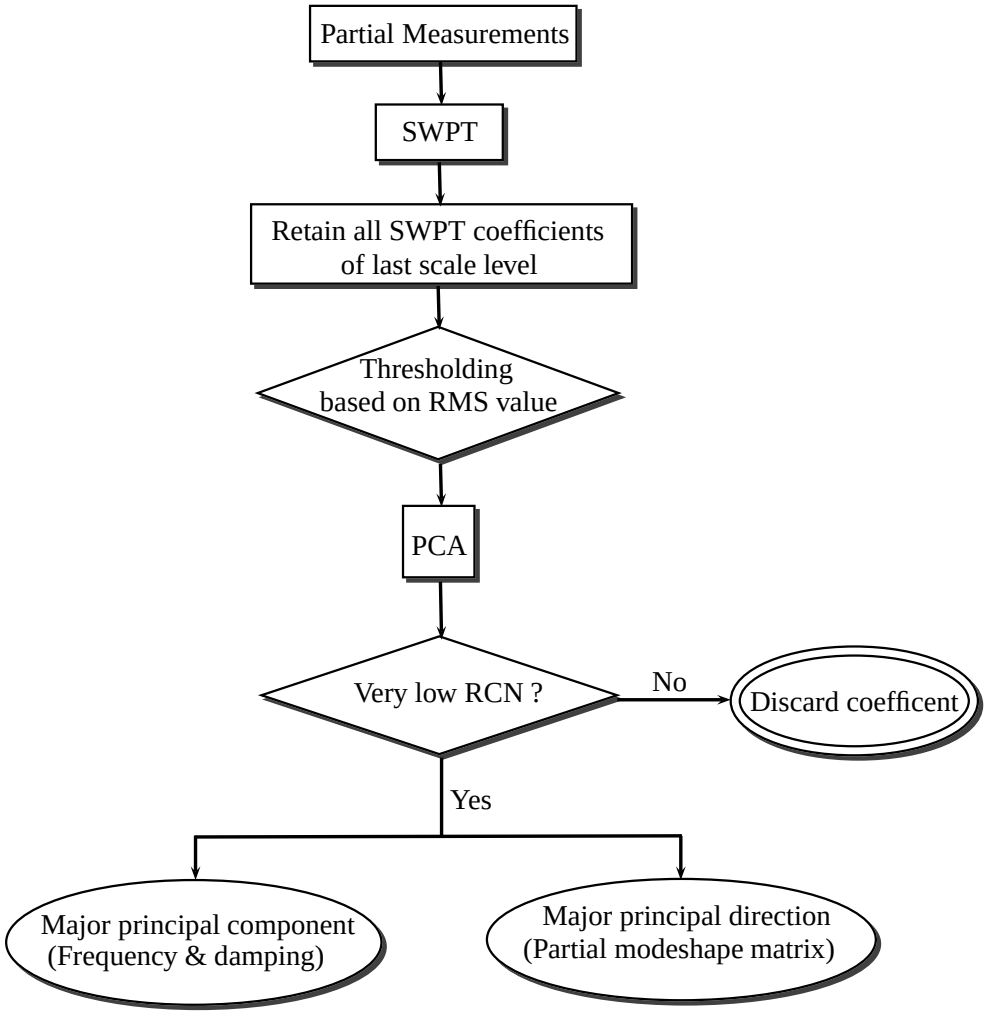

Figure 3.10: Flowchart of the proposed method

containing the modal responses.

3.2.1 Complete modal information synthesis from partial mode information

Calculating the partial mixing coefficients from two sensors (corresponding to the q^{th} and r^{th} measurement channels) has been explained so far. This process can be repeated using a fixed or movable common reference sensor location, which is the essence of the decentralized

sensing concept. Few example topologies [160, 122, 115] for the decentralized network using a 5-DOF building (used subsequently in the numerical example section) are depicted in Fig. 3.11.

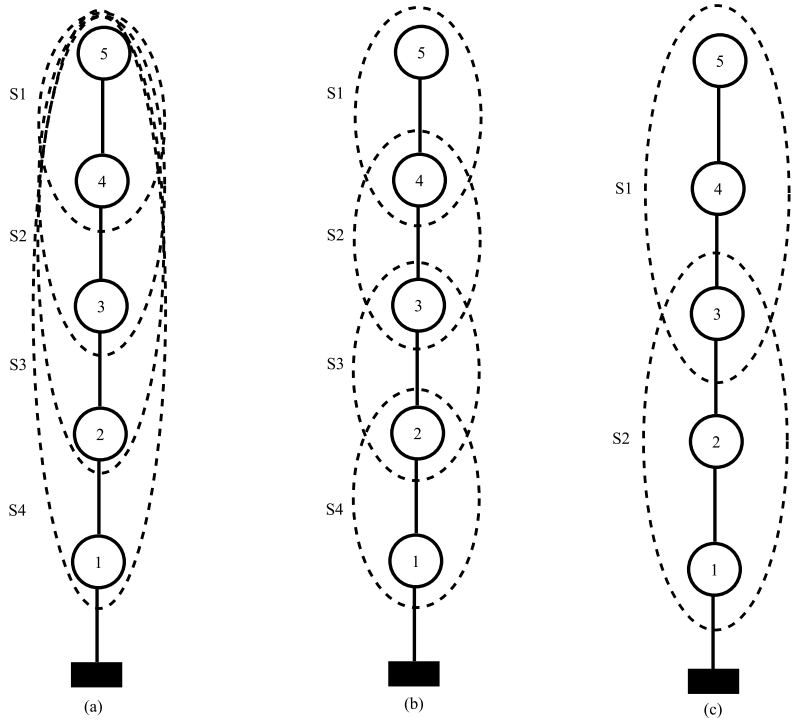

Figure 3.11: Various topologies for decentralized implementations: (a) topology-1 (fixed common reference), (b) topology-2 (movable common reference), (c) topology-3 (movable common reference)

In topology-1 (T_1), there are a total of four sensor groups, with a common reference sensor fixed at the 5^{th} floor. As shown in Fig. 3.11, each group denoted by Si contains two measurements processed at a time, $S1(5-4)$, $S2(5-3)$, $S3(5-2)$ and $S4(5-1)$. On the other hand, topology-2 (T_2) and topology-3 (T_3) do not have a common reference sensor between for all the groups, but only between two adjacent ones. If $\hat{\phi}_{i,j}^{Si}$ represents the estimated mode shape coefficient at the i^{th} DOF of j^{th} mode ϕ_j in the Si setup, then

$\hat{\phi}_j$ is simply the union of the partial mode shape coefficients, $\hat{\phi}_{i,j}^{Si}$ from each group (S_i):

$$\hat{\phi}_j = \bigcup_{Si=1}^{Sg} \hat{\phi}_{i,j}^{Si} \tag{3.33}$$

where, Sg is the total number of groups. Finally the complete mode shape matrix is obtained using $\Phi = [\hat{\phi}_1|\hat{\phi}_2|...|\hat{\phi}_j|...|\hat{\phi}_{n_s}]$. The accuracy of the estimated mode shape matrix is evaluated by comparing them with the theoretical modes using the Modal Assurance Criterion (MAC), defined by [84]:

$$\text{MAC}_i = \frac{(\psi_{t,i}^T \psi_{e,i})^2}{(\psi_{t,i}^T \psi_{e,i})(\psi_{t,i}^T \psi_{e,i})} \tag{3.34}$$

where $\psi_{t,i}$ and $\psi_{e,i}$ represent the theoretical and the estimated i^{th} mode shape vectors, respectively.

3.3 Numerical Study

In order to demonstrate the proposed method, simulations are performed on a 5-storey shear-beam structure model [115]. The state-space model for this system subjected to an external disturbance vector $\mathbf{w}$ is given by:

$$\begin{aligned} \dot{\mathbf{x}} &= \mathbf{A}\mathbf{x} + \mathbf{E}\,\mathbf{w} \\ \mathbf{y} &= \widetilde{\mathbf{C}}\mathbf{x} \end{aligned} \tag{3.35}$$

Here, the vector $\mathbf{x}$ is a vector of states, and the vector $\mathbf{y}$ represents the output vector, which is governed by $\widetilde{\mathbf{C}}$ matrix. The matrix $\mathbf{E}$ governs the location of the excitation on the structure. The system matrix $\mathbf{A}$ is constructed using $\mathbf{M}$, $\mathbf{C}$ and $\mathbf{K}$ matrices. For the example building, the lumped weight of each floor is assumed to be 19.2 kN, and the

damping is assumed to be 2% critical in all modes. The natural frequencies are obtained as 0.91, 3.37, 7.11, 10.66 and 12.73 Hz. The mode shape matrix (normalized with respect to top floor) for the building is given by:

$$\begin{bmatrix} 1.00 & 1.00 & 1.00 & 1.00 & 1.00 \\ 0.82 & -0.087 & -1.29 & -2.52 & -3.39 \\ 0.59 & -0.91 & -0.87 & 1.81 & 5.43 \\ 0.34 & -1.02 & 1.23 & 0.94 & -5.84 \\ 0.11 & -0.48 & 1.35 & -2.86 & 4.84 \end{bmatrix} \tag{3.36}$$

The 5-DOF building ($n_s = 5$) model is excited by the zero-mean unit variance Gaussian white noise at all floor levels. Only 5^{th} and 4^{th} floor responses ($n_m = 2$), $x_5(t)$ and $x_4(t)$ are

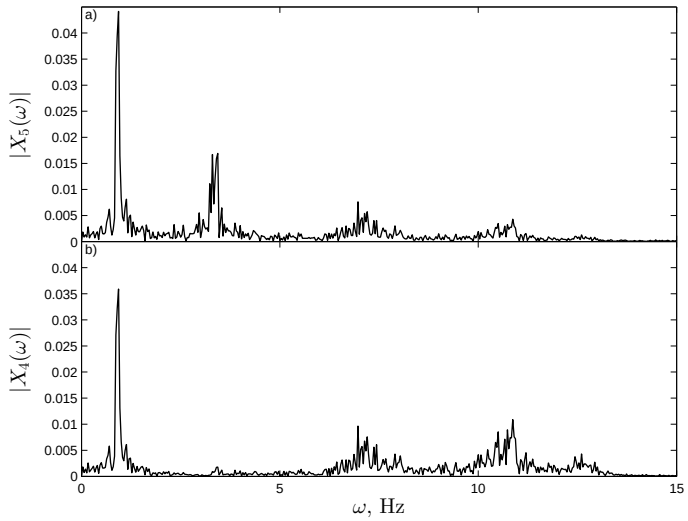

Figure 3.12: Fourier Spectra of the partial responses

used to estimate the partial mixing matrix ($\mathbf{A}_{2\times5}$). Fig. 3.12 shows the plots of the Fourier spectrum (FS) of the floor responses with added measurement noise having signal-to-noise ratio (SNR) of 100.

The SWPT is first performed on the two floor responses up to scale level $s = 6$. The

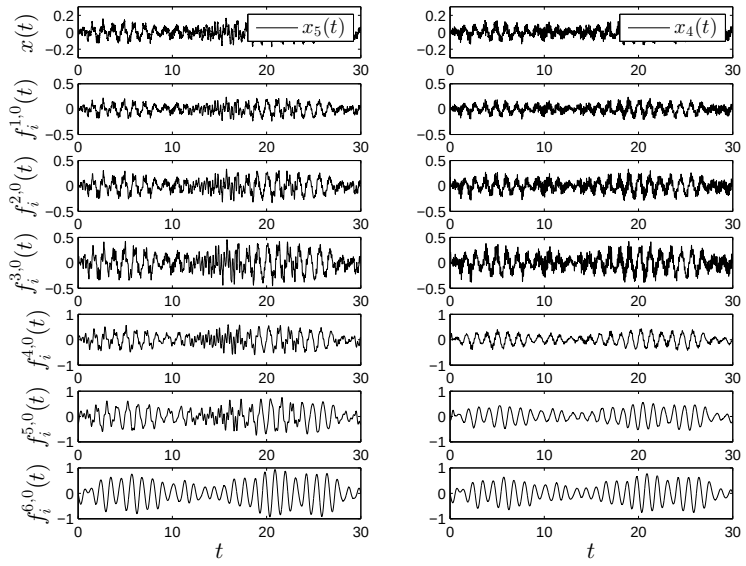

Figure 3.13: LP-wavelet packet coefficients of measurements at various scale levels

maximum scale level is selected based on the sampling frequency of the signal and the magnitude of the lowest frequency content of the measurement. $db5$ wavelet basis is chosen for the analysis. Fig. 3.13 shows the wavelet packet transform of the measurement signals at the 5^{th} and 4^{th} floor levels, $x_5(t)$ and $x_4(t)$, and shows the first low-pass (LP) coefficient at each scale level, $f_i^{j,v}$, where $v = 0$, $j = 1 - 6$ and $i = 4, 5$. It is seen that the lowest frequency content become dominant at higher scale levels, whereas the high-pass (HP) coefficients successively contain the higher frequency waveforms and noise.

Fig. 3.14 shows the plots of the fourier spectra (FS) of $x_5(t)$, and the FS of the corresponding wavelet coefficients, $F_i^{j,0}(\omega)$, where $j = 1 - 6$ and $i = 5$. It is quite clear that the signals are more sparse (in its sources) with increasing scale. The high frequency noise is filtered until scale level 3, o. The 4^{th} and 5^{th} frequency sources are filtered at scale level 4. Proceeding to examine all the other LP/HP coefficients at this scale level, the 4^{th} or the 5^{th} mode, or both, can be then be estimated. The 3^{rd} source is filtered at the scale level 5 in a similar fashion. Thus, examining other LP/HP coefficients at this scale level, the 3^{rd}, 4^{th} and 5^{th} modes can be located, and this process repeated.

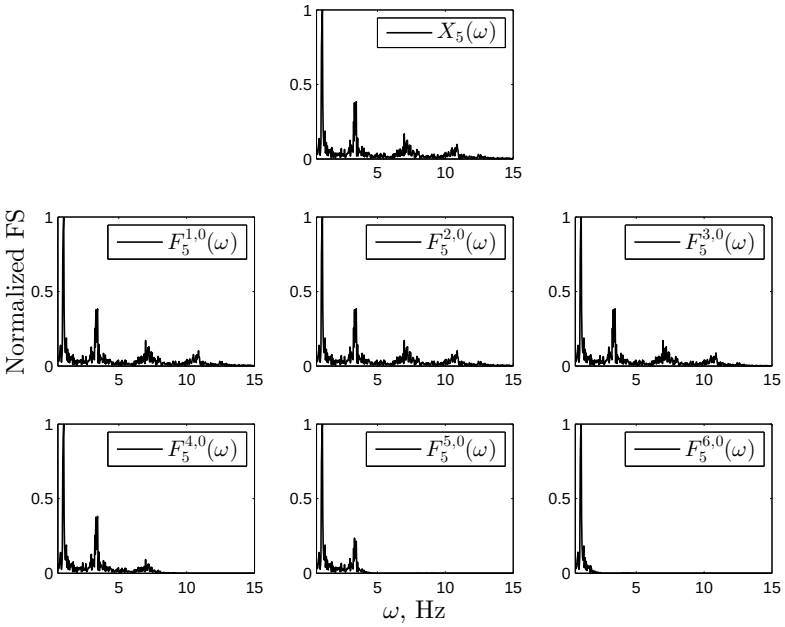

Figure 3.14: The normalized FS of $x_5(t)$ and $f_5^{j,0}(t)$ at various scale levels

The coefficients at highest scale level ($m = 2^s = 64$) of decomposition are used to estimate the mixing matrix coefficients. Out of these, the coefficients containing low-energy noisy components are rejected using a thresholding criterion based on RMS values [115]. The RMS values of the coefficients corresponding to $x_5(t)$ and $x_4(t)$ are shown in Fig. 3.15. The average (μ_{RMS}) of all the RMS values is shown using a dotted horizontal line in Fig. 3.15. The values of μ_{RMS} are obtained as 0.022 and 0.021 for $x_5(t)$ and $x_4(t)$ respectively. The total number of coefficients with RMS values greater than μ_{RMS}, are 10 and 11 in $x_5(t)$ and $x_4(t)$ respectively. To include all the significant energy coefficient pairs from both the floors, 11 coefficient pairs (i.e., higher of the two values 10 and 11) are included.

PCA is then undertaken using the 11 SWPT coefficient pairs. Two typical cases of coefficient pairs and their FS are shown in Fig. 3.16. For example, Fig. 3.16 shows the plots of $f_i^{6,0}(t)$ and $f_i^{6,12}(t)$ for $i = 4 - 5$. From the Fourier spectra, it can be observed that $f_i^{6,0}(t)$ is nearly mono-component, while $f_i^{6,12}(t)$ contains a mixture of modes. The

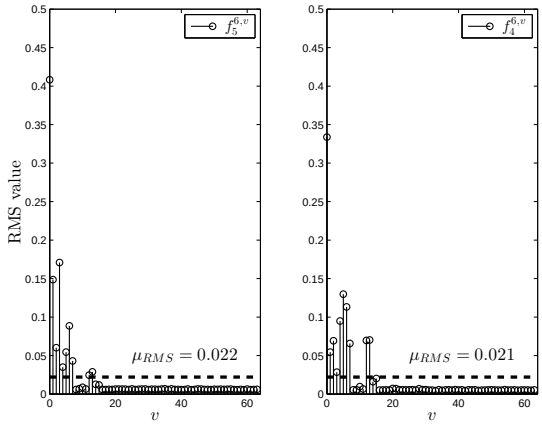

Figure 3.15: RMS values of the last scale level coefficients of $x_5(t)$ and $x_4(t)$ (SNR=100)

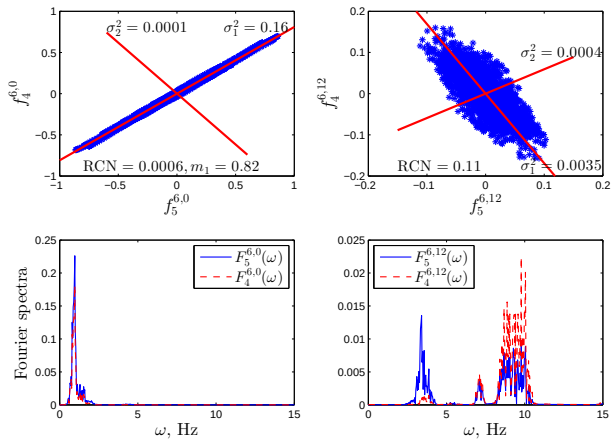

Figure 3.16: PCA of the SWPT coefficients, at $v = 0$ and $v = 12$

principal directions and the variances of the major and minor PCs are shown in Fig. 3.16. The corresponding RCN values are 0.0006 and 0.11 for $f_i^{6,0}(t)$ and $f_i^{6,12}(t)$, respectively. A lower value of RCN ($\ll 1$) in $f_i^{6,0}(t)$ indicates a nearly mono-component signal, and hence it is indicative of a structural mode. On the other hand, a higher value of RCN indicates mode mixing in $f_i^{6,12}(t)$, and is therefore discarded. Therefore the coefficients with smaller value of RCN are the most plausible candidate for the structural mode. If the number of desired target modes is n_t, then the coefficients with first n_t lowest RCN values can be selected as sources. In this example, the number of target modes is 5 and thus the

coefficients with first five lowest RCN are retained as the sources.

The major principal direction, or the slope of the major principal axis of $f_i^{6,0}(t)$ ($m_1 = 0.82$) are the normalized partial mixing matrix coefficients corresponding to $i = 4-5$. The resulting major and minor PCs of $f_i^{6,0}(t)$ are shown in Fig. 3.17. The natural frequency (ω) and damping (ξ) corresponding to the first mode are computed based on curve fitting the auto-correlation function of the major PC.

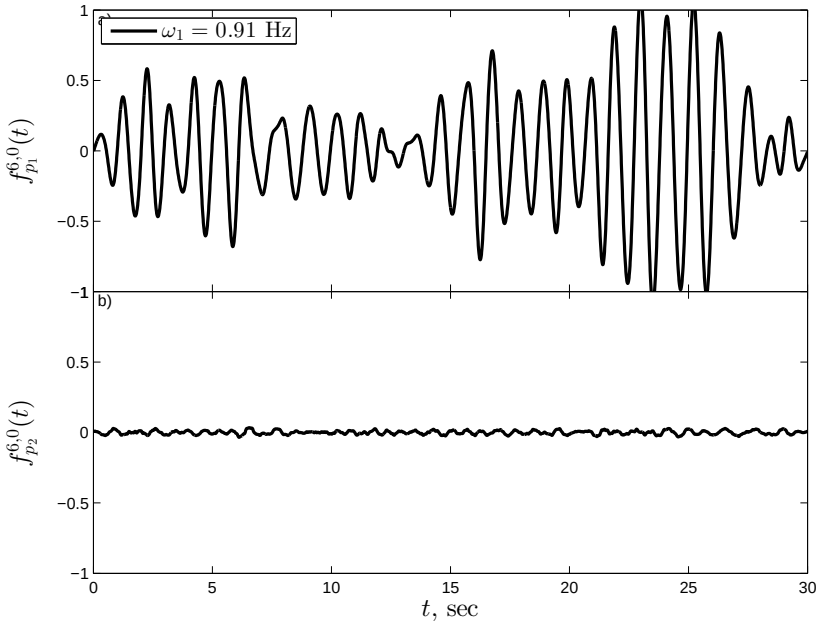

Figure 3.17: Major and Minor PCs of $f_5^{6,0}$ and $f_4^{6,0}$

This procedure is repeated for all the selected coefficients. Fig. 3.18 shows the major principal directions and the corresponding principal components for the 5 modes. The identification results are presented in Table 3.1. The absolute percentage error between the estimated and the theoretical values for the mixing matrix coefficients are presented as well. It can be seen that the absolute percentage error in all the modes is less than 5.8% for SNR= 100.

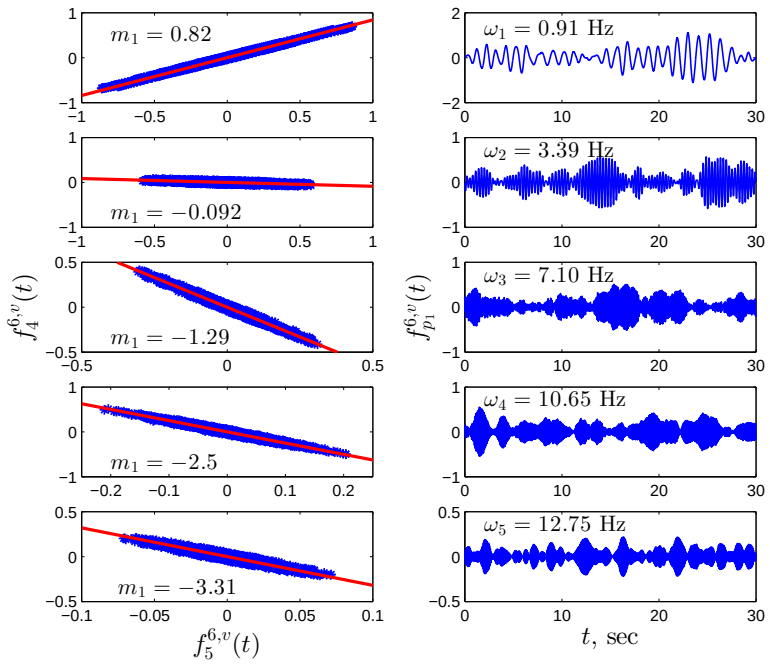

Figure 3.18: Major principal components of 5 modes

Construction of the full mixing matrix from partial mixing coefficients

Calculating the partial mixing coefficients from two sensors (corresponding to the 5^{th} and 4^{th} floor responses) has been explained thus far. This process can be repeated using a fixed or movable common reference sensor location, which is the essence of the decentralized sensing concept. The identification results for the first mode shape are illustrated in Tables 3.2, 3.3 and 3.4 for T_1, T_2 and T_3 cases, respectively. $\phi_{j,1}$ and $\hat{\phi}_{j,1}$ represents the true and estimated mode shape coefficient at the j^{th} DOF of ϕ_1. As shown in Eq. 3.33, $\hat{\phi}_{j,1}$ is simply the union of the partial mode shape coefficients, $\hat{\phi}_{j,1}^{Si}$ from each group (Si).

In this example, T_1 is selected for illustration purposes. This identification process is shown schematically in Fig. 3.19. Repeating the analysis described earlier yields 2×5 normalized partial mixing coefficient matrices A_{3j}, A_{2j} and A_{1j}, for each group. This matrix is spatially sparse, yet dense in frequencies, as it includes all the modes of the system. On

Table 3.1: Details of the identification results (SNR = 100)

j	RCN	ω_j	ξ_j	$A_{4j} = m_1$	$\mathbf{\Phi}_{4j}$	% error
1	0.0006	0.91	2.08	0.82	0.82	0.0
2	0.0187	3.39	1.98	−0.092	−0.087	5.7
3	0.0059	7.10	1.96	−1.29	−1.29	0.0
4	0.0088	10.65	1.95	−2.50	−2.52	0.8
5	0.0049	12.75	1.97	−3.31	−3.39	2.3

Table 3.2: Estimation of ϕ_1 using T_1 with SNR = 10

j	$\phi_{j,1}$	$\hat{\phi}^{S1}_{j,1}$ $(5-4)$	$\hat{\phi}^{S2}_{j,1}$ $(5-3)$	$\hat{\phi}^{S3}_{j,1}$ $(5-2)$	$\hat{\phi}^{S4}_{j,1}$ $(5-1)$	$\hat{\phi}_{j,1}$
5	1.0	1.0	1.0	1.0	1.0	1.0
4	0.82	0.82	–	–	–	0.82
3	0.59	–	0.59	–	–	0.59
2	0.34	–	–	0.34	–	0.34
1	0.11	–	–	–	0.12	0.12

the other hand, if existing methods such as ERA are used, the maximum theoretically obtainable modes with two sensors is two. In this respect the proposed method is capable of identifying nearly all the dominant modes of the system, even with two sensors, which is the main advantage. Since all of the matrices are normalized with respect to the 5^{th} floor location, the partial mixing matrices can be concatenated to yield the full mixing matrix. The MAC numbers obtained using Eq. 3.34 are greater than 0.98 for all the five modes. The calculated mode shapes are relatively insensitive to noise (reflected by the relatively high MAC values) even for SNR as high as 10 (as shown in Table 3.5). This can be attributed to the inherent de-noising capability of the wavelet filter-bank.

3.4 Summary

In this chapter, a new modal identification technique specifically tailored for decentralized processing was presented. The main advantage of the proposed method lies in the fact that only the data collected from a few sensors need to be processed at-a-time. The

Table 3.3: Estimation of ϕ_1 using T_2 with SNR = 10

j	$\phi_{j,1}$	$\hat{\phi}_{j,1}^{S1}$ $(5-4)$	$\hat{\phi}_{j,1}^{S2}$ $(4-3)$	$\hat{\phi}_{j,1}^{S3}$ $(3-2)$	$\hat{\phi}_{j,1}^{S4}$ $(2-1)$	$\hat{\phi}_{j,1}$
5	1.0	1.0	–	–	–	1.0
4	0.82	0.82	1.0	–	–	0.82
3	0.59	–	0.72	1.0	–	0.59
2	0.34	–	–	0.58	1.0	0.34
1	0.11	–	–	–	0.41	0.12

Table 3.4: Estimation of ϕ_1 using T_3 with SNR = 10

j	$\phi_{j,1}$	$\hat{\phi}_{j,1}^{S1}$ $(5-4-3)$	$\hat{\phi}_{j,1}^{S2}$ $(3-2-1)$	$\hat{\phi}_{j,1}$
5	1.0	1.0	–	1.0
4	0.82	0.82	–	0.82
3	0.59	0.59	1.0	0.59
2	0.34	–	0.58	0.34
1	0.11	–	0.21	0.12

measurements are sparsified using SWPT. Then, the principal components are calculated, which then yields the partial mixing matrix coefficients and the modal responses. The use of SWPT makes the proposed method robust to measurement noise. Partial mixing matrices are used to build the complete mode shape information. Unlike several popular ambient system identification methods, the proposed method yields partial mixing coefficients that are dense in frequencies. This is a significant advantage over many existing decentralized methods proposed in the literature. Numerical results show that the proposed method is effective in identifying the dominant modal characteristics of typical framed structures.

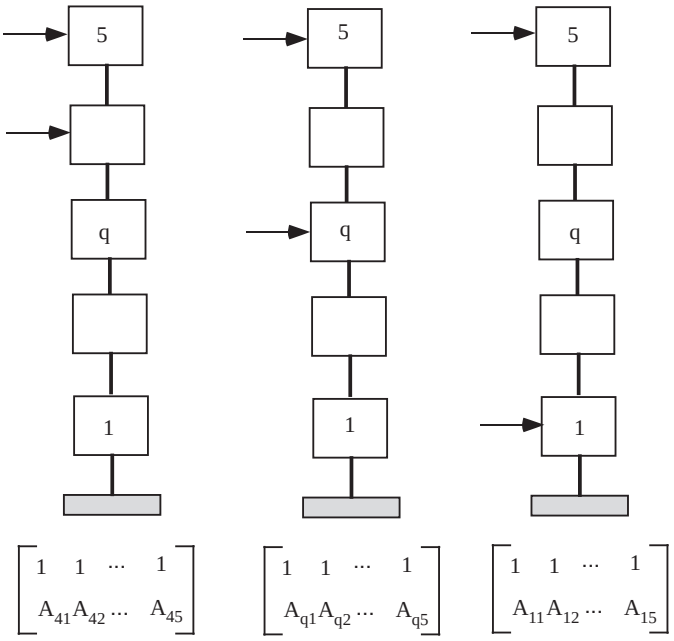

Figure 3.19: Sensor configuration to estimate the global mode shapes

Table 3.5: Effect of noise level in MAC numbers

j	SNR = 100	SNR = 20	SNR = 10
1	1.0	1.0	1.0
2	0.998	0.984	0.98
3	1.0	0.99	0.99
4	1.0	1.0	0.99
5	0.999	0.988	0.98

Chapter 4

Sparse BSS under narrowband sources

In this chapter, the framework of decentralized identification explained previously is extended to the case when narrow-band external excitations are present on the structure. Most modal identification schemes assume that the excitation is white and does not contain narrow band excitation frequencies. However, this assumption is not satisfied in many flexible structures where the excitations are a superposition of narrow-band harmonic(s) and broadband disturbances, e.g., rotating machinery fixed to flexible structures, human induced vibration in pedestrian bridges, or dynamic interaction with surrounding structures. Under such conditions, traditional BSS methods (such as SOBI) yield sources (modes) without any indication as to whether the identified source(s) is a system or an excitation harmonic. In such cases, the decentralized algorithm is augmented with a statistical characterization of the identified sources using residual bootstrap technique, which enables us to delineate the harmonic sources from physical modes of the structure. The performance of the algorithm is illustrated using a numerical study, which is the same test-bed used in the previous chapter.

4.1 Introduction

The issue of excitation harmonics contaminating ambient vibration results has previously been dealt with in the literature, e.g., [91, 92, 106, 6, 32, 90, 110]. In almost all cases, the harmonic frequency is assumed to be known *a priori*. The closest in concept to the method to be proposed here is an algorithm applied to the random decrement method proposed by [90]. The author used the conditional probability density function to estimate the harmonic sources. This was shown to perform well within the random decrement framework. Delineating excitation harmonics from source harmonics has also been dealt within the context of BSS [120, 154], where a modified principal component analysis is introduced in the whitening step of BSS. The underlying architecture in all these methods involves batch processing of sensor measurements, i.e., in a centralized architecture, where the number of measurements is more than the number of sources to be identified. This requires the measurements from a number of sensors to be processed together in order to identify the modes. Unlike this approach, here a decentralized approach is presented to deal with the issue of narrow-band harmonics in the measurements.

The key steps in the proposed method are as follows. First, a sub-set of raw vibrations are transformed using SWPT. This results in a sparse transformation of the signal (dense representation in the frequency domain) in the individual sub-bands in the decomposition. Then, the statistical characteristics of the SWPT coefficients are utilized to identify the modal parameters. First, the cross-correlation coefficient is computed over the SWPT coefficient pairs between two measurement channels containing the modal responses to identify the mono-component sources. Kurtosis is used as an indicator to identify the mono-component sources containing the modal responses and to delineate the sources corresponding to the excitation harmonics. Finally, the standard deviation of selected mono-component coefficients pairs are used to estimate the mode shape coefficients. The natural frequency and damping are estimated based on the time structure of the mono-component

wavelet coefficients. In order to quantify the uncertainty in the estimates, a residual bootstrap technique [34, 161] is employed. This allows us to quantify the uncertainty in the estimates, which is especially useful when dealing with experimental data of small sample sizes.

4.2 Background

When harmonic disturbances are mixed in broad-band excitations (broad-band with respect to the structure frequencies), these disturbances will directly feed-through to the sources, which are then identified as source components in the BSS results. Since the process of BSS is blind to scaling and permutation of sources (and modes), it is not obvious which ones are the physical sources versus the spurious ones. In order to address this issue, the probabilistic features of the sources are estimated and then used to delineate modal sources from the excitation sources, as discussed next.

4.2.1 Statistical characterization of sources

Statistical characterization of modal responses play key role in the delineation process. According to classical Wold's decomposition theorem [97], any time series data can be considered as the summation of deterministic (y_d) and random component (y_r):

$$y(t) = y_d(t) + y_r(t) \tag{4.1}$$

The deterministic part consists of periodic excitations coming from several possible sources, that can generalized as $y_d = \sum_{i=1}^{p} y_{d_0,i} \sin(\omega_i t)$, where p is the number of periodic components in the excitation. On the other hand, the stochastic component $y_r(t) = \sum_{i=1}^{q} y_{r,i}$ arises due to wind or earthquake like random excitations, where q is the number of stochas-

tic excitations. The random excitation is primarily characterized using probabilistic sense (say, a zero-mean Gaussian distribution).

Due to stochastic nature of the excitation, the structural response becomes inherently a random variable. Response of a single-degree-of-freedom dynamical system subjected to the excitation $y(t)$ as in Eq. 4.1 can be expressed as:

$$x(t) = x_d(t) + x_r(t) \tag{4.2}$$

where $x_d(t) = \sum_{i=1}^{p} x_{d,i}(t) = \sum_{i=1}^{p} x_{d_0,i} \sin(\omega_i t + \phi_i)$ is the contribution by the deterministic component. When the time t is not precisely specified and arbitrary in nature, the analytical PDF of $x_{d,i}(t)$ can be expressed as [97]:

$$p(x_{d,i}) = \frac{1}{\pi\sqrt{x_{d_0,i}^2 - x_{d,i}^2}} \qquad -x_{d_0,i} \leq x_{d,i} \leq x_{d_0,i} \tag{4.3}$$

The $p(x_{d,i})$ has two distinct peaks and yields a *bath-tub* curve with a value of infinity at $x_{d,i} = \pm x_{d_0,i}$. On the hand hand, $x_r(t) = \sum_{i=1}^{q} x_{r,i} = \sum_{i=1}^{q} \int_{-\infty}^{t} h(t) * y_{r,i}(t)$ is the stochastic component of the response, where $h(t)$ is the impulse response function. It can be shown that if $y_{r,i}(t)$ is a Gaussian process, then $x_{r,i}(t)$ is also a gaussian process with *bell-shaped* distribution [97]:

$$p(x_{r,i}) = \frac{1}{\sqrt{2\pi}\sigma} \exp\left(-\frac{(x_{r,i} - \mu)^2}{2\sigma^2}\right) \tag{4.4}$$

where, μ and σ are the mean and standard deviation of $x_{r,i}$. Therefore, by looking into the shape (i.e, bath-tub curve, bell-shaped or bi-modal curve) of the PDF of the response, the type of excitation (i.e, periodic, random or mixture of them respectively) can be identified [18]. In order to quantify the normality of the response, kurtosis (κ) can be used as one of the indicator,

$$\kappa_x = E\left[\left(\frac{x - \mu}{\sigma}\right)^4\right] \tag{4.5}$$

It may be noted that $\kappa_x = 3.0$ for Gaussian data such as $x_r(t)$, which is the response of the SDOF system under random excitation primarily containing the modal responses. On the other hand, for deterministic harmonic data such as $x_d(t)$, which is the response of the SDOF system under harmonic excitation containing mainly the excitation component, $\kappa_x = 1.5$ [97]. When both the harmonic and random data is mixed together, $1.5 \leq \kappa_x \leq 3.0$.

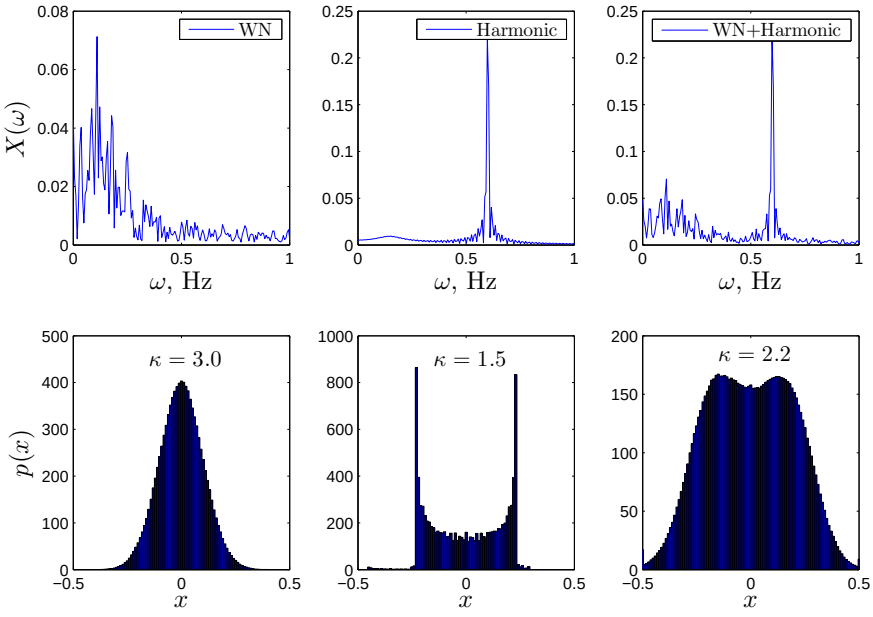

Figure 4.1: PDF of the response

In order to illustrate this concept, a SDOF system is used as an example. The natural frequency of the system is assumed to be 0.16 Hz. Three types of excitations are used: (a) Gaussian white noise ($q = 1$) (WN), (b) harmonic ($p = 1$) with a frequency of 0.6 Hz, (c) mixture of (a) and (b). The Fourier spectra and the PDF of the response are shown in Fig. 4.1. It is seen that the response $x(t)$ follows the *bell-shaped* Gaussian PDF (with a κ value of 3.0), which is the modal response with a frequency of 0.16 Hz. On the other hand, the $x(t)$ having a bath-tub PDF (with a κ value of 1.5) contains the harmonic excitation at a frequency of 0.6 Hz. In the case of mixed excitation, a bi-modal behavior is obtained

with a κ value of 2.2. Though in real measurements these numbers may not be exact, the overall idea can be used as a good indicator to identify the structural modes amongst the narrow band sources that are extracted using the system identification method. This is the key idea of the algorithms to be explained next.

4.2.2 Residual bootstrap technique

While dealing with practical data, especially in decentralized settings, the sample sizes are generally small to achieve good statistical characterization of the identified sources. The bootstrap technique [34] (a re-sampling method) allows us to overcome this limitation. Bootstrap is more computationally efficient in that unlike the Monte Carlo technique experiments need not be repeated. Rather, it involves re-sampling already acquired results, which is attractive in situations dealing with system identification where repeating experiments can be expensive and time-consuming. Bootstrapping has also been implemented in the context of uncertainty quantification in system identification methods such as random decrement method and sub-space methods [14, 63, 145].

The original intent of bootstrap was to deal with small sample sizes of independent and identically distributed data. Let $\Upsilon = \{Y_1, Y_2, ..., Y_n\}$ represent a collection of n independent and identically distributed numbers drawn randomly from an unknown distribution P. Let δ be an unknown parameter of P which needs to be derived from the sample Υ (e.g., mean, standard deviation). In its non-parametric version, a new sample with replacement from Υ is generated so that each Y_i^* has probability $\frac{1}{n}$ of being equal to any one of the Y_j^* and the new sample is called a bootstrap sample $\Upsilon_i^* = \{Y_1^*, Y_2^*, ..., Y_n^*\}$ [34, 161]. An estimate of the unknown parameter $\hat{\delta}_i^*$ is obtained from Υ_i^*. When we repeat such bootstrapping for $i = 1, 2, ..., B$, where B is the number of bootstrapping, an accurate statistical estimate of δ such as mean, variance or confidence intervals can be obtained from $\{\delta_1^*, \delta_2^*, ..., \delta_B^*\}$ [42]. For example, the variance $\sigma_{\hat{\delta}}^2$ of the unknown parameter $\hat{\delta}$ can

be estimated by:

$$\sigma_{\hat{\delta}}^2 = \frac{1}{(B-1)} \sum_{i=1}^{B} (\hat{\delta}_i^* - \frac{1}{B} \sum_{j=1}^{B} \hat{\delta}_j^*)^2 \tag{4.6}$$

Vibration measurements are time-correlated data for which the independence assumption in traditional bootstrap is not valid. There are basically two approaches presented in the literature to overcome this issue. The first method is known as the *moving-block method* and the second is known as *bootstrapping residuals* method [14]. The moving-block method has been used in the literature in the context of modal parameter uncertainty estimation [63, 145], and it involves partitioning a data set into n blocks, and treating these blocks of data as satisfying independence assumption. It is obvious that this method requires a prior knowledge of the correlation structure to determine n, and could suffer from end-effects if the blocks are randomly concatenated. Alternatively, in the residual method, an auto-regressive moving average (ARMA) model [103, 16] is fitted to the data. This model consists of a deterministic auto-regressive part and random residuals or innovation components. The ARMA model which relates the output y_t with input a_t is expressed in the following form:

$$y_t - \phi_1 y_{t-1} - \phi_2 y_{t-2} - ..... - \phi_p y_{t-p} = a_t - \theta_1 a_{t-1} - \theta_2 a_{t-2} - ..... - \theta_q a_{t-q} \tag{4.7}$$

Using B operator, Eq. 4.7 can be expressed as:

$$\begin{aligned} (1 - \phi_1 B - \phi_2 B^2 - ..... - \phi_p B^p) y_t &= (1 - \theta_1 B - \theta_2 B^2 - ..... - \theta_q B^q) a_t \\ \phi(B) y_t &= \theta(B) a_t \end{aligned} \tag{4.8}$$

where $\phi(B)$ and $\theta(B)$ contain the AR (auto-regressive) and MA (moving average) parameters respectively. a_t is the zero-mean identically and independently distributed (IID) sequence characterized by its variance, σ_a^2. The AR part of order p describes the system dynamics while MA part of order q is related to external disturbances. Since the residuals

a_t are white [103, 16], the residual sequence can be bootstrapped instead of the raw data. This is the approach taken in this algorithm.

The main parameters in representing vibration data using ARMA models are the model orders p and q, and the associated parameters, $\phi(B)$ and $\theta(B)$. As will be discussed in the next section, bootstrap results will be used not only to quantify the uncertainty in the parameter estimates, but also to delineate the sources. Hence, it is important to implement a model with low p and q, which is not possible using raw vibration data. Hence, the wavelet coefficients at various scale levels will be bootstrapped, since these are nearly mono component and hence yield low model orders $p = 2,\ q = 1$ [5, 94]. $\phi(B)$ and $\theta(B)$ are estimated using Maximum Likelihood Estimation [103, 16].

Once the model parameters are estimated, the residual sequence is estimated as $\hat{\mathbf{a}} = \hat{\theta}(B)^{-1}\hat{\phi}(B)\Upsilon$ using the inverse expression of Eq. 4.8. Since $\hat{\mathbf{a}}$ is IID, bootstrapping can be performed to generate a bootstrap innovation $\hat{\mathbf{a}}_\mathbf{1}^*$ by re-sampling $\hat{a}_1, \hat{a}_2, \hat{a}_3, ..., \hat{a}_N$ with replacement from the estimated residual sequence, $\hat{\mathbf{a}}$. Subsequently the bootstrapped modal response Υ_1^* is estimated using $\Upsilon_1^* = \hat{\phi}(B)^{-1}\hat{\theta}(B)\mathbf{a}_\mathbf{1}^*$ as in Eq. 4.8. In doing so, the statistical measures δ_1^* such as the standard deviation and kurtosis for the bootstrap samples can be estimated with better confidence using Υ_1^*.

4.3 Details of the Algorithm

The measurement at the i^{th} degree-of-freedom ($i = 1, 2, ..., n_m$) of Eq. 3.4 can be expressed as

$$x_i(t) = \sum_{r=1}^{n_s} \psi_{ir} q_r(t) \tag{4.9}$$

Consistent with the notation of BSS for the static mixtures case in Eq. 2.2, we can write the measurement at the i^{th} location:

$$x_i(t) = \sum_{l=1}^{n_s} A_{il} s_l(t) \qquad i = 1, 2, ..., n_m \tag{4.10}$$

Considering the wavelet packet decomposition of the sensor responses and the sources at any specific node (j, v), and finally applying the orthogonality condition [107] for wavelets, Eq. 4.10 yields [115]:

$$f_{k,i}^{j,v}(t) = \sum_{l=1}^{n_s} A_{il} e_{k,l}^{j,v}(t) \qquad i = 1, 2, ..., n_m \tag{4.11}$$

Considering only the highest level coefficients $(j = s)$, the coefficients at the s^{th} scale level contain both the sparse modal responses and the high frequency noise components. At the last scale level, assuming only one source is active in each sub-band after decomposition, Eq. 4.11 can be written as:

$$f_{k,i}^{s,v}(t) = A_{il} e_{k,l}^{s,v}(t) \qquad i = 1, 2, ..., n_m \tag{4.12}$$

Eq. 4.12 relates the SWPT coefficients of i^{th} measurement with the SWPT coefficients of the sparse l^{th} source. Therefore, following the same logic for $i = q$ and $i = r$ in Eq. 4.12, the partial mixing matrix coefficients of q^{th} sensor measurement normalized with the r^{th} measurement is:

$$\frac{f_{k,q}^{s,v}}{f_{k,r}^{s,v}} = \frac{A_{ql} e_{k,l}^{s,v}(t)}{A_{rl} e_{k,l}^{s,v}(t)} = \frac{A_{ql}}{A_{rl}} = a_{ql}; \qquad l = 1, 2, ...n_s \tag{4.13}$$

Then, $a_{ql} = \frac{A_{ql}}{A_{rl}}$ represents the estimated normalized mixing matrix coefficient of the

l^{th} mode at the q^{th} DOF. Therefore, we get:

$$f_{k,q}^{s,v} = a_{ql} f_{k,r}^{s,v} \tag{4.14}$$

If we pre-multiply both side with $f_{k,q}^{Ts,v}$ and take the expectation both sides, Eq. 4.14 can be simplified as:

$$\begin{aligned} \sigma_{f_{k,q}^{s,v}} &= |a_{ql}| \sigma_{f_{k,r}^{s,v}} \\ |a_{ql}| &= \frac{\sigma_{f_{k,q}^{s,v}}}{\sigma_{f_{k,r}^{s,v}}} \end{aligned} \tag{4.15}$$

where, $\sigma_{f_{k,i}^{s,v}}$ is the standard deviation of $f_{k,i}^{s,v}$. In order to estimate the sign of a_{ql}, the cross-correlation coefficient (ρ) between $f_{k,q}^{s,v}$ and $f_{k,r}^{s,v}$ can be used. We know that

$$\rho_{f_{k,q}^{s,v}, f_{k,r}^{s,v}} = \frac{E[f_{k,q}^{s,v}.f_{k,r}^{Ts,v}]}{\sigma_{f_{k,q}^{s,v}} \times \sigma_{f_{k,r}^{s,v}}} = \frac{a_{ql}.\sigma_{f_{k,r}^{s,v}}^2}{|a_{ql}| \sigma_{f_{k,r}^{s,v}}.\sigma_{f_{k,r}^{s,v}}} = \pm 1 \tag{4.16}$$

Thus the cross-correlation coefficient with a value of ± 1.0 indicates the presence of a mono-component source. Further, the absolute value of the mixing coefficient a_{ql} can be estimated using Eq. 4.15 and the sign of ρ (i.e., $\frac{|\rho|}{\rho}$) in Eq. 4.16 can be used to estimate the true value of a_{ql}.

$$a_{ql} = \frac{|\rho_{f_{k,q}^{s,v}, f_{k,r}^{s,v}}|}{\rho_{f_{k,q}^{s,v}, f_{k,r}^{s,v}}} \frac{\sigma_{f_{k,q}^{s,v}}}{\sigma_{f_{k,r}^{s,v}}} \tag{4.17}$$

Using this procedure, the normalized partial mixing matrix coefficients can be estimated using SWPT coefficients of partial sensor measurements at the highest scale level. A thresholding criteria based on average root-mean-square (RMS) value of the coefficients can be used to retain coefficients with significant energy [115].

Filter banks constituted out of the wavelet packets have overlapped frequency contents due to imperfect filtering [115]. This sometimes leads to multi-component sources in the

WPT coefficients. However, Eq. 4.12 and Eq. 4.13 are valid only when the coefficients are mono-component signals. In order to identify the mono-component sources in the wavelet coefficients, the cross-correlation between $f_{k,q}^{s,v}$ and $f_{k,r}^{s,v}$ is used, and if more than one source is detected, such coefficients are discarded. For the simple case consisting of a mixture of two sources ($l = m, n$) present in $f_{k,i}^{s,v}$ as in Eq. 4.11,

$$\begin{aligned} f_{k,r}^{s,v} &= A_{rm} e_{k,m}^{s,v} + A_{rn} e_{k,n}^{s,v} \\ f_{k,q}^{s,v} &= A_{qm} e_{k,m}^{s,v} + A_{qn} e_{k,n}^{s,v} \end{aligned} \tag{4.18}$$

Since $e_{k,m}^{s,v}$ and $e_{k,n}^{s,v}$ are uncorrelated, i.e., $E[e_{k,m}^{s,v}.e_{k,n}^{Ts,v}] = 0$, the cross-correlation of the coefficients yields,

$$\rho_{f_{k,q}^{s,v} f_{k,r}^{s,v}} = \frac{E[f_{k,r}^{s,v}.f_{k,q}^{Ts,v}]}{\sigma_{f_{k,r}^{s,v}}.\sigma_{f_{k,q}^{s,v}}} = \frac{E[(A_{rm}e_{k,m}^{s,v} + A_{rn}e_{k,n}^{s,v}).(A_{qm}e_{k,m}^{s,v} + A_{qn}e_{k,n}^{s,v})]}{\sqrt{(A_{rm}^2\sigma_{e_{k,m}^{s,v}}^2 + A_{rn}^2\sigma_{e_{k,n}^{s,v}}^2)}\sqrt{(A_{qm}^2\sigma_{e_{k,m}^{s,v}}^2 + A_{qn}^2\sigma_{e_{k,n}^{s,v}}^2)}} \tag{4.19}$$

the above expression can be simplified as:

$$\rho_{f_{k,q}^{s,v}, f_{k,r}^{s,v}} = \frac{A_{rm}A_{qm}\sigma_{e_{k,m}^{s,v}}^2 + A_{rn}A_{qn}\sigma_{e_{k,n}^{s,v}}^2}{\sqrt{(A_{rm}^2\sigma_{e_{k,m}^{s,v}}^2 + A_{rn}^2\sigma_{e_{k,n}^{s,v}}^2)}\sqrt{(A_{qm}^2\sigma_{e_{k,m}^{s,v}}^2 + A_{qn}^2\sigma_{e_{k,n}^{s,v}}^2)}} \tag{4.20}$$

Since $m \neq n$,

$$\rho_{f_{k,q}^{s,v}, f_{k,r}^{s,v}} \neq \pm 1 \tag{4.21}$$

Thus, the cross-correlation of the coefficients can be used as an indicator for source mixing. When there is no mode mixing, $\rho_{f_{k,q}^{s,v}, f_{k,r}^{s,v}} \to \pm 1$ as in Eq. 4.16. On the other hand $\rho_{f_{k,q}^{s,v}, f_{k,r}^{s,v}} \neq 1$ when mode mixing is present, as in Eq. 4.21.

4.3.1 Delineating excitation sources from modal harmonics and generating bootstrap estimates

As described in the background section, kurtosis contains information regarding the nature of the underlying density of the identified sources. For a sample realization, this is given by:

$$\kappa_x = E\left[\left(\frac{x-\mu}{\sigma}\right)^4\right] \tag{4.22}$$

A value close to 3 indicates modal sources, while lower values indicate the presence of harmonic excitation frequency. Once a source containing modal response is detected, then Eq. 4.17 is utilized to estimate the partial mode shape matrix. However, in order to estimate the statistical measures such as kurtosis and standard deviation of the underlying density function, a sufficiently large sample size is required. In order to circumvent this issue, several bootstrapped samples are generated using the residual bootstrap method described in the background section. The 98% confidence interval of kurtosis obtained from bootstrapping is used to delineate the excitation harmonics from modal harmonics.

The bootstrap procedure is implemented as follows. First, the measurements are transformed to the wavelet domain using SWPT. $\Gamma_q = \{f_{k,q}^{s,v}\}_{N\times 1}$ and $\Gamma_r = \{f_{k,r}^{s,v}\}_{N\times 1}$ correspond to the SWPT of the measurements from two sensors ($i = q, r$). Then, using ARMA (2,1) modeling of the coefficients, the innovations of SWPT coefficients are estimated. The bootstrap samples $\Gamma_{q,1}^*$ and $\Gamma_{r,1}^*$ are obtained by using the bootstrap innovations as illustrated in the background section and then the unknown parameters are estimated $\delta_1^* = \sigma_{f_{k,i}^{s,v}}, \kappa_{f_{k,i}^{s,v}}$ for $i = q, r$. This step is repeated for $m = 1, 2, 3, ..., B$, where B is the number of bootstrap samples, which then yields the required parameter statistics.

4.3.2 Estimation of modal parameters

Once the modal responses are identified, the modal frequencies and damping are estimated from the SWPT coefficients by treating them as single-degree-of-freedom systems. Due to the shift-invariance property of SWPT coefficients [95], the time structure of SWPT coefficients i.e., the modal responses, are unaffected. Modal frequencies are identified by using the Fourier transform of the modal responses as selected by the proposed method. For the damping estimation, autocorrelation functions of the modal responses are first estimated. Modal damping is then identified by fitting an exponential decay to the relative maxima of the auto-correlation function [69, 127]. Subsequently, the partial mode shape coefficients $\Phi_{2\times n_s}$ are estimated using Eq. 4.17 by utilizing the relevant SWPT coefficients containing the modal responses. Finally the full modeshape matrix is obtained by using Eq. 3.33 employing the decentralized architecture.

The key steps involved in the algorithm (for two measurement channels) are listed below for estimation of modal parameters.

Key steps of the proposed algorithm

- Obtain two channels of measurements, x_q and x_r.
- Perform SWPT for these measurements, up to scale level s, which yields $f_{k,q}^{s,v}$ and $f_{k,r}^{s,v}$ for $v = 1 - 2^s$.
- Apply the energy-based thresholding criteria to eliminate the SWPT coefficients associated with noise.
- Estimate the cross-correlation coefficient between the SWPT coefficient pairs, and retain only those coefficients with $|\rho| \to \pm 1$ which are mono-component sources.
- Perform the residual-based bootstrap technique to each SWPT coefficient pair, and estimate the statistics of standard deviation and kurtosis.

- Use 98% confidence interval of kurtosis to detect excitation harmonics amongst the mono-component sources and discard them.

- Estimate the modal frequencies and damping from the mono-component sources. Eq. 4.17 is then used to estimate the normalized mixing matrix coefficients and subsequently the partial mixing matrix $\Phi_{2\times n_s}$ is formed.

The above steps are repeated for two measurements at-a-time, and the results from each intermediate step are combined to yield the complete modal information by utilizing Eq. 3.33.

4.4 Numerical Study

The same 5-DOF example ($n_s = 5$) used previously is excited by a zero mean unit variance Gaussian white noise at all the floor levels. In addition to the white noise, a harmonic frequency 5.1 hz is added to the excitation. This harmonic is well-separated from the resonant frequencies of the structure. Fig. 4.2 shows the Fourier spectra of the response at the 5^{th} and the 4^{th} floors contaminated with a measurement noise containing a SNR of 100. Please note that these values are arbitrary, and other frequencies yield similar results.

The SOBI method [13] is first employed to extract the mixing matrix using all the floor responses. Due to presence of harmonics, SOBI, which is based on the assumption of white noise inputs, is unable to separate out the sources. Fig. 4.3 shows a significant amount of mode mixing in the separated sources using SOBI, which leads to significant estimation errors in the mixing matrix (modes).

The proposed method is then applied to the partial measurements. Two response measurements at the 5^{th} and the 4^{th} floors are processed using SWPT up to scale level $s = 6$. The maximum scale level is selected based on the sampling frequency (f_s) of 100 Hz

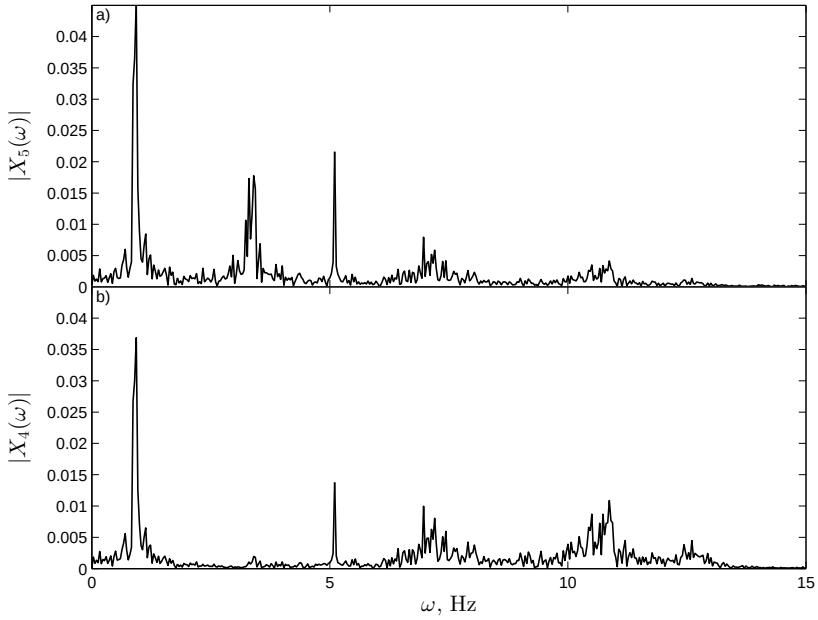

Figure 4.2: Fourier spectrum of the response

and the magnitude of the lowest frequency (f_l) of the signal (0.91 Hz). For this example, this leads to $s = 6$ ($f = \frac{100}{2^6} = 1.56$ Hz$>$ 0.91 Hz). $db5$ wavelet basis is chosen, though other orthogonal bases such as Symlet also produce consistent results. The coefficients at the last scale level ($2^s = 64$) of decomposition are used to estimate the partial mixing matrix. Of these, the coefficients containing low-energy noisy components are discarded using a thresholding criterion based on RMS values [118].

In order to identify the modal parameters from SWPT coefficients, the sample probability density of the selected SWPT coefficients of $x_5(t)$ and $x_4(t)$ are used. Fig. 4.4 shows the details of the identification using the information of PDF of $f_5^{6,v}$ and $f_4^{6,v}$. The first two columns of Fig. 4.4 show the PDF of SWPT coefficients $f_i^{6,v}$ for $v = 0, 2, 4$ and 5 for $i = 5$ and $i = 4$ respectively. In these sub-figures κ and σ represent the kurtosis and standard deviation of the corresponding PDF respectively. The third column shows the Fourier spectra of the coefficients, where the cross-correlation (i.e., ρ) of the SWPT coefficients and the resulting mode shape coefficient are reported. It can be seen that the PDF of $f_i^{6,v}$

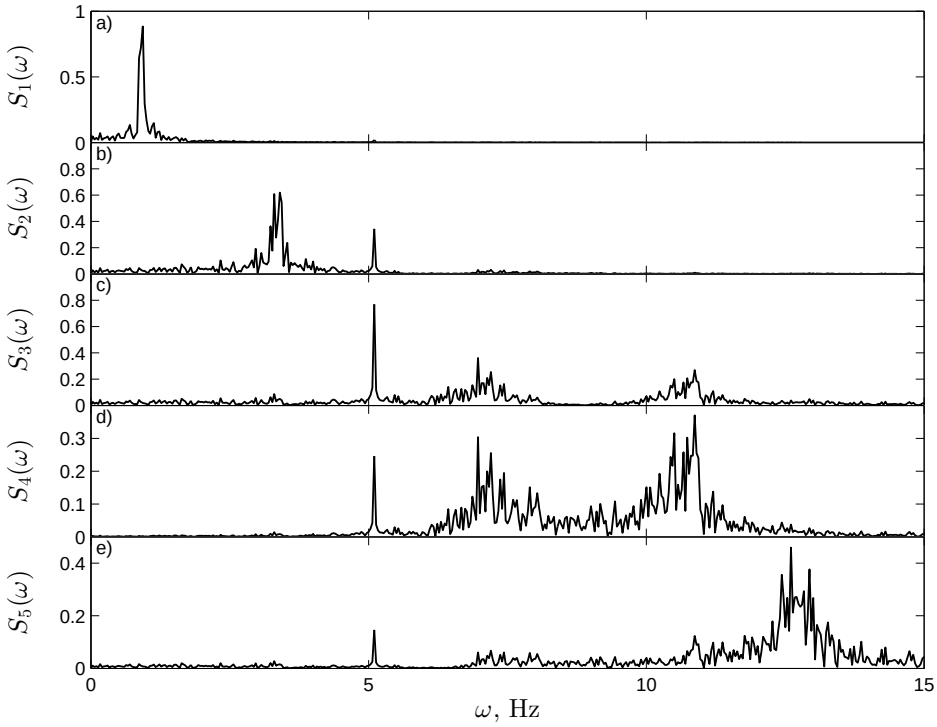

Figure 4.3: Fourier spectrum of the separated sources using SOBI

with $v = 0$ and 5 have the value of κ close to 3.0, which corresponds to belonging to a system mode. The absolute value of cross-correlation $\rho_{5,4}$ for those coefficients close to 1.0 implies a mono-component source, which can be considered as a modal response. The ratio of their standard deviation yields the mode shape coefficient and the sign of ρ determines the sign of the mode shape coefficients. In this fashion, the mixing coefficients can be estimated repeatedly using Eq. 4.17. For example, $f_5^{6,0}$ and $f_4^{6,0}$ have ρ value of $+0.99$ and standard deviation of 0.41 and 0.335 respectively, for which $\phi_{4,j}$ becomes $\frac{0.335}{0.41} = +0.82$. On the other hand, $f_5^{6,5}$ and $f_4^{6,5}$ have a ρ value of -0.99 and standard deviation of 0.062 and 0.156 respectively, for which $\phi_{4,j}$ is computed as $\frac{0.156}{0.062} = -2.51$.

Although the PDF of $f_i^{6,4}$ has the value of κ close to 3.0, the cross-correlation between $f_5^{6,4}$ and $f_4^{6,4}$ is -0.72 ($|\rho| \neq 1$). It implies that the coefficients contain mode mixing which is evident from the associated Fourier spectrum and thus it is rejected to be considered as a

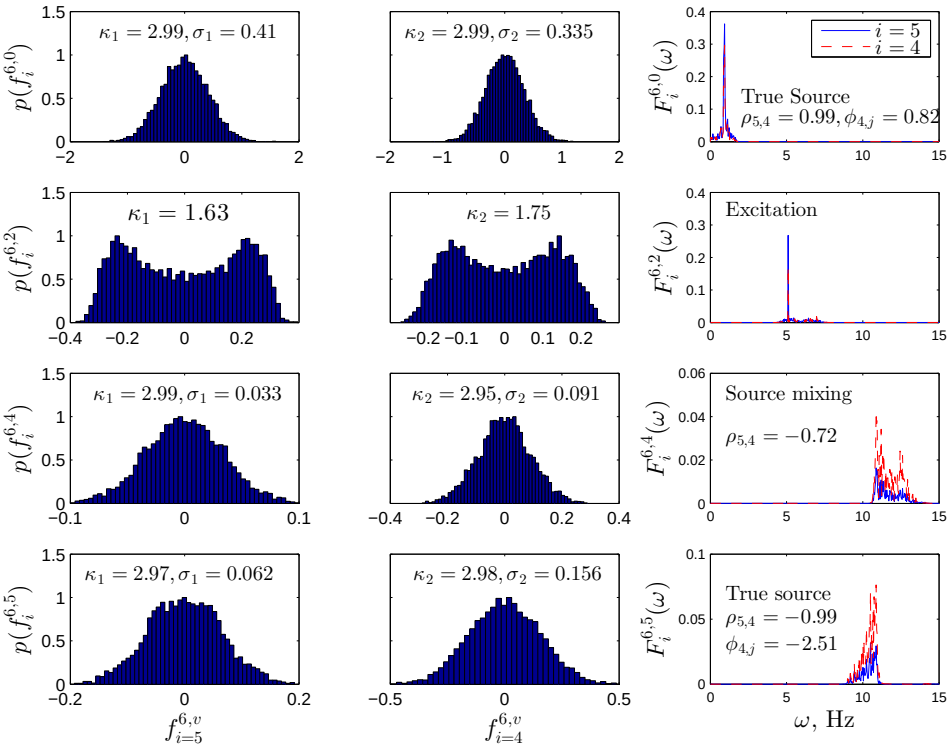

Figure 4.4: Details of identification using the PDF of $f_5^{6,v}$ and $f_4^{6,v}$

modal response. The PDF of $f_i^{6,2}$ has the value of $\kappa << 3.0$, which implies that the source is an excitation harmonic which is then discarded from further analysis. It can be seen that the coefficient $f_i^{6,2}$ accurately separates the excitation harmonic with a frequency of 5.1 Hz. The results are finally summarized for all coefficients containing the modal response in Table 4.1.

Uncertainty quantification

As mentioned earlier, the estimates of the probabilistic measures such as standard deviation, kurtosis, and the cross-correlation coefficients are key ingredients for the modal parameter estimation procedure. In the following, the uncertainty in estimating these quan-

Table 4.1: Details of the identification results

j	$\rho_{5,4}^{6,v}$	ω_j	ξ_j	$a_{4,j}^v = \frac{\sigma_4^{6,v}}{\sigma_5^{6,v}}$	$A_{4j} = (+/-)a_{4,j}^v$	$\mathbf{\Phi}_{4j}$	% error
1	0.999	0.91	2.07	0.82	0.82	0.82	0.0
2	−0.997	3.39	1.99	0.093	−0.093	−0.087	5.8
3	−0.991	7.10	1.97	1.288	−1.288	−1.29	0.16
4	−0.992	10.65	1.96	2.51	−2.51	−2.52	0.8
5	−0.993	12.75	1.97	3.32	−3.32	−3.39	2.1

tities from limited measurement data is undertaken using the residual bootstrap method presented in the previous section. The residuals of the ARMA model corresponding to the last scale level for several sub-bands v are treated as IID. Fig. 4.5 shows typical SWPT coefficients $f_5^{6,5}$ (containing modal response with a frequency of 10.65 Hz) and the estimated distribution of its standard deviation and kurtosis (with 98% confidence interval) resulting from the bootstrapping process. The first and second statistic of the standard deviation is 0.062 with a coefficient of variation c_v of 3.1%. The mean value of kurtosis is obtained as 2.97 with lower confidence limit (LCL) of 2.94 and and upper confidence limit (UCL) of 3.0. Since the 98% confidence interval of kurtosis includes a value of 3.0, the corresponding SWPT coefficients are used for the modal parameter estimation as shown in Fig. 4.4 corresponding to $f_{i=5}^{6,5}$.

Once the modal responses are identified, the natural frequency and damping are estimated using time structures of the corresponding SWPT coefficients. For example, SWPT coefficient $f_5^{6,5}$ as shown in first plot of Fig. 4.5, is a modal response which is identified in Fig. 4.4. The associated modal frequency is estimated as 10.65 Hz. In order to estimate the modal damping, the auto-correlation function of $f_5^{6,5}$ is utilized. The best-fit exponential envelope of the auto-correlation function yields a damping of 1.98% which closely agrees with the theoretical damping value (2%) of the associated mode.

Calculating the partial mixing coefficients from two sensors (corresponding to the 5^{th} and 4^{th} floor responses) has been explained thus far. This process can be repeated using a

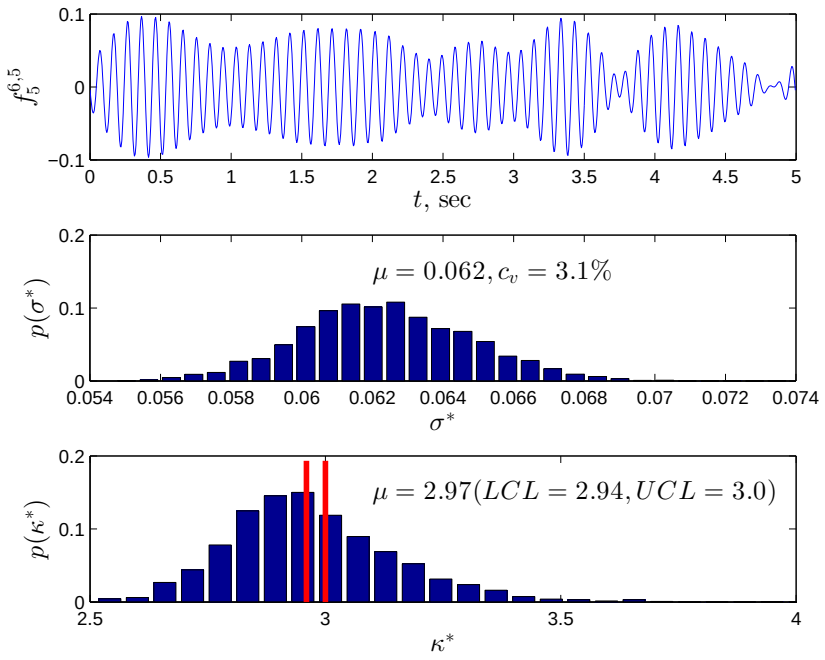

Figure 4.5: Typical bootstrapping results of $f_5^{6,5}$

fixed or movable common reference sensor location, which is the essence of the decentralized sensing concept (explained in Chapter 3). Partial mixing matrix coefficients so obtained can be concatenated using Eq. 3.33. The identification results for the first mode shape are summarized in Table 4.2 using topology T_1 of previous chapter.

Table 4.2: Estimation of ϕ_1 using a typical topology with SNR= 10

j	$\phi_{j,1}$	$\hat{\phi}_{j,1}^{S1}$ $(5-4)$	$\hat{\phi}_{j,1}^{S2}$ $(5-3)$	$\hat{\phi}_{j,1}^{S3}$ $(5-2)$	$\hat{\phi}_{j,1}^{S4}$ $(5-1)$	$\hat{\phi}_{j,1}$
5	1.0	1.0	1.0	1.0	1.0	1.0
4	0.82	0.82	–	–	–	0.82
3	0.59	–	0.58	–	–	0.58
2	0.33	–	–	0.34	–	0.34
1	0.11	–	–	–	0.12	0.12

Details of the identified natural frequencies and damping are also reported in Table 4.3.

Table 4.3: Identified modal parameters under various noise levels

	True values		SNR=100			SNR=20			SNR=10		
j	ω_j	ξ_j	$\hat{\omega}_j$	$\hat{\xi}_j$	MAC	$\hat{\omega}_j$	$\hat{\xi}_j$	MAC	$\hat{\omega}_j$	$\hat{\xi}_j$	MAC
1	0.91	2.0	0.91	2.07	1.0	0.91	2.09	1.0	0.91	2.1	1.0
2	3.37	2.0	3.39	1.99	0.99	3.35	1.99	0.984	3.35	1.98	0.98
3	7.11	2.0	7.10	1.97	1.0	7.10	2.02	0.99	7.12	2.03	0.99
4	10.66	2.0	10.65	1.96	0.99	10.67	2.04	0.99	10.64	2.07	0.99
5	12.73	2.0	12.75	1.97	1.0	12.75	1.96	0.99	12.77	1.96	0.99

4.4.1 Presence of multiple harmonics

So far, the presence of a single harmonic was considered. This is extended further to the case where multiple harmonic excitation sources are present. As an illustration, a total of three harmonics with frequencies 2.0, 5.1 and 8.5 Hz are added the broadband excitation at all the floor levels. The excitation frequencies are chosen in such a way that they are well-separated from the natural frequencies of the structure. Fig. 4.6 shows the Fourier spectra of the response at the 5^{th} and 4^{th} floors. The details of identification are presented

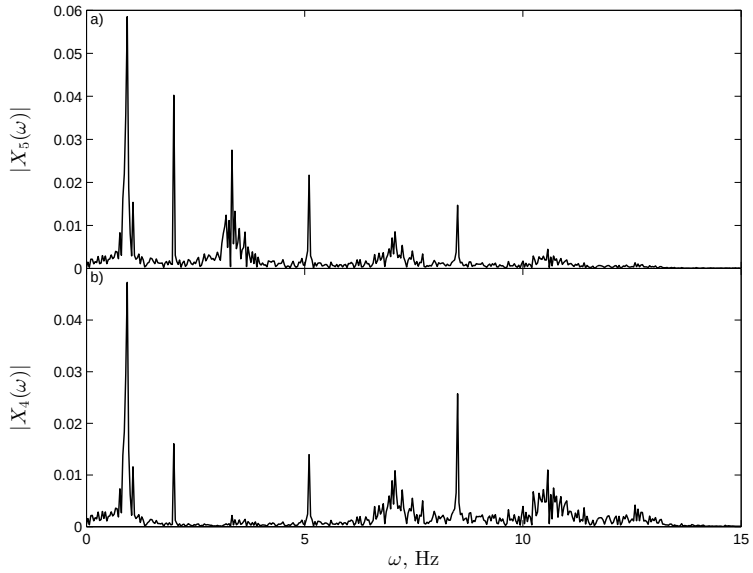

Figure 4.6: Fourier spectrum of the response

in Fig. 4.7. The kurtosis values of the coefficients $f_i^{6,1}$, $f_i^{6,3}$ and $f_i^{6,7}$ are significantly less

than 3.0 and hence discarded as candidates for excitation harmonics, a feature that is also evident from their respective Fourier transforms. The remaining coefficients are primarily the sources corresponding to system harmonics, and are used for the estimation of modal parameters as explained in previous section. Fig. 4.7 shows two typical coefficients $f_i^{6,0}$ and

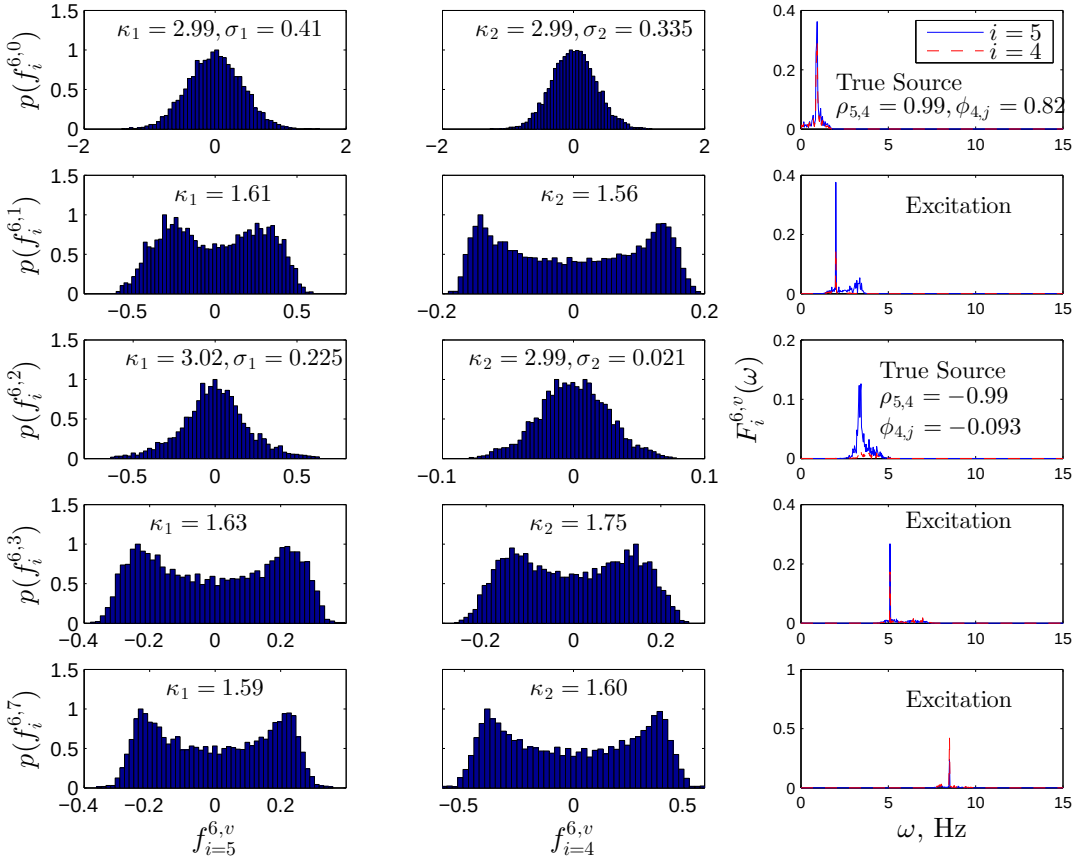

Figure 4.7: Details of identification using the PDF of $f_5^{6,v}$ and $f_4^{6,v}$ under the presence of multiple harmonics

$f_i^{6,2}$ that have kurtosis values of nearly 3.0, in fact they are the modal responses containing the structural frequencies of 0.91 and 3.39 Hz, respectively. The proposed method as described in the earlier section is then employed to estimate the modal parameters. For example, $f_5^{6,2}$ and $f_4^{6,2}$ have a ρ value of -0.99 and standard deviation of 0.225 and 0.021

respectively, for which $\phi_{4,j}$ becomes $\frac{0.021}{0.225} = -0.093$. This example shows that the procedure described in this paper can be extended to the case of multiple disturbance harmonics embedded along with structural modes, provided their frequencies are well separated.

4.5 Summary

A decentralized ambient modal identification method that can satisfactorily delineate the modal sources when narrow band harmonics are present in the excitations, was presented in this chapter. The algorithm is based on the principle of sparse blind source separation using stationary wavelet packet transforms. The main advantage of the proposed approach is in its decentralized architecture, with as few as two sensors at a time used for mode shape construction. In this method, prior information regarding the excitation harmonic frequency is not required, and is estimated along with the modal frequencies. The bootstrap approach allows the estimation of key statistics using limited measurements, which has potential in situations where repeating experiments is cumbersome. Due to the filter bank implementation of wavelet transforms, the proposed method is robust to measurement noise and other extraneous frequencies. Through an example simulation study, it was shown that the method works well when single or multiple harmonics are present, as long as the disturbance frequencies are well separated from the structural modes.

Chapter 5

Parallel Factor Decomposition for Compact Sparse Decentralized BSS

In the previous chapters decentralized BSS algorithms geared towards ambient modal identification with and without the presence of narrow-band harmonics was presented. One of the central aspects of these methods is the use of time-frequency transformations employing SWPT. In many applications, however, the redundant SWPT can be computationally intensive depending on the bandwidth of the signals and the sampling frequency of the vibration measurements. The rather large volume of data to be handled even in such decentralized situations with limited sensors creates significant computational burden. This issue of computational burden is alleviated here, which is based on a tensor algebra tool called PARAllel FACtor (PARAFAC) decomposition [43, 24, 20]. The basic principle behind this approach is that PARAFAC enables source separation in wavelet packet coefficients with considerable mode mixing, thereby relaxing the conditions to generate over-complete mono-component bases, thus reducing the computational burden. The proposed method is validated using a series of numerical simulations.

5.1 Introduction

In the decentralized approach employing SWPT, an appropriate choice of the scale level is critical. This depends on the sampling frequency and the lowest modal frequency of underlying system. As many civil structures exhibit low frequencies (many less than 1 Hz), the number of decomposition levels required to achieve mono-component sources is large. In such cases, if the required scale level can be reduced, this could mean a substantial savings in the computation burden, especially for very low frequency systems. Stated differently, the challenge is to delineate all the frequencies at a higher scale level (instead of the last scale level). This is attempted using a tensor algebra tool called PARAllel FACtor (PARAFAC) [70, 71] as explained next.

The PARAFAC decomposition of a higher-order tensor is an extremely powerful tensor algebra tool that has achieved significant popularity in multiple disciplines [124]. When a signal is a multi-dimensional array, its tensor representation allows us to use multi-linear algebra tools. The basic working of PARAFAC is as follows. A general tensor is first decomposed into a sum of rank-1 tensors. A rank-1 tensor is commonly defined as outer products of triple vectors and it is termed as a PARAFAC component [43, 24, 20]. Therefore, PARAFAC decomposition of a tensor of R rank results in R such PARAFAC components, that are to be estimated. Several forms of PARAFAC decomposition enriched with strong uniqueness properties exist in the literature [68, 129, 138, 71]. Recognizing that the two-dimensional covariance matrices of vibration measurements at several lags can be formulated as a third-order tensor, PARAFAC has the potential for separating sources, which are the vibration modes of a flexible structure.

The main advantage of using PARAFAC is that establishing a single framework is possible in order to tackle modal identification problems involving both the over-determined and the under-determined source separation cases. Whereas standard SOBI techniques require the presence of full sensor measurements, a PARAFAC-based sparse BSS (PSBSS)

method, as we will see later, is able to relax this requirement due its strong uniqueness condition. In an unified framework with BSS, PARAFAC can be interpreted as a decomposition technique that directly yields freely decaying auto-correlation vectors of the modal responses. This yields a single and unique interpretation for both under-determined and full measurement situations as well as over-determined cases. In a relevant study, PARAFAC was recently used in conjunction with Bayesian model updating method [1] to estimate modal parameters. In contrast, this research work addresses this problem within the context of decentralized implementation, which, in addition to noise robustness, separability of closely-spaced modes and low-energy modes, was not studied in the aforementioned work. The source separation capability of PARAFAC is further enhanced by the use of stationary wavelet packet transform . The PARAFAC components explicitly yield the mode shapes, and the auto-correlation functions of the resulting modal responses yield the corresponding frequencies and damping.

5.2 Background

The methodology presented here needs a brief background on PARAFAC. In this section, a brief background of PARAFAC decomposition is discussed, before going into the details of the algorithm.

5.2.1 PARAFAC Decomposition

When a signal is expressed as a multi-dimensional array, then its tensor representation allows the use of multi-linear algebra tools, which is more powerful than linear algebra tools [124]. A vector $\mathbf{t} = t_i \in \Re^{n_1}$ is a first-order tensor, whereas a matrix $\mathbf{T} = t_{ij} \in \Re^{n_1 \times n_2}$

is second-order tensor. In general a p^{th} order tensor is written as:

$$\underline{\mathbf{T}} = t_{ijk...p} \in \Re^{n_1 \times n_2 \times n_3 \times .... \times n_p} \tag{5.1}$$

The simplest three-dimensional tensor is a $2 \times 2 \times 2$ tensor which can be visualized as a parallelepiped (as shown in Fig. 5.1(a)). Like matrices, a tensor is defined by its higher

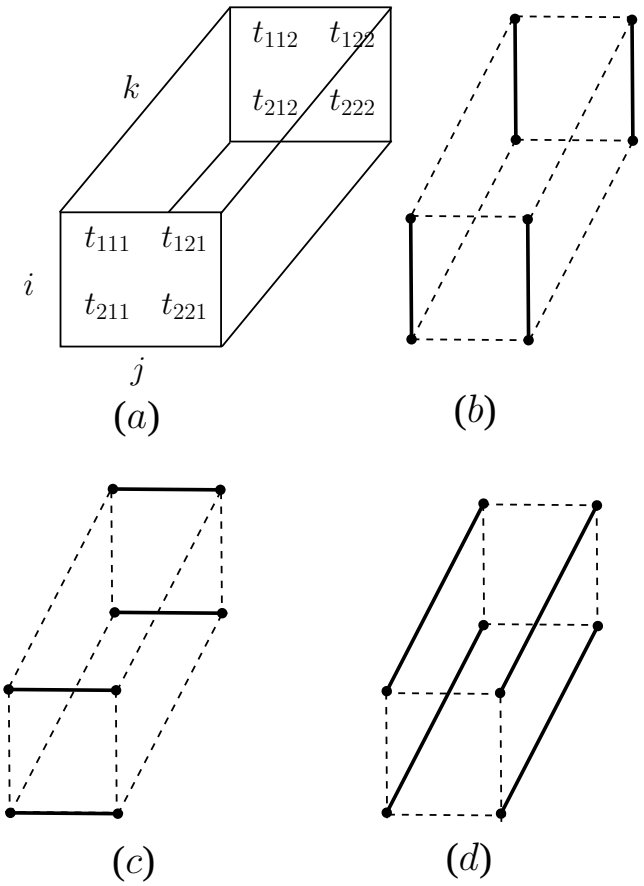

Figure 5.1: (a) Block representation of a $2 \times 2 \times 2$ tensor, t_{ijk}, tensor fibers (b) mode-1 fibers, (c) mode-2 fibers, and (d) mode-3 fibers

order fibres, mode-1 (column) fibres ($t_{:jk}$), mode-2 (row) fibres ($t_{i:k}$) and mode-3 (tube) fibres ($t_{ij:}$) as shown in Fig. 5.1 (b)-(d). They are obtained by fixing any two of the three indices. A tensor is also represented by a matrix by rearranging its elements which

is commonly known as *matricization* or *unfolding* [124]. For a three-dimensional tensor, three types of matricization can be formed by fixing any one of the indices of a tensor, i.e., horizontal ($t_{i::}$), lateral ($t_{:j:}$) and frontal ($t_{::k}$) which form the slices of three respective modes. For example, mode-1 slices comprise of two horizontal slices and it is described as:

$$\underline{\mathbf{T}}_{(1)} = \begin{bmatrix} t_{1::} \\ t_{2::} \end{bmatrix} = \begin{bmatrix} t_{111} & t_{121} & t_{112} & t_{122} \\ t_{211} & t_{221} & t_{212} & t_{222} \end{bmatrix} \tag{5.2}$$

Along the same lines, mode-2 and mode-3 can be expressed as:

$$\underline{\mathbf{T}}_{(2)} = \begin{bmatrix} t_{111} & t_{211} & t_{112} & t_{212} \\ t_{121} & t_{221} & t_{122} & t_{222} \end{bmatrix} \tag{5.3}$$

and

$$\underline{\mathbf{T}}_{(3)} = \begin{bmatrix} t_{111} & t_{121} & t_{211} & t_{221} \\ t_{112} & t_{212} & t_{122} & t_{222} \end{bmatrix} \tag{5.4}$$

respectively. Eqs. 5.2, 5.3 and 5.4 represent mode-1, mode-2 and mode-3 matricizations, respectively. It may be noted that the term *mode* here is associated with the notion of tensor matricization [124] and it should not be confused with the notion of structural modes. While considering the product of tensor and matrix, one has to decide the dimension of the tensor and accordingly, matricization plays an important role [124]. The n-mode product of a tensor with a matrix $\mathbf{A}$ is defined below [124]:

$$\underline{\mathbf{P}} = \underline{\mathbf{T}} \times_n \mathbf{A} \Leftrightarrow \underline{\mathbf{P}}_{(n)} = \mathbf{A}\underline{\mathbf{T}}_{(n)} \tag{5.5}$$

where each n-mode fiber of $\underline{\mathbf{T}}$ is multiplied by the matrix $\mathbf{A}$ to compute n-mode fiber of the resulting tensor $\underline{\mathbf{P}}$.

A three-way tensor is primarily decomposed into a sum of outer products of triple vectors as shown in Fig. 5.2 [124]:

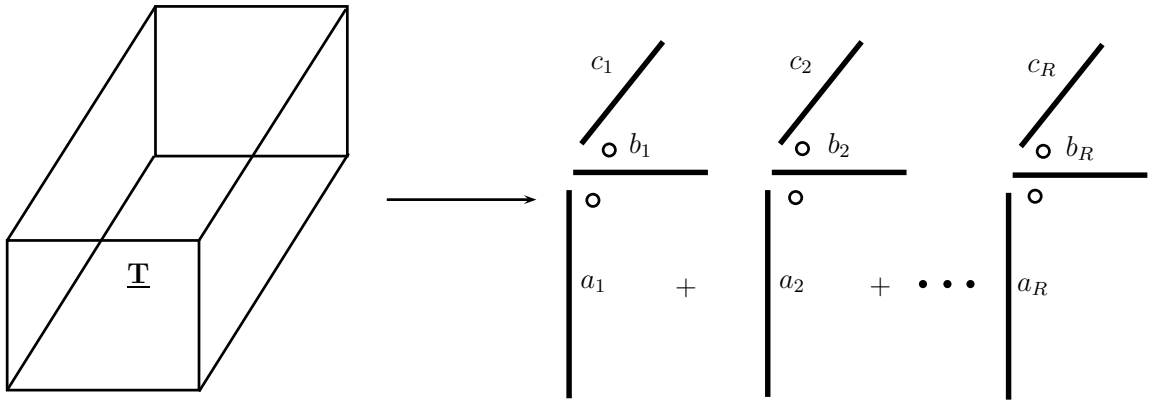

Figure 5.2: Tensor decomposition

$$\underline{\mathbf{T}} = \sum_{r=1}^{R} \mathbf{a_r} \circ \mathbf{b_r} \circ \mathbf{c_r} \Longleftrightarrow \underline{T}_{ijk} = \sum_{r=1}^{R} a_{ir} b_{jr} c_{kr} \tag{5.6}$$

where $\circ$ denotes the outer product and $i \in [1\ \mathrm{I}]$, $j \in [1\ \mathrm{J}]$ and $k \in [1\ \mathrm{K}]$. This is termed as a trilinear model of $\underline{\mathbf{T}}$, $\underline{\mathbf{T}} = [[\mathbf{A}, \mathbf{B}, \mathbf{C}]]$, where the matrices are given by $\mathbf{A} = (\mathbf{a_1}, \mathbf{a_2}, ..., \mathbf{a_R})$, $\mathbf{B} = (\mathbf{b_1}, \mathbf{b_2}, ..., \mathbf{b_R})$, and $\mathbf{C} = (\mathbf{c_1}, \mathbf{c_2}, ..., \mathbf{c_R})$. Therefore, Eq. 5.6 represents the summation of R rank-1 tensors or PARAFAC components that are needed to fit the tensor. PARAFAC components are usually estimated by minimization of the quadratic cost function:

$$g(a, b, c) = \|\underline{\mathbf{T}} - \sum_{r=1}^{R} \mathbf{a_r} \circ \mathbf{b_r} \circ \mathbf{c_r}\|^2 \tag{5.7}$$

This technique was introduced in two different works; canonical decomposition (CANDECOMP) [24] or parallel factor analysis (PARAFAC) [43]. The algorithms fitting the PARAFAC model are usually classified in three main groups [138]: (a) alternating least squares (ALS), which updates only a subset of parameters at each step; (b) derivative-based methods; which seeks an update for all the parameters simultaneously by successive approximations, and (c) direct or non-iterative approaches. Out of these, ALS method has several advantages, including easier implementation, guaranteed convergence, and better handling capability of higher order tensors [138].

Using ALS, the PARAFAC components $\mathbf{A}$, $\mathbf{B}$ and $\mathbf{C}$ are estimated as follows.

$$\begin{aligned}\mathbf{A} &\longleftarrow \underline{\mathbf{T}}_{(1)}(\mathbf{C} \odot \mathbf{B})(\mathbf{C}^T\mathbf{C} * \mathbf{B}^T\mathbf{B})^{\dagger} \\ \mathbf{B} &\longleftarrow \underline{\mathbf{T}}_{(2)}(\mathbf{C} \odot \mathbf{A})(\mathbf{C}^T\mathbf{C} * \mathbf{A}^T\mathbf{A})^{\dagger} \\ \mathbf{C} &\longleftarrow \underline{\mathbf{T}}_{(3)}(\mathbf{B} \odot \mathbf{A})(\mathbf{B}^T\mathbf{B} * \mathbf{A}^T\mathbf{A})^{\dagger} \end{aligned} \tag{5.8}$$

where $\odot$ indicates Khatri-Rao product. ALS is primarily consisting of following key steps which exploits the simultaneous unfolding of three matrices:

- Fix $\mathbf{A}$ and $\mathbf{B}$, solve for $\mathbf{C}$

$$\min_{\mathbf{C}} \|\underline{\mathbf{T}} - [[\mathbf{A}, \mathbf{B}, \mathbf{C}]]\|^2 \equiv \min_{\mathbf{C}} \|\underline{\mathbf{T}}_{(3)} - \mathbf{C}(\mathbf{B} \odot \mathbf{A})^T\|^2 \tag{5.9}$$

- Optimal $\mathbf{C}$ is the least square solution:

$$\mathbf{C} = \underline{\mathbf{T}}_{(3)}(\mathbf{B} \odot \mathbf{A})(\mathbf{B}^T\mathbf{B} * \mathbf{A}^T\mathbf{A})^{\dagger} \tag{5.10}$$

- Successively solve for each component of $\mathbf{A}$, $\mathbf{B}$ and $\mathbf{C}$

First, $\mathbf{A}$ and $\mathbf{B}$ are fixed, and $\mathbf{C}$ is solved using [124]:

$$\min_{\mathbf{C}} \|\underline{\mathbf{T}} - [[\mathbf{A}, \mathbf{B}, \mathbf{C}]]\|^2 \equiv \min_{\mathbf{C}} \|\underline{\mathbf{T}}_{(3)} - \mathbf{C}(\mathbf{B} \odot \mathbf{A})^T\|^2 \tag{5.11}$$

Optimal $\mathbf{C}$ is obtained using the following least-square solution:

$$\mathbf{C} = \underline{\mathbf{T}}_{(3)}(\mathbf{B} \odot \mathbf{A})(\mathbf{B}^T\mathbf{B} * \mathbf{A}^T\mathbf{A})^{\dagger} \tag{5.12}$$

where, $\odot$ indicates Khatri-Rao product. Given $\mathbf{A} \epsilon \Re^{I \times R}$ and $\mathbf{B} \epsilon \Re^{J \times R}$, $\mathbf{A} \odot \mathbf{B}$ is a matrix

with IJ rows and R columns and is expressed as:

$$A \odot B = \begin{bmatrix} a_{11} & a_{12} & \cdots\cdots & a_{1R} \\ a_{21} & a_{22} & \cdots\cdots & a_{2R} \\ \vdots & \vdots & \cdots\cdots & \vdots \\ a_{I1} & a_{I2} & \cdots\cdots & a_{IR} \end{bmatrix} \odot \begin{bmatrix} b_{11} & b_{12} & \cdots\cdots & b_{1R} \\ b_{21} & b_{22} & \cdots\cdots & b_{2R} \\ \vdots & \vdots & \vdots & \vdots \\ b_{J1} & b_{J2} & \cdots\cdots & b_{JR} \end{bmatrix} \tag{5.13}$$

which is simplified as:

$$A \odot B = \begin{bmatrix} a_{11}b_{:1} & a_{12}b_{:2} & \cdots\cdots & a_{1R}b_{:R} \\ a_{21}b_{:1} & a_{22}b_{:2} & \cdots\cdots & a_{2R}b_{:R} \\ \vdots & \vdots & \vdots & \vdots \\ a_{I1}b_{:1} & a_{I2}b_{:2} & \cdots\cdots & a_{IR}b_{:R} \end{bmatrix} \tag{5.14}$$

where $b_{:k}$ represents k^{th} column of $\mathbf{B}$. Once $\mathbf{C}$ is estimated using Eq. 5.12, $\mathbf{A}$ and $\mathbf{B}$ are solved successively using the following steps:

$$\begin{aligned} \mathbf{A} &\longleftarrow \underline{\mathbf{T}}_{(1)}(\mathbf{C} \odot \mathbf{B})(\mathbf{C}^T\mathbf{C} * \mathbf{B}^T\mathbf{B})^\dagger \\ \mathbf{B} &\longleftarrow \underline{\mathbf{T}}_{(2)}(\mathbf{C} \odot \mathbf{A})(\mathbf{C}^T\mathbf{C} * \mathbf{A}^T\mathbf{A})^\dagger \end{aligned} \tag{5.15}$$

Finally the algorithm finds a tensor $\hat{\underline{\mathbf{T}}} = \sum_{r=1}^{R} \mathbf{a_r} \circ \mathbf{b_r} \circ \mathbf{c_r}$ such that Eq. 5.7 is satisfied. An unique decomposition is obtained if the following Kruskal condition [68] is satisfied:

$$k_A + k_B + k_C \geq 2R + 2 \tag{5.16}$$

where k_A, k_B and k_C are the $k-$rank of the matrices $\mathbf{A}$, $\mathbf{B}$ and $\mathbf{C}$ respectively (k-rank is defined as maximum number k such that every set of k columns of the matrix is linearly independent [68]).

5.3 Formulation

5.3.1 PARAFAC-only method (PBSS)

When all the measurements of Eq. 3.3 are available (i.e, $n_m \geq n_s$), the covariance matrix $\mathbf{R_x}(k)$ evaluated at time-lag k can be written as:

$$\mathbf{R_x}(k) = E\left\{\mathbf{x}(n)\mathbf{x}^T(n-k)\right\} = \mathbf{A}\mathbf{R_s}(k)\mathbf{A}^T \tag{5.17}$$

$$\mathbf{R_s}(k) = E\left\{\mathbf{s}(n)\mathbf{s}^T(n-k)\right\} \tag{5.18}$$

For notational simplicity, the following definitions are used:

$$\begin{aligned} R_{x_1x_2}(k) = R^x_{12k} &\Longleftrightarrow R_{x_ix_j}(k) = R^x_{ijk} \\ R_{s_1}(k) = R^s_{k1} &\Longleftrightarrow R_{s_l}(k) = R^s_{kl} \end{aligned} \tag{5.19}$$

Eq. 5.17 can be expanded for $\mathbf{x} = \{x_1, x_2, x_3\}$ as follows:

$$\begin{bmatrix} R^x_{11k} & R^x_{12k} & R^x_{13k} \\ R^x_{21k} & R^x_{22k} & R^x_{23k} \\ R^x_{31k} & R^x_{32k} & R^x_{33k} \end{bmatrix} = \begin{bmatrix} a_{11} & a_{12} & a_{13} \\ a_{21} & a_{22} & a_{23} \\ a_{31} & a_{32} & a_{33} \end{bmatrix} \begin{bmatrix} R^s_{k1} & 0 & 0 \\ 0 & R^s_{k2} & 0 \\ 0 & 0 & R^s_{k3} \end{bmatrix} \begin{bmatrix} a_{11} & a_{21} & a_{31} \\ a_{12} & a_{22} & a_{32} \\ a_{13} & a_{23} & a_{33} \end{bmatrix} \tag{5.20}$$

From Eq. 5.20, using the simplified notations as in Eq. 5.19, $R_{x_1x_2}(k) = R^x_{12k}$ can be expressed as:

$$R^x_{12k} = a_{11}a_{21}R^s_{k1} + a_{12}a_{22}R^s_{k2} + a_{13}a_{23}R^s_{k3} \tag{5.21}$$

which can be generalized for R^x_{ijk} as:

$$R^x_{ijk} = a_{i1}a_{j1}R^s_{k1} + a_{i2}a_{j2}R^s_{k2} + a_{i3}a_{j3}R^s_{k3} = \sum_{r=1}^{3} a_{ir}a_{jr}R^s_{kr} \quad i,j = 1-3; k = 1,2,3,...,p_k \tag{5.22}$$

where p_k is the total number of lags considered for the PARAFAC decomposition. For a general n_s-DOF system, Eq. 5.22 can be generalized as:

$$R^x_{ijk} = \sum_{r=1}^{n_s} a_{ir} a_{jr} R^s_{kr} \Longleftrightarrow \mathbf{R^x} = \sum_{r=1}^{n_s} \mathbf{a_r} \circ \mathbf{a_r} \circ \mathbf{R^s_r} \tag{5.23}$$

Now, we can observe that Eqs. 5.6 and 5.23 are similar; hence, the mixing matrix can be estimated by decomposing the third order tensor $\mathbf{R^x}$ into n_s number of rank-1 tensors (i.e., PARAFAC components). Using PARAFAC decomposition explained previously, the resulting solutions yield the mixing matrix $\mathbf{A} = [\mathbf{a_1}, \mathbf{a_2}, \mathbf{a_3}, ...\mathbf{a_{n_s}}]$ and the auto-correlation functions of $\mathbf{R^s_r}$ for $r = 1, 2, 3, ...n_s$, from which the natural frequency and damping corresponding to each mode can be estimated.

In order to demonstrate the source separation using PARAFAC decomposition, a linear mixture of two sine waves with frequencies 1.0 and 2.5 hz are considered.

$$\begin{aligned} x_1 &= s_1 + s_2 \\ x_2 &= 1.5s_1 + 4.5s_2 \end{aligned} \tag{5.24}$$

Since the mixture contains two sources, rank-2 PARAFAC decomposition is employed to extract the hidden harmonics from the mixtures. Fig. 5.3 shows the true harmonics, their mixtures, and estimated sources $\hat{s}$. PARAFAC decomposition yields $\mathbf{a_1}$ and $\mathbf{a_2}$ as shown in Fig. 5.3, from which the mixing matrix can be estimated by concatenating successively normalized (say w.r.t x_1) $\mathbf{a}$'s:

$$A = \begin{bmatrix} a_1 & a_2 \end{bmatrix} = \begin{bmatrix} 1.404 & 1.027 \\ 2.11 & 4.622 \end{bmatrix} \Leftrightarrow \begin{bmatrix} 1 & 1 \\ 1.5 & 4.5 \end{bmatrix} \tag{5.25}$$

As compared to a two-way array (matrix case), PARAFAC yields a unique decomposition even if the rank is greater than the smallest dimension of tensor, i.e., $n_m < n_s$

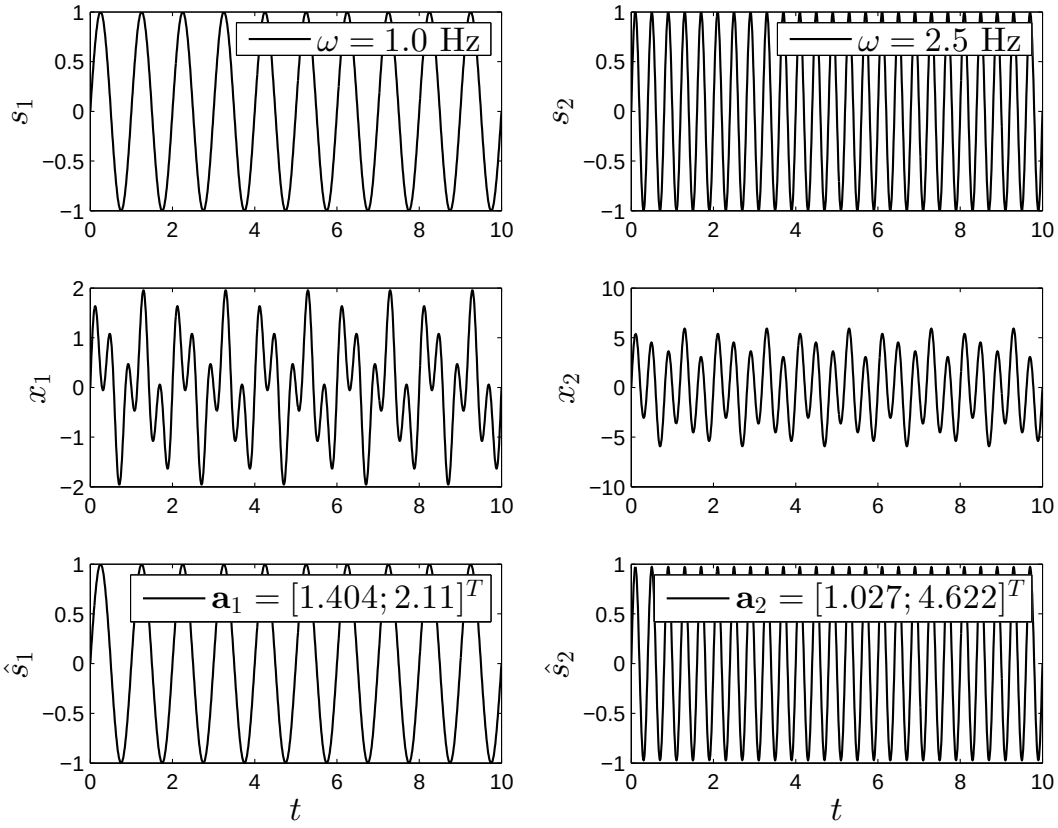

Figure 5.3: Typical source separation using PARAFAC

[71]. When $B = A$ (comparing Eq. 5.6 and 5.23), a more relaxed uniqueness condition is proposed [129] where the following inequality is satisfied:

$$\frac{n_s(n_s-1)}{2} = \frac{n_m(n_m-1)}{4}[\frac{n_m(n_m-1)}{2}+1] - \frac{n_m!}{(n_m-4)!4!}(n_m)_{\{n_m \geq 4\}} \tag{5.26}$$

where,

$$\begin{aligned}(n_m)_{\{n_m \geq 4\}} &= 0 \quad n_m < 4 \\ (n_m)_{\{n_m \geq 4\}} &= 1 \quad n_m \geq 4\end{aligned} \tag{5.27}$$

Using Eq. 5.26, an upper bound of source separability of PARAFAC decomposition can

be computed, which is shown in Table 5.1 [129].

Table 5.1: Source separation capability of PARAFAC

n_m	2	3	4	5	6	7	8	9	10
n_s	2	4	6	10	15	20	26	33	41

An important factor that determines the source separation capability of PARAFAC is the relative energy content of various modes amongst measurement channels [1]. For example, in typical ambient vibration measurement cases, all the sources (i.e., modal responses) might not have significant energy content that will allow easy delineation using traditional BSS methods. In such cases, the direct application of PARAFAC (PBSS) method [113] to noisy data with multiple low-energy modes is not likely to yield satisfactory results. This issue is overcome using the noise robustness and separability properties of wavelet transforms within the framework of sparse BSS.

5.3.2 PARAFAC-based Sparse BSS (PSBSS)

So far the discussion has been limited to cases where full measurements ($n_m > n_s$) are available. When $n_m \ll n_s$, a PARAFAC decomposition based sparse BSS (PSBSS) method can be implemented [114], which is a computational improvement of sparse BSS method [115] described in the previous section.

Eq. 4.13, as discussed earlier, requires the application of wavelet packet decomposition until the last scale level ($j = s$). A suitable choice of s however depends on – (a) sampling frequency (f_s) and (b) lowest modal frequency of structures (f_l). f_s values for civil engineering structures commonly range from 100-500 Hz. Under such circumstances, using dyadic decomposition of wavelets, the required scale level ($2^s = \frac{f_s}{f_l}$) becomes large (since s is proportional to f_s), which results in a large volume of wavelet packet coefficients that need to be extracted and managed. Similar scenario occurs when some of the structural

frequencies are not well-separated (which commonly occur in flexible light-weight structures, or in structures with tuned-mass-dampers), thereby requiring a relatively high scale level for accurate source separation with fine resolution.

An obvious way to overcome this large computational burden is to limit the scale level to a smaller number ($j < s$); however, this will result in significant mode-mixing amongst structural frequencies. In order to overcome this issue, while limiting the scale level, the strong identifiability property of PARAFAC is utilized as follows.

Consider the mode-mixing of n_m^u ($n_m \leq n_m^u < n_s$) sources in the SPWT coefficients at a scale level u (where, $j = u << s$). Eq. 4.12 in matrix vector form can be written as:

$$\mathbf{f}_\alpha^{u,v} = \mathbf{A_u} \mathbf{e}_\alpha^{u,v} \tag{5.28}$$

Therefore, by utilizing the shift-invariance property of SWPT, the covariance matrix of SWPT coefficients of the partial measurements $f_\alpha^{u,v}$ (i.e., $\mathbf{R}_{\mathbf{f}_\alpha^{\mathbf{u,v}}}(l_k)$) evaluated at time lag (l_k) can be written as:

$$\mathbf{R}_{\mathbf{f}_\alpha^{\mathbf{u,v}}}(l_k) = \mathbf{A_u} \mathbf{R}_{\mathbf{e}_\alpha^{\mathbf{u,v}}}(l_k) \mathbf{A_u}^T \tag{5.29}$$

Now, following a similar procedure in Eq. 5.17–5.23, this can be further simplified to the following PARAFAC model of SWPT coefficients:

$$\mathbf{R^f} = \sum_{r=1}^{n_m^u} \mathbf{a_r^u} \circ \mathbf{a_r^u} \circ \mathbf{R_r^e} \tag{5.30}$$

By comparing Eq. 5.30 and 5.23, we see that the third order tensor $\mathbf{R^f}$ can be decomposed into n_m^u number of rank-1 tensors using PARAFAC. However, unlike the former case (i.e., Eq. 5.23) where n_s sources (i.e., $\mathbf{A}_{n_m \times n_s}$) are identified in a single step, in the latter case (i.e., Eq. 5.30) only a subset of the partial mixing matrix (i.e., $\mathbf{A}_{n_m \times n_m^u}$) with n_m^u sources is

estimated from n_m SPWT coefficients at a given v. By using PARAFAC decomposition, the resulting solutions yield a subset of the partial mixing matrix $\mathbf{A} = [\mathbf{a_1^u}, \mathbf{a_2^u}, \mathbf{a_3^u}, ...\mathbf{a_{n_m^u}^u}]_{n_m \times n_m^u}$ and the auto-correlation functions of $\mathbf{R_r^e}$ for $r = 1, 2, 3, ...n_m^u$, from which the natural frequency and damping of the respective mode can be estimated. By repeating this process for other SPWT coefficients (i.e., for $v = 0, 2, ..., (2^u - 1)$), the complete partial mixing matrix (i.e., $\mathbf{A}_{n_m \times n_s}$) of n_s modes can be constructed and the natural frequency and damping for n_s modes can be estimated. It is important to to note that the source separation capability of PARAFAC as guided by Table 5.1 is significantly improved when incorporated into the framework of sparse BSS. In PBSS method, the uniqueness property of PARAFAC applies throughout the full measurement setups. On the other hand, this property in the PSBSS method is utilized only at the individual packet level. Therefore, the PSBSS method is able to separate all the structural modes and the associated partial mixing matrix using a limited number of sensors. In this way, the source separation capability of PARAFAC is significantly improved and made applicable to under-determined situations.

So far, using the proposed method, a partial mixing matrix (i.e., $\mathbf{A}_{n_m \times n_s}$) is obtained. By repeating this exercise for successive setups as explained in section 2.1.3, the full mixing matrix (i.e., $\mathbf{A}_{n_s \times n_s}$) can be obtained. The key steps involved in the algorithm (for two measurement channels at a time) are listed below for estimating the natural frequencies, damping, and the partial mode-shape matrix.

- Obtain the partial measurements x_q and x_r.
- Perform SWPT for the measurements up to scale level u which yields $f_{k,q}^{u,v}$ and $f_{k,r}^{u,v}$ for $v = 0, 1, 2, ..., (2^u - 1)$.
- Apply PARAFAC decomposition to the set of SWPT coefficients at each v to obtain a subset of partial mode-shape $\bar{\Phi}_{n_m \times n_m^u}$ and the associated natural frequencies and damping ratios.

- Repeat the previous step for $v = 0, 1, 2, ..., (2^u - 1)$ and estimate the complete partial mixing matrix (i.e., $\bar{\Phi}_{n_m \times n_s}$).

- Eq. 3.33 is then used to estimate the complete mode-shape matrix coefficients (i.e., $\Phi_{n_s \times n_s}$) by utilizing various measurement setups.

From the point of view of decentralized implementation, SWPT and thresholding can be performed at an individual node (e.g., a wireless smart sensor node), and the remaining steps can be completed at an intermediate stage, or centrally. Assuming each point is 2 byte short, the number of operations for SWPT at an individual node in its naive form is $\sum_{j=1}^{u} 2^j \times 2 \times N^2$, where u is the scale level ($u < s$), and N is the sample length. For example, at level $s = 4$ decomposition with sample length of 5 sec at 100 Hz ($N = 500$), there are 15 $\times 10^6$ individual addition and multiplicative operations in the SWPT-PCA method. On other hand, using PSBSS method, using $u = 2$ ($< s = 4$), the total number of operations would be 3 $\times 10^6$ which yields 80% reduction in the computational effort. The memory requirement is governed by $\sum_{j=1}^{u} 2^j \times 2 \times N$. In the case of the above example (i.e., $u = s = 4$ and $N = 500$), the memory requirement at each node will be 30 kB for the SWPT-PCA method, whereas for the PSBSS method (i.e., $u = 2$) this is reduced to 6 kB. In terms of data transfer between nodes, only a fraction (m out of 2^u as governed by thresholding) of the wavelet coefficients are transmitted, therefore the total communication load between two nodes is $m \times N \times 2 \times n_m$. In this example, when $m = 2 (< 2^u)$, $N = 500$, and $n_m = 2$, the amount of data transmitted is 4 kB.

5.4 Numerical Study

In this section, the methodology and the benefits of the proposed algorithm are demonstrated using a simulation example. The direct application of PARAFAC decomposition

(i.e., PBSS method) is introduced to show how PARAFAC can be used for modal identification of civil structures. The PSBSS method is then verified using a the same example used previously (5DOF) and the relative advantages over the PBSS method and SWPT-PCA method [115] are discussed. In vibration signal processing, a suitable choice of scale level in SWPT depends on the separation of frequencies; therefore the previous example is subsequently equipped with a tuned-mass damper to show the advantage of the PSBSS method to perform identification in the presence of closely-spaced modes. Finally, a 10-DOF building model is used to demonstrate the sensitivity of the PSBSS method to various sensor configurations, which is identified as one of the major bottlenecks of PBSS method.

5.4.1 Application of PBSS method for the 5-DOF building

Simulations are first performed on a 5-storey shear-beam structure model [115]. White Gaussian noise is used to excite the building at all its floor locations. PARAFAC decomposition is performed for the 5 components using five floor measurements. The resulting mixing matrix shows an average MAC number of 0.99 and the auto-correlation of the sources are obtained as shown in Fig. 5.4, from which the natural frequencies and damping are estimated. The sources are estimated by multiplying the pseudo-inverse of mixing matrix with the responses, and are shown in Fig. 5.5.

According to Table 5.1, a minimum 4 sensors are required to identify 5 sources. The mode-shape identification results for full measurement as well as the partial measurement cases are shown in Table 5.2. Results are compared for different noise levels, SNR of 100 and 10. It is observed that the MAC numbers decrease for the second and the fifth modes for the higher noise level case, due to the low energy in the respective modes present in the floor response measurements. Thus, it can be observed that the PBSS method suffers from performance issues in the presence of low energy modes and measurement

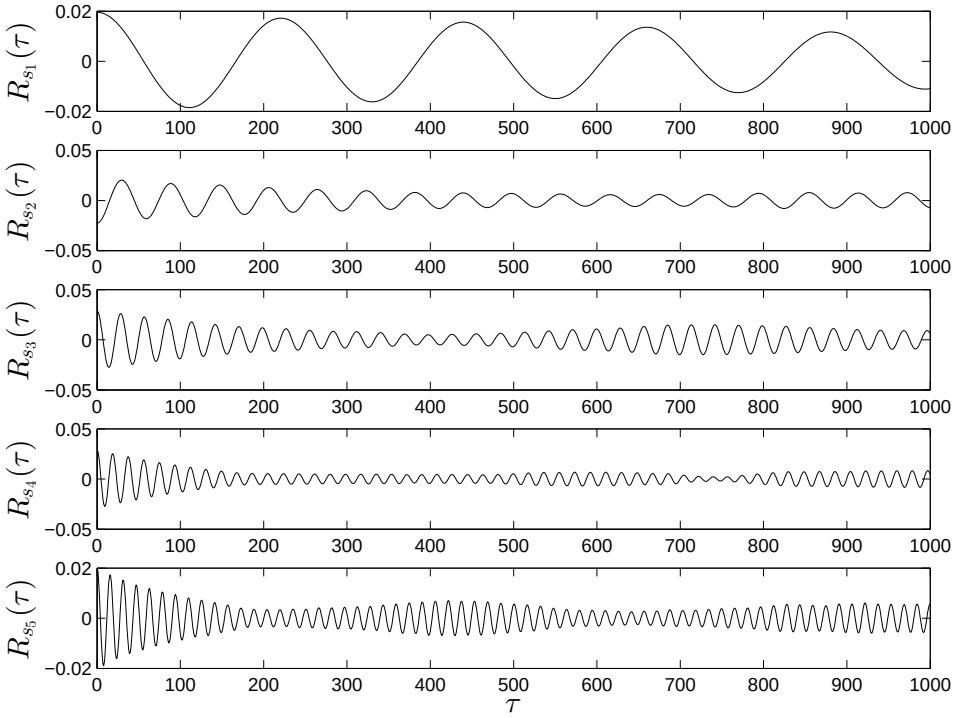

Figure 5.4: 5-DOF building: $\mathbf{R}_{\mathbf{r}}^{\mathbf{s}}$ using PARAFAC-only method

noise, especially for the partial measurement case. Additionally, an upper bound on the number of sources that can be identified for the partial measurement case is limited by the uniqueness or identifiability property enumerated in Table 5.1, which is a serious limitation of the PARAFAC approach. These shortcomings are addressed using the proposed method as demonstrated in the subsequent sections.

Table 5.2: Details of the identification results of 5-DOF building using PBSS method

	MAC_i (SNR=100)		MAC_i (SNR=10)	
Mode (i)	$n_m = 5$	$n_m = 4$	$n_m = 5$	$n_m = 4$
1	1.0	0.99	0.98	0.97
2	0.99	0.98	0.97	0.93
3	1.0	0.99	0.98	0.97
4	1.0	0.98	0.99	0.98
5	0.99	0.97	0.97	0.92

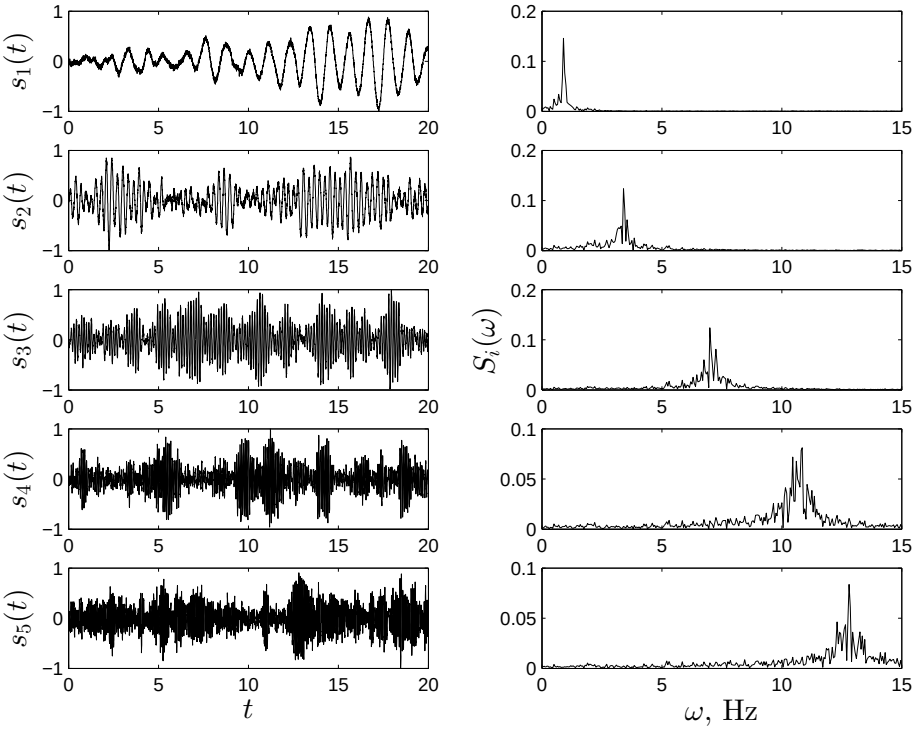

Figure 5.5: 5-DOF building: Estimated source and their Fourier Transform using PARAFAC-only method

5.4.2 Application of the PSBSS method for the 5-DOF building

In the previous example, all the five (or four) floor measurements are utilized for performing source separation. In this example, we apply the new algorithm to estimate the modal parameters using just 2 measurements. Two response measurements at the 5^{th} and 4^{th} floors are processed using SWPT. The maximum scale level (i.e., s) is computed based on the sampling frequency (f_s) of 100 Hz and the lowest frequency (f_l) of the signal (i.e., 0.91 Hz), and this leads to $s = 6$ ($f = \frac{100}{2^6} = 1.56$ Hz> 0.91 Hz). However, to demonstrate the effectiveness of this approach at a lower scale level, we start with a scale level of 5 (i.e., $u = 5$) instead of $s = 6$, which later on will be reduced even further to $s = 3$. Due to its orthogonality property, $db5$ is chosen for the analysis. The coefficients at the last scale level ($2^u = 32$) of decomposition are used to estimate the partial mixing matrix. Of these,

the coefficients containing low-energy noisy components are discarded using a thresholding criterion based on their energy values [115].

Fig. 5.6 shows that there is mode mixing in $f_i^{5,1}$ (i.e., frequencies 0.91 and 3.37 Hz are present at this scale). Rank-2 ($R = 2$) PARAFAC decomposition is then employed for these pairs of SWPT coefficients. The resulting auto-correlation functions of the two PARAFAC components are also shown in Fig. 5.6, from which the natural frequencies and damping ratios are estimated. Similar exercise is repeated for all selected v and the partial mode-shape matrix is formed. Repeating these steps for other measurement set-ups yields the complete mode-shape matrix, according to Eq. 3.33 [115].

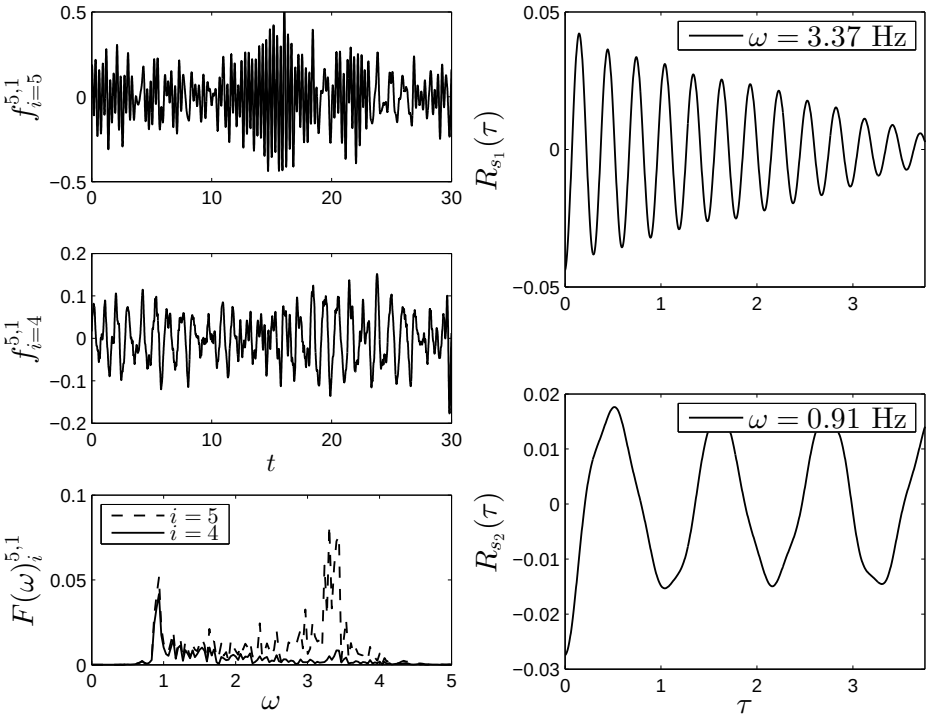

Figure 5.6: 5-DOF Model: (left column) Mode mixing in SWPT coefficients at the lower scale level ($u = 5$), (right column) $R_s(\tau)$ of the PARAFAC components of the SWPT coefficients using the PSBSS method

Typical modal identification results for the 5-DOF building model using PSBSS method comparing SWPT-PCA method are shown in Table 5.3, where $\overline{\text{MAC}}$ denotes the average

MAC value for all the modes. It is noted that when the scale level is less than the required scale level (i.e., $j < s = 6$), mixing occurs for the structural modes, which is difficult to delineate using PCA-based SWPT method [115]. Thus the results are poor ($\overline{\text{MAC}} < 0.92$). On the other hand, with the strong identifiability property of PARAFAC, we are able to separate the sources from their mixtures. From Table 5.3, using a lower scale level (i.e., $u = 5$) that generates only $n_c = 32$ SPWT coefficients compared to 64 coefficients generated by the SWPT-PCA method, similar performance can be achieved with $\overline{\text{MAC}} > 0.99$. It is also evident that n_c (i.e., the number of SWPT coefficients at the u scale level) can be further reduced to only 8 when n_m is increased to 3, by utilizing the identifiability criteria of PARAFAC given in Table 5.1. In this way, the proposed method reduces the level of computational effort significantly, which is especially advantageous in decentralized modal identification situations. On the other hand, a minimum of four measurements are needed to identify the modal parameters for the 5-DOF model with 5 sources using the PARAFAC-only method (as governed by Table 5.1). Therefore, it can be concluded that the source separation capability of PARAFAC is significantly improved when adopted within the framework of sparse BSS. Details of the estimated frequencies and modal damping ratios are shown in Table 5.6.

Table 5.3: 5-DOF building: Performance of the PSBSS method

Case	n_m	u	n_c	Comments	Source Separation
SWPT-PCA method	2	6	64	Imperfect filtering	Success ($\overline{\text{MAC}} > 0.99$)
SWPT-PCA method	2	5	32	Mode mixing of 2 sources	Failure ($\overline{\text{MAC}} < 0.92$)
PSBSS method	2	5	32	Mode mixing of 2 sources	Success ($\overline{\text{MAC}} > 0.99$)
PSBSS method	3	3	8	Mode mixing of 4 sources	Success ($\overline{\text{MAC}} > 0.99$)

5.4.3 Application of the PSBSS method for a building equipped with a tuned-mass-damper

Presence of closely-spaced modes and low energy modes are common in civil structures. For example, such a situation occurs when there is a tuned mass damper (TMD), in near-symmetric structures where there is very little separation in the lateral modes, or when the vibration measurements of a high-rise building are contaminated with measurement noise (higher modes typically carry very low energy relative to the main structural modes). In such cases, SWPT-PCA method [115] requires a relatively high scale level to delineate closely-spaced modes. In order to show the application of the proposed method for the separation of closely-spaced modes using a lower scale level, an optimally designed TMD is assumed at the roof of the 5-DOF model considered earlier. The weight of the TMD is 2.74 kN, $k = 77.8$ N/cm, and $c = 3.72$ Ns/cm [46]. Due to the insertion of the TMD, the first mode (i.e., 0.91 Hz) of the 5-DOF building is segregated into two closely-spaced modes at frequencies 0.78 and 0.99 Hz.

For this example, based on the assumed sampling frequency (i.e., 100 Hz) and the lowest frequency of the structure (i.e., 0.78 Hz), the required scale level for the SWPT-PCA method is 7 (i.e., $s = 7$). However the proposed method can be applied at a scale level of say, 6 (i.e., $u = 6$), which results in a reduction of the number of SWPT coefficients to 64 from 128. Fig. 5.7 shows the Fourier transform of the resulting SPWT coefficient pairs, $f_4^{6,1}$ and $f_5^{6,1}$. It can be seen that there is a significant amount of mode mixing due to the presence of closely spaced modes resulting from this lower scale level selected. However, when the PARAFAC decomposition of the resulting SPWT coefficients is performed, it clearly separates the associated modes as shown in Fig. 5.7. The sub-set of partial mode-shape matrix ($n_m = 2$ and $n_m^u = 2$) can be estimated using the PARAFAC components as given by $\mathbf{A_u}$ in Fig. 5.7:

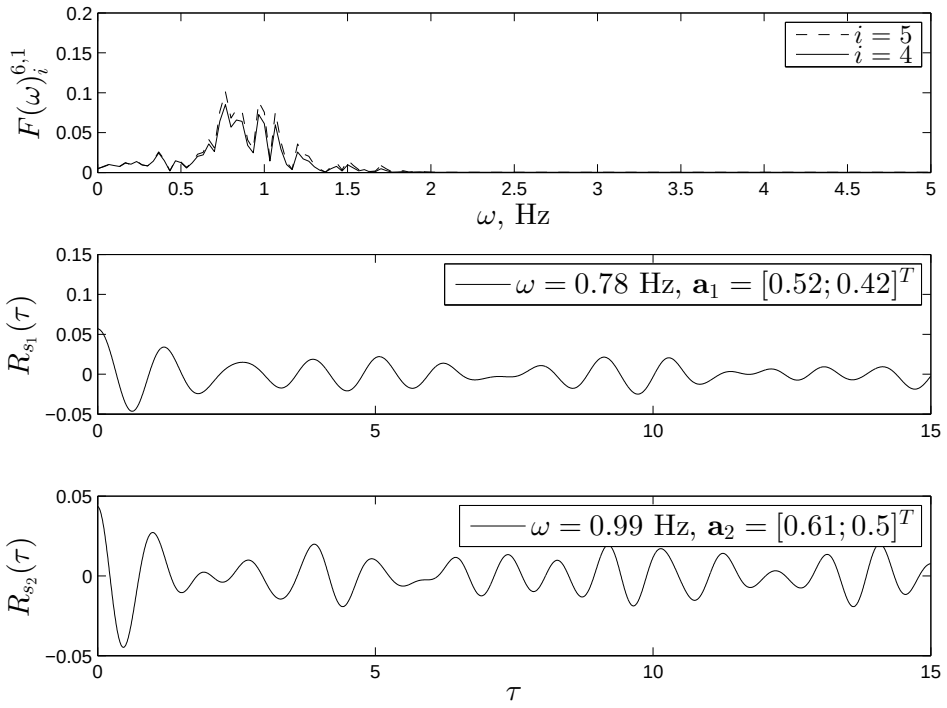

Figure 5.7: 5-DOF with TMD: Source separation of SPWT coefficients of two responses using Rank-2 PARAFAC decomposition

$$A_u = \begin{bmatrix} 0.52 & 0.61 \\ 0.42 & 0.5 \end{bmatrix} \Leftrightarrow \bar{\Phi}_{2\times 2} = \begin{bmatrix} 1.0 & 1.0 \\ 0.8 & 0.82 \end{bmatrix} \tag{5.31}$$

where $\bar{\Phi}$ is a sub-set of the partial mixing matrix (normalized) $\Phi_{2\times 5}$ corresponding to the 5^{th} and 4^{th} floor DOF, associated with the 1^{st} and 2^{nd} modes. Subsequently, the complete partial mixing matrix ($\Phi_{2\times 5}$) is obtained by analyzing the key SWPT coefficient pairs at $v = 0, 1, 2, ..., 63$ with significant energy contents. The complete mixing matrix is then obtained by concatenating $\Phi_{2\times 5}$ different measurement set-ups with a common reference DOF [115].

Increasing the number of measurements, using Table 5.1, the scale level can be reduced further to 4. However, this results in mode-mixing from 3 sources. Fig. 5.8 shows the Fourier transform of the resulting SPWT coefficient pairs, $f_3^{4,1}$, $f_4^{4,1}$ and $f_5^{4,1}$, which shows

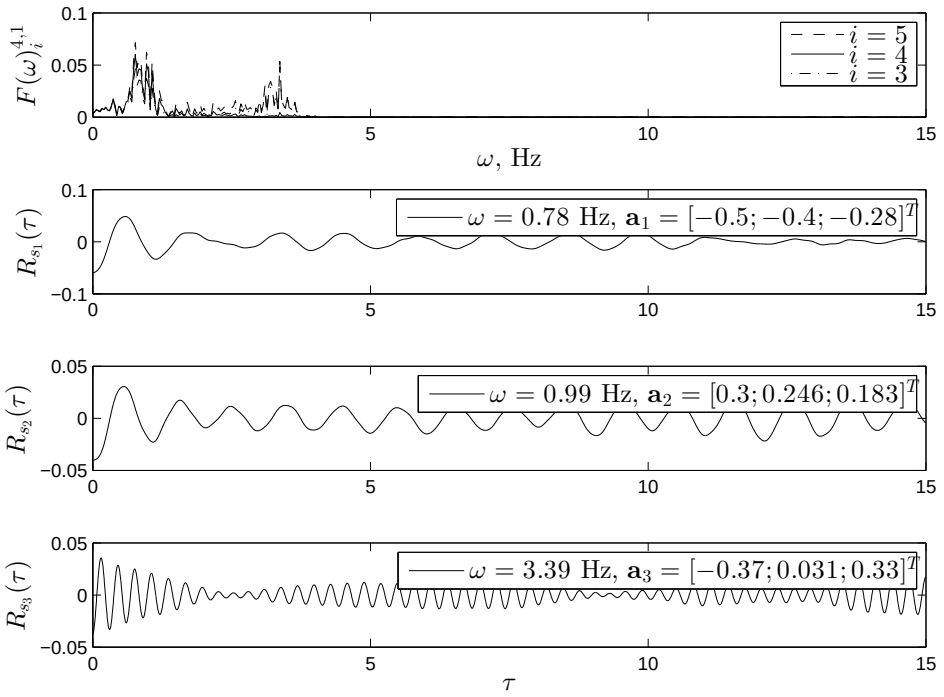

Figure 5.8: 5-DOF with TMD: Source separation of SPWT coefficients of three responses using Rank-3 PARAFAC decomposition

that there is significant amount of mode mixing from 3 sources; however, the sources are separated accurately using Rank-3 PARAFAC decomposition and the sub-set ($\bar{\Phi}_{3\times3}$) of partial mixing matrix ($\bar{\Phi}_{3\times6}$) is obtained as follows:

$$A_u = \begin{bmatrix} -0.5 & 0.3 & -0.37 \\ -0.4 & 0.246 & 0.031 \\ -0.28 & 0.183 & 0.33 \end{bmatrix} \Leftrightarrow \bar{\Phi}_{3\times3} = \begin{bmatrix} 1 & 1 & 1 \\ 0.8 & 0.82 & -0.0823 \\ 0.56 & 0.61 & -0.9 \end{bmatrix} \tag{5.32}$$

Similar results are shown in Fig. 5.9, where the SPWT coefficients (i.e., $f_3^{4,2}$, $f_4^{4,2}$ and $f_5^{4,2}$) at $v = 2$ contain a mixture of two structural modes and a noise component of 4.65 Hz. Such noise components are easily eliminated based on their energy magnitude compared to the physical structural modes. By concatenating the PARAFAC components of successive SWPT coefficient pairs, the partial mixing matrix ($\bar{\Phi}_{3\times6}$) can be constructed. It may be

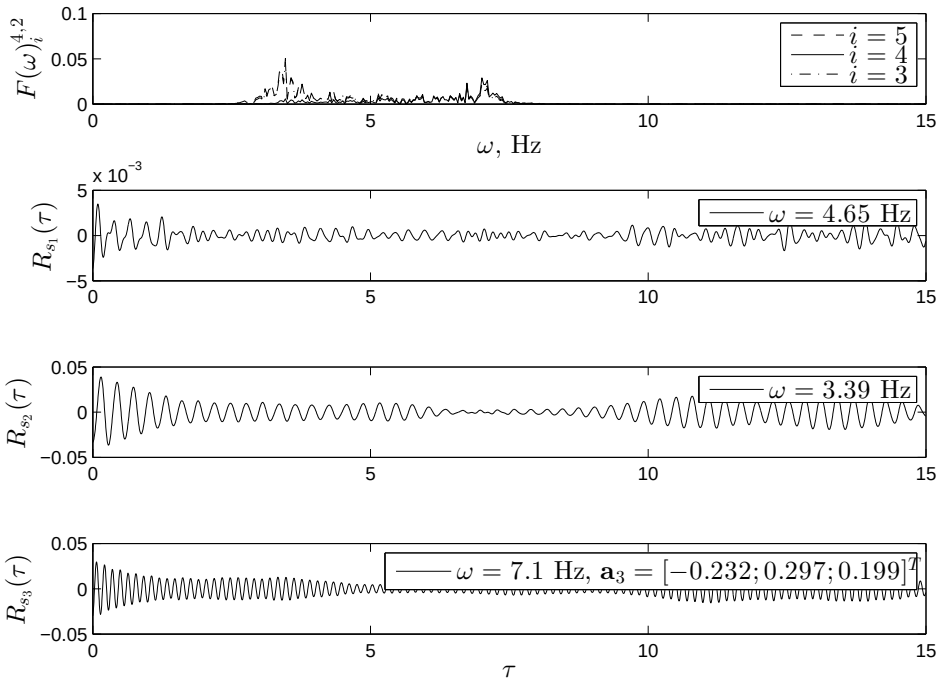

Figure 5.9: 5-DOF with TMD: Source separation using the SPWT coefficients of three measurements and PARAFAC decomposition

noted that according to Table 5.1, a maximum of 4 sources can be extracted from 3 sensors using PARAFAC-only method. On the other hand, using the PSBSS method, it is possible to identify all the 6 modes using just 3 sensors, which is a significant advantage.

The scale level for the ensuing analysis is further reduced to 3, where only 4 sensors are assumed to be available. In doing so, the number of SPWT coefficients is further reduced to 8. Fig. 5.10 shows the successful separation of 4 structural modes using the proposed method. Table 5.4 shows the comparison of the proposed method for different measurement cases. Details of the estimated frequencies and damping ratios are shown in Table 5.6.

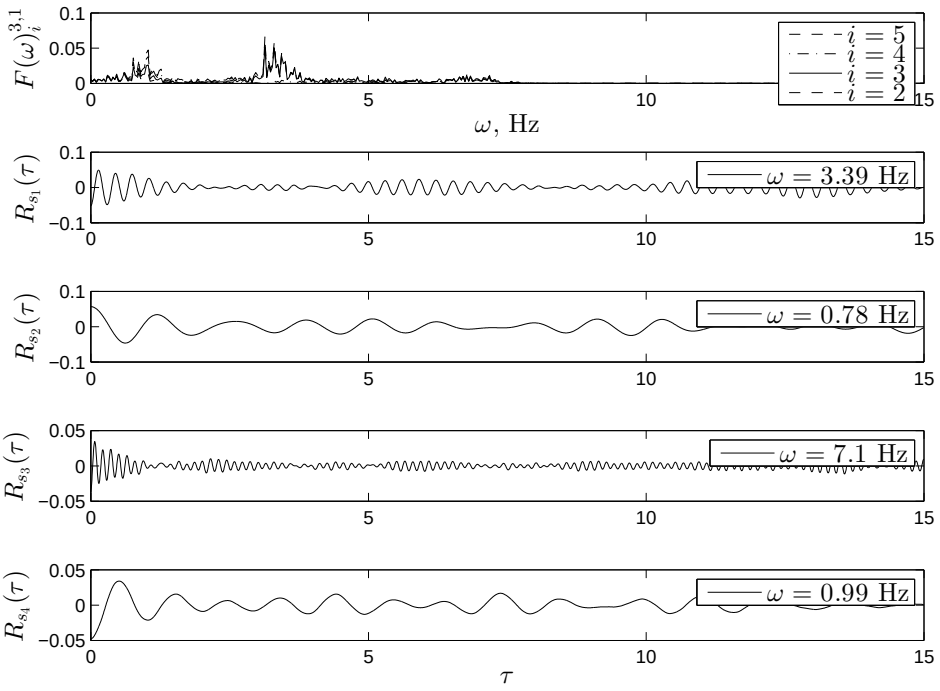

Figure 5.10: 5-DOF with TMD: Source separation of SPWT coefficients of four responses using Rank-4 PARAFAC decomposition

5.4.4 Application of the PSBSS method for a 10-DOF building

While the focus in the previous examples has been on partial mode estimation and its transformation to a full mode shape matrix using successive measurement setups, the next example demonstrates an approach to reduce the number of setups to achieve comparable performance in terms of estimating the modal parameters. Primarily, one needs to choose an appropriate sensor configuration [104] for modal identification using few measurements. It is shown that the PSBSS method is relatively insensitive to sensor configuration compared to the existing methods, which makes it advantageous for distributed sensing applications, where the exercise of finding an appropriate topology may not be practical.

In this section, a comparative study is performed between the PARAFAC-only method and the proposed method in selecting the suitable sensor configuration. For this purpose, a high-rise building model with 10-DOF [10] is considered. Such a system with relatively

Table 5.4: 5-DOF building with TMD: Performance of the PSBSS method

Case	n_m	u	n_c	Comments	Source Separation
SWPT-PCA	2	7	128	Imperfect filtering	Success ($\overline{\text{MAC}} > 0.99$)
SWPT-PCA	2	6	64	mode mixing of 2 sources	Failure ($\overline{\text{MAC}} < 0.93$)
PSBSS	2	6	64	mode mixing of 2 sources	Success ($\overline{\text{MAC}} > 0.99$)
PSBSS	3	4	16	mode mixing of 3 sources	Success ($\overline{\text{MAC}} > 0.99$)
PSBSS	4	3	8	mode mixing of 5 sources	Success ($\overline{\text{MAC}} > 0.98$)

large number of possible locations for measurements will allow us to highlight the benefits of the proposed algorithm. The lumped mass at all the floors is assumed to be $m_i = 1 \times 10^5$ kg, $i = 1, 2, .., 10$. The inter-story stiffness of all the floors are assumed to be $k_i = 180 \times 10^6$ N/m. The first six natural frequencies are 1.01, 3.01, 4.94, 6.75, 8.42 and 9.9 Hz. Fourier spectra of typical floor responses are shown in Fig. 5.11. The spectra shows the presence of 6 dominant modes within the frequency range of 0-10 Hz. Higher modes (after the sixth) have relatively little energy content. It may be noted that some of the vibration measurements, $x_i(t)$ (i.e., $i = 3, 6, 9$) exhibit relatively low energy in the 4^{th} and 5^{th} modes respectively due to that fact that these locations are the nodes for those modes. The effects of including such measurements are studied, and some important conclusions are included in the discussion.

First, the PBSS method is used to extract the first 6 PARAFAC components using rank-6 decomposition with 4 sensor measurements (as suggested by Table 5.1). However, there are a total 10 possible locations, and we need to select four out of all the sensor configurations (n_{sc}) is ${}^{10}C_4 = 210$. Ideally, one would determine the optimal location of sensors prior to performing the identification task. However, in many situations practical constraints may not allow one to predetermine such optimal locations and hence, one has to rely on locations that are accessible, which may or may not be optimal. Hence, it is

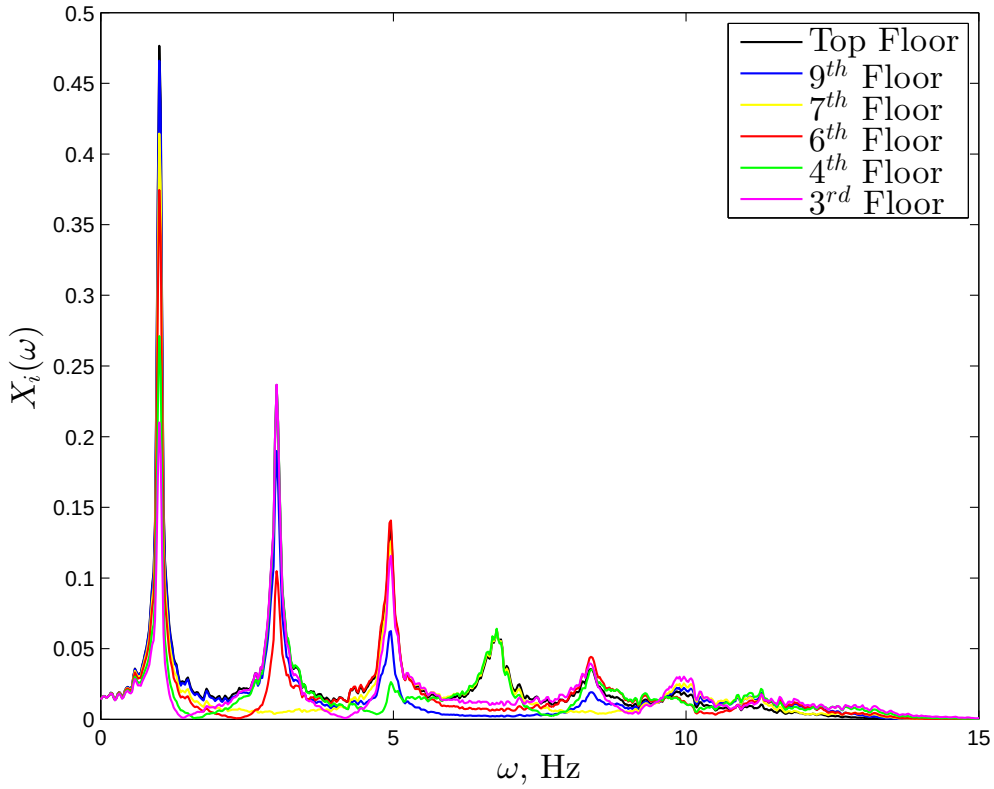

Figure 5.11: 10-DOF building: Fourier spectra of typical floor responses

useful to quantify the relative performance of PARAFAC-only method and the method proposed here. For this purpose, a frequency-based performance index is introduced:

$$\omega_R = \frac{1}{n_t} \sum_{l=1}^{n_t} \frac{\hat{\omega}_l}{\omega_l} \tag{5.33}$$

where ω_R is the average value of the ratio of the estimated ($\hat{\omega}_l$) and true natural frequency (ω_l), for all the target modes (say, n_t is the number of target modes which is six in the present case). Therefore $\omega_R = 1.0$ means perfect source separation. Here, the mean and standard deviation of ω_R for each measurement case is used to evaluate the performance. Table 5.5 shows that the performance of PBSS method deteriorates significantly with the

reduction in the number of sensors. For example, when complete sensor measurements

Table 5.5: Performance of PBSS method using different sensor configurations

			SNR=100		SNR=10	
case	n_m	$n_{sc} = {}^{10}C_{n_m}$	μ_{ω_R}	σ_{ω_R}	μ_{ω_R}	σ_{ω_R}
1	10	1	1.0	-	1.0	-
2	8	45	1.0	0.0	0.98	0.01
3	6	210	0.9	0.12	0.84	0.18
4	4	210	0.83	0.15	0.75	0.21

(i.e., $n_m = 10$ and $n_{sc} = 1$) are utilized, not surprisingly, μ_{ω_R} is 1. On the other hand, when $n_m = 4$ (which yields 210 number of possible sensor configurations), the performance of PBSS method deteriorates to yield μ_{ω_R} value of 0.83 (for the lower noise level case). Upon further examination of case-4, when the sensors correspond to locations $10-8-4-2$, they yield $\omega_{R_{\mu+\sigma}}$ value of 0.98. On the other hand, $\omega_{R_{\mu-\sigma}}$ (i.e., 0.68) results from a sensor configuration consisting of $9-6-3-2$ measurements. This is because the sensors are located at 3^{rd}, 6^{th} and 9^{th} floors, which contain structural frequencies with extremely low energy content, as these locations represent nodes for the structural modes. Thus, it is concluded that the quality of identification is dependent not only the number of measurements, but also on the energy distribution of the key modes in these measurements. Sensors corresponding to responses with low energy content in the key modes result in poor source separation, a problem that is exacerbated in the higher measurement noise case. Therefore, a suitable choice of sensor configuration is crucial for PARAFAC-only method in identifying low-energy modes under the partial measurement case.

Now we proceed to the PSBSS method to examine its sensitivity to the selected sensor configuration. For this purpose, we use the most critical previous sensor setup with $9-6-3-2$ contaminated for measurement noise of SNR=10, where the PBSS method fails to identify the modal parameters accurately and the performance is extremely sensitive

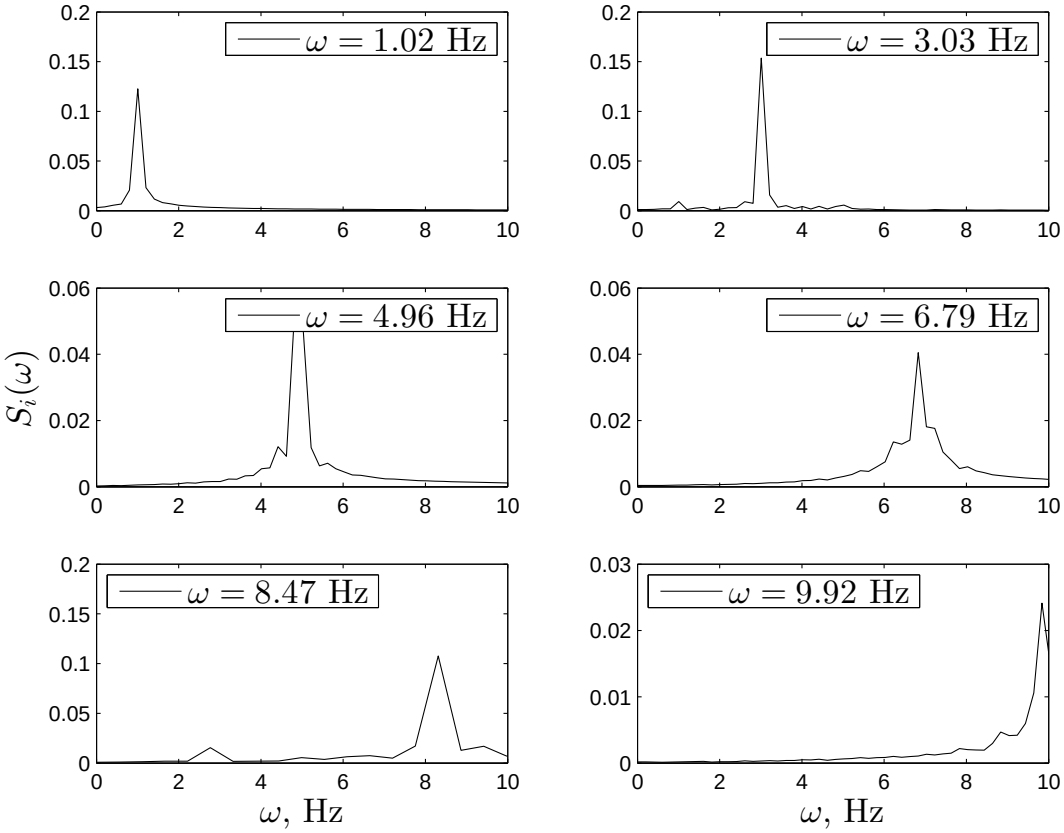

Figure 5.12: 10-DOF building: Fourier transform of auto-correlation of estimated sources using the PSBSS method

to the choice of sensor location. Fig. 5.12 shows the estimated sources using the PSBSS method, which indicates that the sources are clearly identified with reasonable accuracy ($\omega_R = 1.0$). Details of the estimated frequencies and damping ratios are shown in Table 5.6. The performance of the proposed method is quite robust due to wavelet decomposition. The subsequent PARAFAC-decomposition of the packet coefficients enables significant improvement of under-determined source separation. Further, it may be noted that the most critical sensor configuration was selected for demonstration, where some of the low frequency modes have relatively low energy contribution. Thus it is concluded that the performance of the proposed method is relatively robust to the exact choice of sensor location, which makes it preferable for decentralized applications, especially where the

exercise of finding a suitable topology may not be practical.

Table 5.6: Summary of the estimated natural frequency (ω) and damping (ξ) ratios for the numerical models using the PSBSS method

	5-DOF ($n_m = 2$)		5-DOF+TMD ($n_m = 2$)		10-DOF ($n_m = 4$)	
Mode	ω (Hz)	ξ(%)	ω (Hz)	ξ(%)	ω (Hz)	ξ(%)
1	0.91 [0.91]*	1.8 [2.0]	0.77 [0.78]	7.7 [7.67]	1.02 [1.01]	1.1 [1.0]
2	3.39 [3.37]	1.9 [2.0]	1.0 [0.99]	7.0 [7.2]	3.03 [3.01]	1.2 [1.0]
3	7.10 [7.11]	1.96 [2.0]	3.37 [3.37]	2.08 [2.16]	4.96 [4.94]	1.3 [1.4]
4	10.65 [10.66]	1.96 [2.0]	7.10 [7.11]	2.01 [2.03]	6.79 [6.75]	2.0 [1.8]
5	12.75 [12.73]	2.01 [2.0]	10.66 [10.66]	1.99 [2.0]	8.47 [8.42]	2.4 [2.2]
6	[*True values]		12.71 [12.73]	1.96 [2.0]	9.92 [9.9]	2.7 [2.5]

5.5 Summary

A novel decentralized ambient modal identification method is proposed that enhances the performance of sparse BSS using PARAFAC decomposition. In the proposed method, under-determined modal identification is solved within the framework of sparse BSS where the redundant stationary wavelet packet transform is employed to generate an over-complete dictionary of sparse bases. In order to reduce the computational effort, the tensor algebra tool, PARAFAC, is utilized, which allows us to use a higher scale level that would be possible based on the fundamental frequency of interest and the sampling frequency. It is observed that the proposed PSBSS method successfully improves the upper bound of source separation of PARAFAC, and is relatively insensitive to the choice of sensor configuration, which makes it suitable for the decentralized modal identification. The proposed method is validated using a series of numerical simulations. The results indicate that the proposed method is robust to noise, sensor configuration, and requires significantly less computational overhead than in its native form, and hence has significant potential for ambient modal identification problems in decentralized applications for civil infrastructure.

Chapter 6

Experimental studies

This chapter is devoted to demonstrate the application of the algorithms developed in the previous chapters to the vibration measurements obtained from three different sets of experimental data: (1) lab-scale model, (2) UCLA Factor building, and (3) a pedestrian bridge located at Brossard, Quebec, Canada.

6.1 Lab-scale experiment

The bench-scale two-storey model used to conduct experiments is shown in Figure 6.11. The structural model consists of two floor weights, 140 N each. Flexural stiffness is provided by four vertical L-shaped aluminium sections with a flange width and thickness of 1.30 cm and 0.16 cm, respectively. The vertical separation of each floor is 70 cm. An electrodynamic shaker as shown in Figure 6.1 is connected to the first floor level, and the floor accelerations are recorded using low-frequency accelerometers at both the floor levels, in both directions. A stinger is used to attach the shaker to the structure to impart the axial force, but protect the model against excessive lateral movements, moment and torsion. The stinger used in the test setup is a 3 mm diameter threaded steel rod with a length of 178 mm [46].

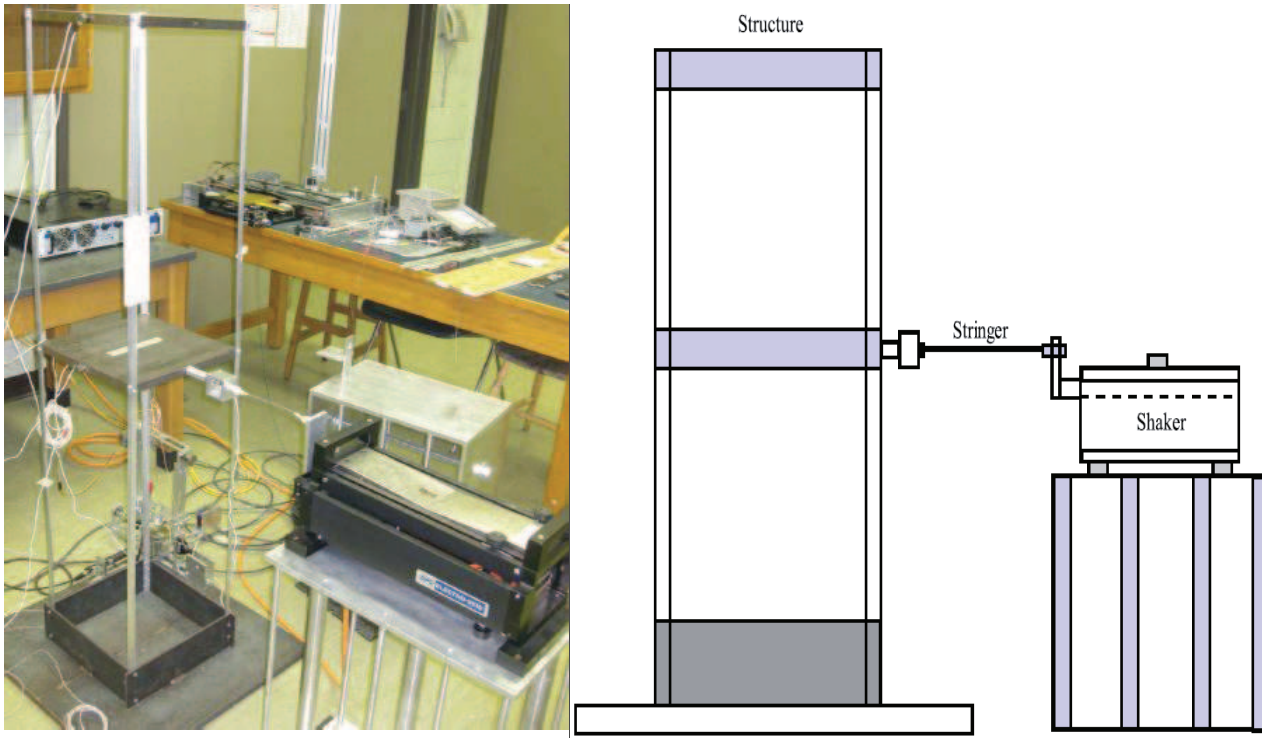

Figure 6.1: Experimental Set-up

A mixture of broadband noise sampled from a normal distribution is added to a deterministic sine wave of frequency 4.0 Hz and applied to the structure using the shaker, for a duration of 1 min. The acceleration data is sampled at 100 Hz and acquired using a data acquisition system. The decentralized algorithms are implemented on the vibration measurement data from two floors and the modal parameters are identified as illustrated in Fig. 6.2. The bootstrap estimates of the statistical measures are reported in Fig. 6.2, from which the modal responses are identified and subsequently the modes are estimated. The excitation frequency with a frequency of 4.0 Hz is clearly eliminated as an unwanted

frequency in $f_i^{5,5}$ using the proposed method. The details of the modal identification are tabulated in Table 6.1. The mode shapes are normalized with respect to upper floor, and are shown in Fig. 6.3.

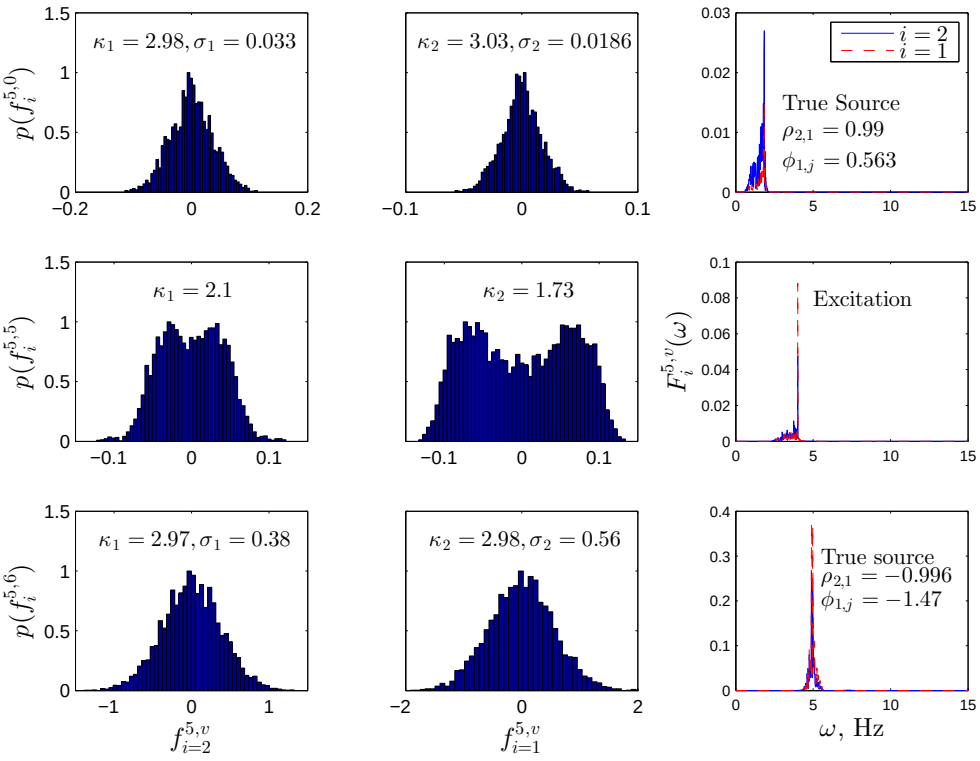

Figure 6.2: Details of identification using the PDF of $f_2^{5,v}$ and $f_1^{5,v}$

Table 6.1: Details of the identification results

Mode, #	ω_n (Hz)	ξ_n (%)
1	1.84	2.46
2	4.88	4.84

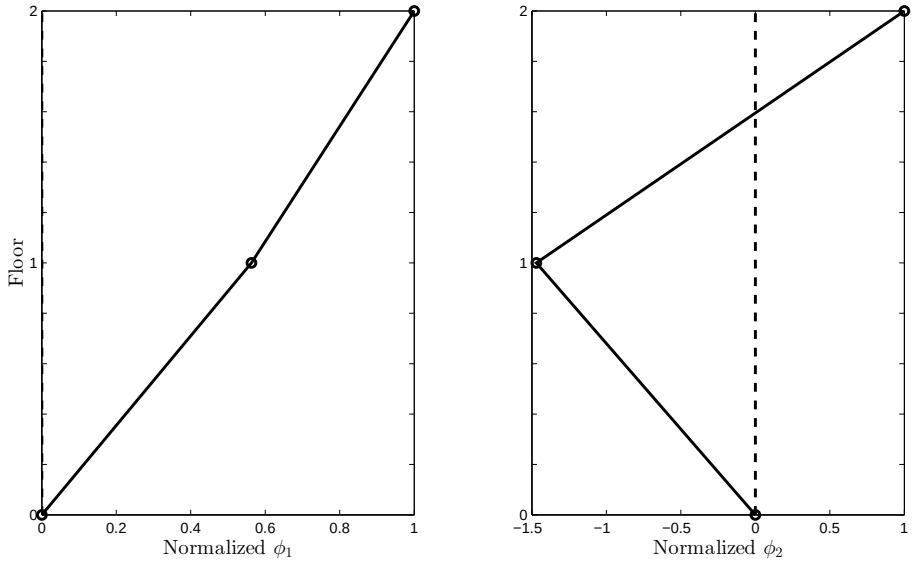

Figure 6.3: Mode shapes of the experimental model

6.2 UCLA Factor building

In order to demonstrate the application of the proposed identification methods to full-scale data [115, 114], recorded ambient responses from the University of California, Los Angeles, UCLA Doris and Louis Factor building (UCLAFB) are utilized. A general layout of this building is shown in Fig. 6.4, which houses several centers for the health sciences and other biomedical facilities of UCLA.

This building is one of the most heavily instrumented buildings in North America, whose vibration data in real-time is made available for researchers world-wide through a remote data-base server. Designed and constructed in the late 1970s, the 17−story 216.5 ft high building consists of a special moment resisting steel frames (SMFs) supported by concrete bell caissons and spread footings. Following the 1994 Northridge earthquake, the building was instrumented with an array of 72 Kinemetrics FB-11 uniaxial-accelerometers at the floor levels including the basement and the sub-basement levels. Each level has two pairs

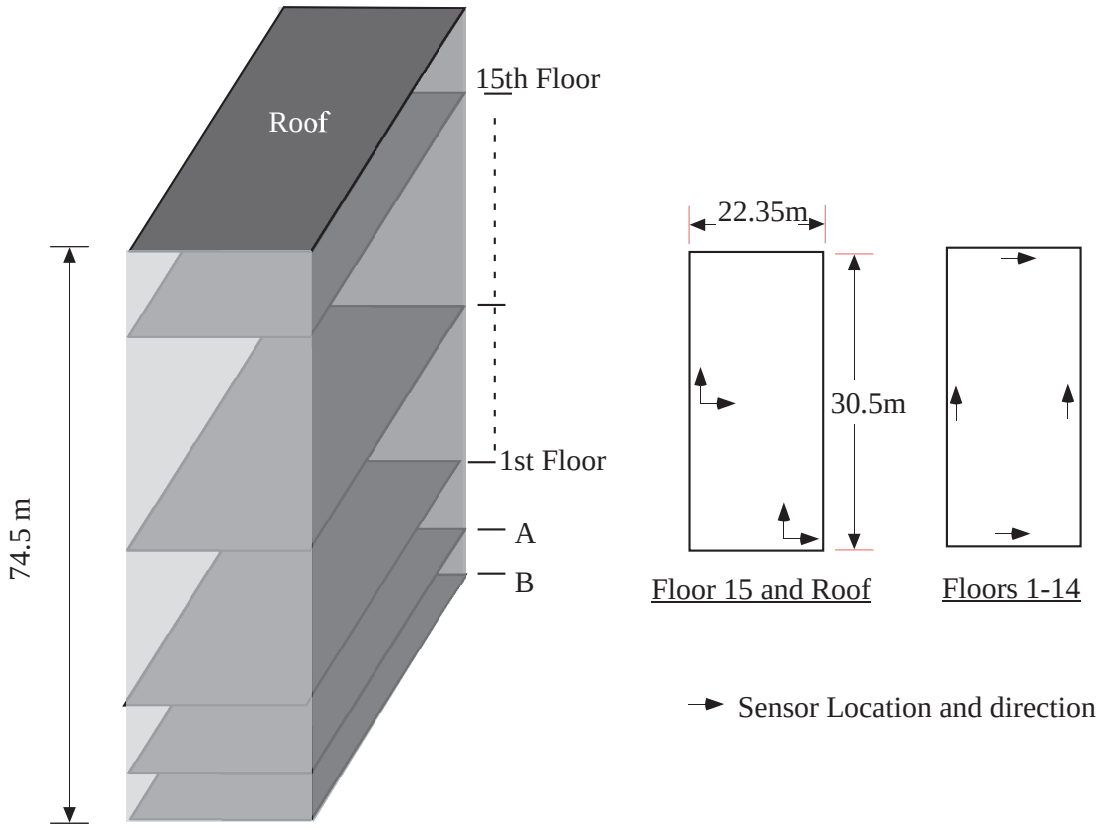

Figure 6.4: Sketch of the UCLAFB with the sensor locations

of orthogonal sensors parallel to the NS and EW directions as shown in the Fig. 6.4. In 2003 a 24−bit network was installed to continuously record data, which managed to record several minor earthquake events. Please refer to the details here [67, 123, 96, 44, 112].

The basic ideas proposed in this paper are implemented on the data recorded from the UCLA Factor building (UCLAFB). With 72 state-of-the-art accelerometers, this building is one of the most densely instrumented buildings in North America. Although the data in this example was obtained using wired sensors, the data from two sensors are processed at-a-time to calculate the partial mixing coefficients. The authors recognize that there are issues such as loss of data that is unique to wireless implementation that are not present in the wired data collection; however, such issues are considered beyond the scope of this paper. Only 2 sensor measurements are used at-a-time to determine the partial mixing

coefficients, and the proposed algorithm can be implemented in a decentralized wireless setting, or in a mobile sensing application. These partial mixing coefficients are then combined to yield the complete modal information. The UCLAFB is a particularly useful test-bed for this study as the results obtained form the results can be compared against published results for the same structure by independent researchers [67, 123, 96, 44, 112]. The focus of the current study is the algorithmic development, while the actual wireless (or mobile) implementation is reserved for the second full-scale study.

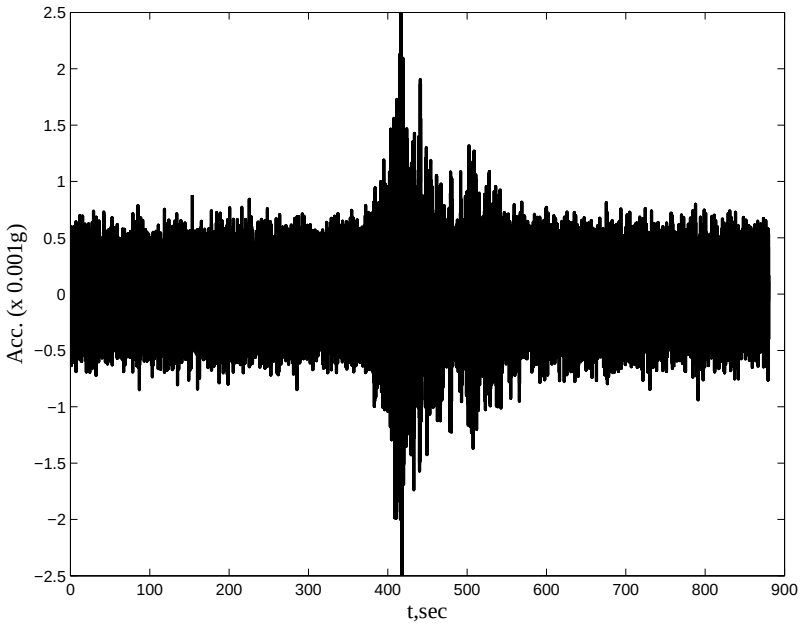

Figure 6.5: Roof acceleration of UCLAFB in NS direction

For the current identification study, floor accelerations recorded on September 28, 2004 at 10:15 AM PDT are used. Typical measured accelerations at roof is plotted in Fig. 6.5. Sudden jump in the roof acceleration at $t = 400$ s indicates the occurrence of Parkfield earthquake. The earthquake with $M_w = 6.0$ on the moment magnitude scale originated in Parkfield, CA, epi-centered 163 miles from the UCLAFB. The peak acceleration recorded at the roof of UCLAFB was $0.0025g$. The first 400 seconds of ambient response data prior to the earthquake is used for the present study.

Table 6.2: Sensor locations

Case	Sensor locations (floor levels)	Time segments (sec)
1	$16-15-14$	$1-50$
2	$16-13-12$	$51-100$
3	$16-11-10$	$101-150$
4	$16-9-8$	$151-200$
5	$16-7-6$	$201-250$
6	$16-5-4$	$251-300$
7	$16-3-2$	$301-350$
8	$16-1$	$351-400$

6.2.1 Application of the SWPT-PCA method

The estimation of partial mixing coefficients using the SWPT-PCA method [115] is employed first. Then, the partial mixing coefficients are combined to estimate the full mixing matrix. The roof sensor is assumed to be the reference sensor. It is further assumed that only 3 sensors are available at-a-time. Table 6.2 shows the successive estimation of partial mixing coefficients, while the data obtained from non-overlapping time segments are used for individual estimation cases. Total number of sensing cases is 8, with a 50 s data duration for each individual case. The details of the sensor locations and the corresponding time segments are shown in Table 6.2.

The proposed SPWT-based technique is applied in each of the eight individual cases. $db5$ wavelet basis and a scale level 8 are chosen for the analysis. The number of target mode, N_t is chosen as 6 in each of the 3 directions. Therefore the total number of desired target mode is 18. The mean (μ_p) and coefficient of variation (COV_p) of the estimated frequencies (ω) and damping (ξ) of all the eight cases using the proposed method are listed in Table 6.3. The results are compared with the model order-based Stochastic Subspace Identification (SSI) technique as reported by others in the literature [123]. The estimated frequencies are consistent with the values as reported in the literature [67, 96, 123, 44].

By concatenating the partial mixing coefficients obtained in each case, the normalized

Table 6.3: Identified ω and ξ of the UCLAFB from Parkfield ambient vibration data

Mode	Shapes	ω (Hz)			ξ (%)		
No	Dir	SSI	μ_e	COV$_e$ (%)	SSI	μ_e	COV$_e$ (%)
1	EW	0.545	0.534	1.1	5.1	4.2	24.5
2	NS	0.588	0.579	1.7	8.3	4.6	34.2
3	Torsion	0.807	0.792	1.8	10.8	5.2	22.4
4	EW	1.63	1.67	1.6	2.1	2.8	15.3
5	NS	1.79	1.80	2.1	1.4	1.9	14.4
6	Torsion	2.48	2.48	1.5	2.9	3.6	25.9
7	EW	2.83	2.85	0.9	2.2	2.7	23.8
8	NS	3.06	3.07	1.7	1.3	2.2	14.3
9	Torsion	4.02	4.04	3.2	2.9	3.7	24.1
10	EW	-	4.2	2.2	-	3.0	23.3
11	NS	-	4.76	2.8	-	2.5	27.9
12	Torsion	-	5.12	1.8	-	3.2	25.5
13	EW	-	5.2	2.1	-	3.9	33.1
14	NS	-	5.75	2.4	-	4.0	23.2
15	Torsion	-	6.25	2.7	-	3.3	28.5
16	EW	-	7.3	3.2	-	3.9	32.8
17	NS	-	7.8	3.2	-	3.5	26.7
18	Torsion	-	8.6	3.7	-	4.9	22.9

mode shape matrix is estimated for the first 18 modes. The mode shapes for the first nine modes are shown in Fig. 6.6. The correlation between the vibration modes obtained using the complete set of sensors-collected over the entire 400 sec duration and processed in a batch mode-versus the estimated modes (using the decentralized algorithm) is calculated using the modal assurance criterion (MAC) and shown in Fig. 6.7. In this case, data from three sensors are processed at a time. In calculating the correlations, three cases are considered: i) the entire data is processed in a decentralized fashion assuming that all the sensors have access to the entire data, ii) the data is divided into non-overlapping segments of 50 sec and processed separately, and iii) the data is divided into non-overlapping

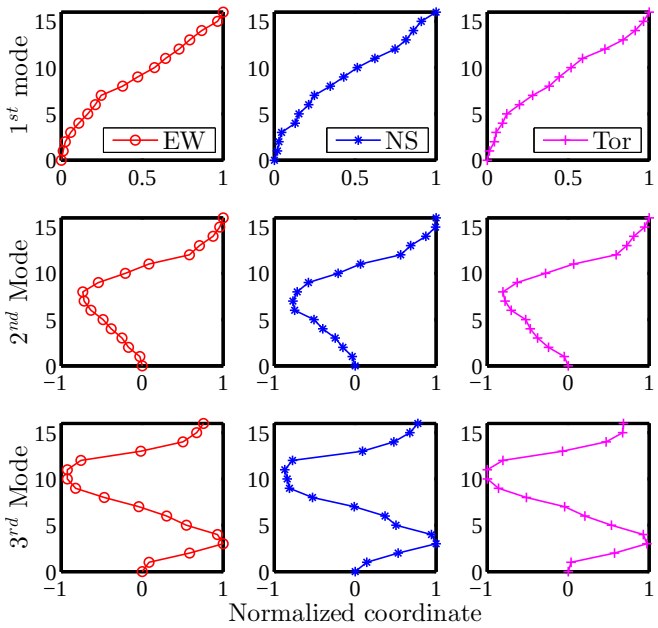

Figure 6.6: 1^{st}, 2^{nd} and 3^{rd} modes in EW, NS, and torsional directions

segments of 10 sec and processed. The partial mixing coefficients are calculated for the non-overlapping (or overlapping for the first case) time segments and then concatenated.

From the results in Fig. 6.7, for the first two cases, the quality of identification is consistent with those obtained using complete sensor data and processed in a batch mode. Particularly noteworthy is that the first case (when the entire data is processed in a decentralized fashion) yields almost identical results with the case of centralized processing using full sensor data. The performance of the algorithm deteriorates as the length of the time segments is reduced in the non-concurrent cases. In the third case, i.e., when only 10 sec of data are used in the algorithm, the MAC numbers obtained only for the first three modes are greater than or equal to 0.98. This means that the data length is a critical parameter that needs to be selected carefully depending on the application. Longer data segments yield better results, however it comes at the cost of higher computational and transmission loads. These issues are reserved for future work.

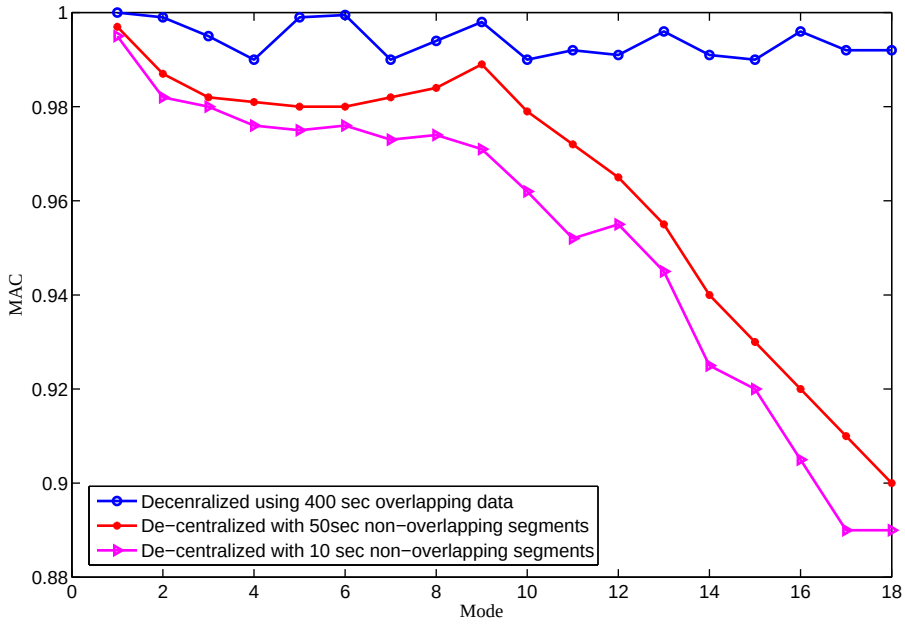

Figure 6.7: Results from the proposed method compared to the full sensor density case

6.2.2 Application of PSBSS method

The proposed technique is applied to the data obtained from each of the eight individual groups. As with the numerical examples, $db5$ is chosen as the wavelet basis. Based on the sampling frequency of 100 Hz and the lowest structural frequency of 0.53 Hz, a maximum scale level of 8 was used ($s = 8$) in the SWPT-PCA method [115]. However, this scale level produces $2^8 = 256$ SWPT coefficient pairs for each of the three partial measurement set ups. In this example, instead, a scale level of 5 is chosen, ($u = 5$), which results in only 32 SWPT coefficient pairs. Finally, PARAFAC is employed to extract the sources from these measurements.

Fig. 6.8 shows the Fourier spectra of the SWPT coefficients of $F_i^{5,1}$ obtained by processing three floor measurements, $i = 14, 15, 16$ in the east-west direction. Multiple frequencies are observed from this spectra of the SWPT coefficients. Fig. 6.8 shows the

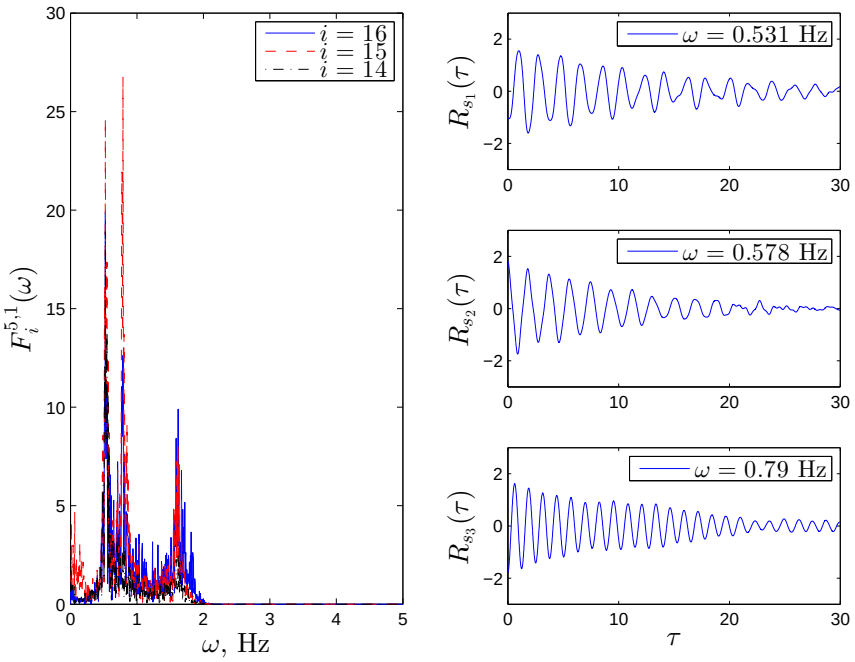

Figure 6.8: UCLAFB: Fourier spectra of the SWPT coefficients $F_i^{5,1}$ and the identified sources

separated sources using the the proposed method using PARAFAC decomposition with 3 components. It is evident from the aforementioned figure that the sources with frequencies $\omega = 0.531$, 0.578 and 0.79 Hz are clearly separated. Similar exercise is performed with respect to the SWPT coefficients of $F_i^{5,2}$, whose Fourier spectra are shown in Fig. 6.9, where the structural modes with frequencies 1.64, 1.8 and 2.52 Hz are identified.

The number of target modes n_t is 5 in each of the 3 directions. Therefore, the total number of desired target modes is 15. The mean (μ_e) and the coefficient of variation (COV_e) of the estimated frequencies (ω) and damping ratios (ξ) for all the eight cases using the proposed method are listed in Table 6.4. The results are compared with the data-driven stochastic subspace identification (SSI) technique and the results reports for the same structure in the literature [67, 96, 115]. By concatenating the partial mixing coefficients obtained in each case, the full mode shape matrix is estimated for 15 modes.

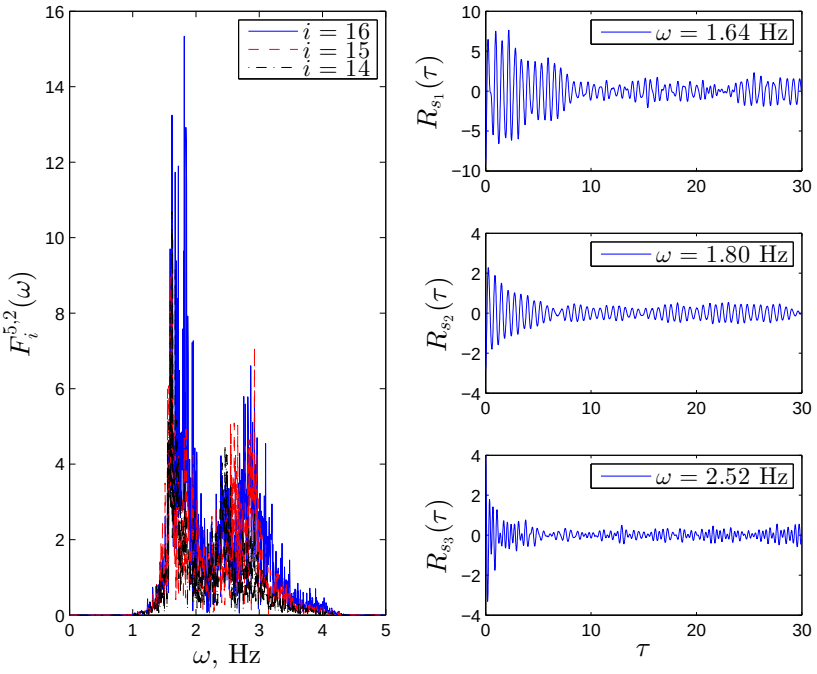

Figure 6.9: UCLAFB: Fourier spectra of the SWPT coefficients $F_i^{5,2}$ and the identified sources

6.3 Wireless Sensor Applications

One of the main advantages in the decentralized methods proposed in this thesis is the potential for application in wireless sensor networks. Though the algorithms are equally applicable to wired applications, the possibility of implementing processing tasks (such as SWPT) on the sensor itself makes these algorithms particularly attractive to wireless implementation. A typical wireless sensing unit primarily includes three subsystems [121, 78]: the sensing interface (to receive and samples the measurements), computational core or an on-board microprocessor (for digital data processing and local storage) and wireless communication system (for data transmission with other sensors or network server). In particular, a sensor node in WSSN performs the local data acquisition, data processing and communication with other nodes in the network and a central base station. A variety

Table 6.4: Identified ω and ξ of the UCLAFB from ambient vibration data using PSBSS method

Mode	Shapes	ω (Hz)			ξ (%)		
No	Dir	SSI	μ_e	COV$_e$ (%)	SSI	μ_e	COV$_e$ (%)
1	EW	0.545	0.531	0.9	5.1	4.1	22.5
2	NS	0.588	0.578	1.4	8.3	5.3	24.2
3	Torsion	0.807	0.790	1.5	10.8	7.2	22.4
4	EW	1.63	1.64	1.4	2.1	2.3	12.3
5	NS	1.79	1.80	1.9	1.4	1.8	12.4
6	Torsion	2.48	2.52	1.7	2.9	3.7	25.9
7	EW	2.83	2.84	1.1	2.2	2.6	21.8
8	NS	3.06	3.08	1.6	1.3	2.5	15.3
9	Torsion	4.02	4.05	3.1	2.9	3.5	24.3
10	EW	-	4.21	2.1	-	3.2	22.3
11	NS	-	4.74	2.4	-	2.5	23.9
12	Torsion	-	5.09	1.7	-	3.5	25.6
13	EW	-	5.22	2.0	-	3.9	24.4
14	NS	-	5.71	2.6	-	4.1	24.2
15	Torsion	-	6.23	2.9	-	3.8	27.5

of commercially available motes (i.e., micaZ [102, 54], wireless modular monitoring system (WiMMS) [81, 82, 26, 159], Narada sensors [133], or iMote2 [121, 76]) have been recently used in several structural health monitoring applications. In this thesis, Memsic's Lotus® motes [89] are utilized for demonstration. It is important to note that the preprocessing algorithms themselves were not implemented directly on the board; the motes were used for their sensor and wireless data transmission functions only.

6.3.1 Softwares

The Lotus mote's software platform consists of LotusView and Moteworks™ architectural components [89]. LotusView is designed to create an interface between user and a deployed

network of wireless sensors. It simplifies the deployment strategies of sensors and their real-time monitoring capabilities by displaying and analyzing the incoming data collected by the motes. On the other hand, Moteworks™ enables the development of custom sensor application including programming the motes to perform a specific task. MoteConfig, a graphical-user-interface of Moteworks™, is finally used to upload the associated firmware onto the motes and gateway.

Lotus motes are primarily programmed in Moteworks™ using XMesh/TinyOS firmware [88]. XMesh™ [87] is MEMSIC's multi-hop mesh networking protocol that has various options including low-power listening, time synchronization, network-to-base and base-to-network routing [87]. All the sensors and data acquisition boards are supported with XMesh™ enabled applications based on TinyOS. TinyOS [137] is a lightweight operating system with small memory footprint and therefore suited to the limited resources of wireless sensors, which finally makes the sensors cheaper, and robust along with deployment simplicity. Such longevity, embedment and wireless communication enable the wireless sensors different than traditional wired sensing system.

6.3.2 Lotus radio processor module

The Lotus mote (LPR2400) is an advanced wireless sensor node platform [86], consisting of computational core, sensing interface and wireless communications. LPR2400 is built around 100 MHz 32-bit ARM low-power Cortex M3 based micro-controller (core) integrated with RF231 (ZigBee) IEEE 802.15.4 compliant radio (responsible for wireless communication), which makes it suitable for large scale embedded applications featuring a high level of integration and low power consumption. Contex micro-controller of LPR2400 has 512 kB of program memory, 64 kB of data memory (RAM), and 64 MB of external flash memory. Its size is $76 \times 34 \times 7$ mm (see Fig. 6.10(a)-(b)) and it weighs just 18 grams [86]. The Lotus platform integrates a 2.4 GHz on-board antenna which provides a

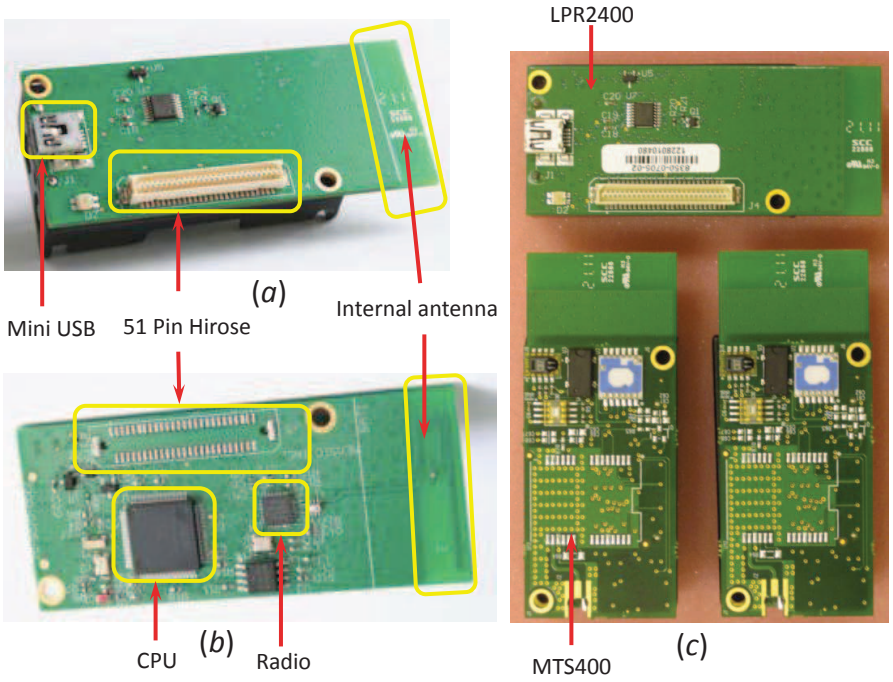

Figure 6.10: (a) Top view and, (b) bottom view of LPR2400, (c) one single LPR2400 and two LPR2400 motes with sensors MTS400 on top

nominal range of about 100 meters and supports 250 kbps (kilo bits per sec) data rate. The design is modular and a single processor board can be configured to run the sensor application and the network-to-radio communication stacks simultaneously. LPR2400 is connected to the sensor using the sensing interface comprising of 51-pin expansion connector that supports analog inputs, 10 bit analog-to-digital converter (ADC), and digital interfaces such as I^2C port, serial peripheral interface (SPI) and universal asynchronous receiver/transmitter (UART). These interfaces make it easy to connect to a wide variety of external peripherals. A detailed comparison of Lotus motes with different other commercially available wireless sensors e.g., micaZ [102, 54], wireless modular monitoring system (WiMMS) [81, 82], Narada sensors [133], or iMote2 [121, 76] are listed in Table 6.5.

Table 6.5: Comparison of Lotus motes with other commercial motes

Specification	MicaZ	WiMMS	Narada	iMote2	Lotus
Clock speed (MHz)	7.37	40	8	13-416	100
Processor (bits)	ATMG128L (8)	Dual Atmel (8) & PowerPC (32)	ATMG128L (8)	XScale (32)	Cortex M3 (32)
ROM (Bytes)	128K	448K	128K	32M	512K
RAM (Bytes)	4K	26K	4K (S) 128K (F)	256K (S) 32M (SD)	64K (S) 64M (F)
Radio Type	CC2420	RangeLAN 2	CC2420	CC2420	RF231
ADC (bytes)	10	16	16	–	10
Battery	2×AA	5×AA	5×AAA	3×AAA	2×AA

6.3.3 Sensor board

MTS400 sensor module [88] is connected to the Lotus motes (LPR2400) to acquire the vibration measurements. It is primarily developed in conjunction with UC Berkeley and Intel Research Labs [88]. The sensor board has several other sensing protocols in addition to the accelerometer used in this study. The dual-axis accelerometer (ADXL202JE) is rated to generate acceleration data with 2 mg resolution and 167 mV/g of sensitivity. The MTS400 sensor board is connected to LPR2400 using 51-pin expansion connector as shown in Fig. 6.10(c). These energy-efficient digital MEMS (micro electro mechanical systems) sensors provide extended battery-life and performance wherever low maintenance field-deployed sensor nodes are required. The detailed specification of MTS400 can be found in Table 6.6 [88]. Data logging and display of the upcoming data is supported by Memsic's LotusView user interface [89]. For our instrumentation purposes, the sensor boards are programmed such that it sends 20 samples per radio packet achieving a sampling rate of 140 Hz for individual sensors.

Table 6.6: Specification of MTS400

Sensor type	Analog devices ADXL202JE
Channels	X (ADC1), Y (ADC2)
Range	$\pm 2g$
Sensitivity	167 mV/g
Resolution	2 mg
Operating range (T)	-10^o to 60^o

6.3.4 Experimental verification

A laboratory experiment is conducted on a bench-scale two-storey model using the Lotus wireless sensor network as shown in Fig. 6.11 (a). The Lotus wireless sensor motes (a combination of LPR2400 and MTS400) are placed on the plane of the floor using the mounts comprising of two aluminum angles, L12.5×12.5 mm as shown in Fig. 6.12(b)-(c). As shown in Fig. 6.12(a), one Lotus mote (LPR2400) is attached to the Laptop which acts as a gateway to receive data from the sensors. The top floor level of the model is excited by a hammer impact, and the floor accelerations are recorded using both wired and wireless sensors. Fig. 6.11(c) shows the comparison of the normalized Fourier spectra of the top floor acceleration collected by wired and wireless sensor. The result shows the accuracy of the wireless sensors in the data collection and confirms its suitability in the full-scale modal identification [119].

The proposed methods [115, 118] are then applied to partial measurements. Two response measurements at the 1^{st} and the 2^{nd} floors are processed using SWPT up to scale level $s = 4$. $db5$ wavelet basis is chosen. The coefficients at the last scale level ($2^s = 16$) of decomposition are used to estimate the partial mixing matrix. Of these, the coefficients containing low-energy noisy components are discarded using a thresholding criterion based on RMS values [115].

In the next step, PCA is performed with the selected SWPT coefficient pairs, and the

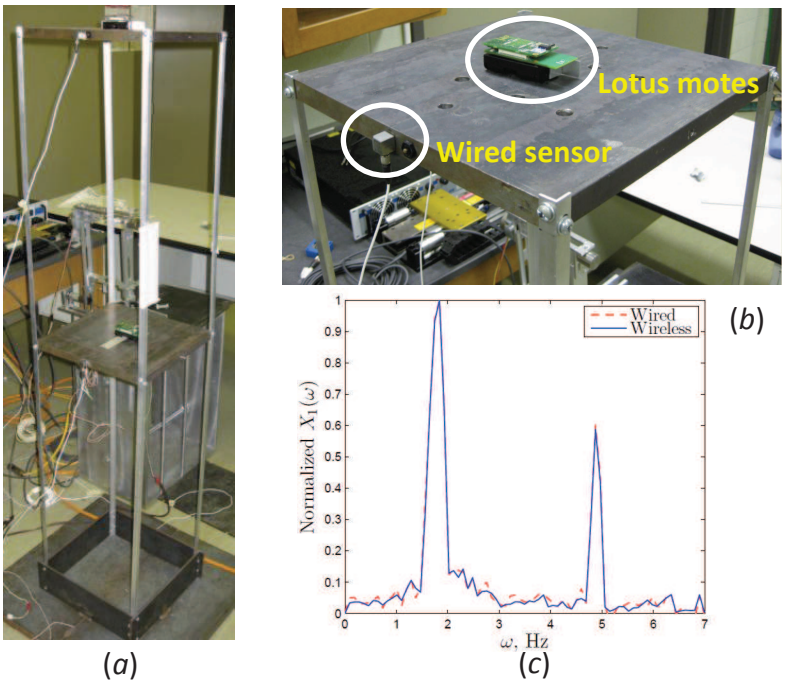

Figure 6.11: (a) Experimental set-up with wired and wireless sensors, (b) a close view of attached wired and wireless sensors, (c) Fourier transform of the top floor acceleration

modal responses are identified. Fig. 6.13 shows the plots of $f_i^{4,0}(t)$ and $f_i^{4,2}(t)$ for $i = 1-2$. From the Fourier spectra, it can be observed that $f_i^{4,0}(t)$ and $f_i^{4,2}(t)$ are nearly mono-component. The principal directions of the major and minor PCs are shown in Fig. 6.13. The corresponding RCN values are 0.001 and 0.007 for $f_i^{4,0}(t)$ and $f_i^{4,2}(t)$, respectively. Such low value of RCN ($\ll 1$) in $f_i^{4,0}(t)$ indicates a nearly mono-component signal, and hence it is indicative of a structural mode. If the number of desired target modes is N_t, then the coefficients with first N_t lowest RCN values can be selected as sources. In this example, the number of target mode is 2 and thus the coefficients with first two lowest RCN are selected as the sources. The details of the modal identification are tabulated in Table 6.7. The mode shapes are normalized with respect to upper floor, and are shown in Fig. 6.13.

Next, sparse BSS method employing statistical characterization of sources is imple-

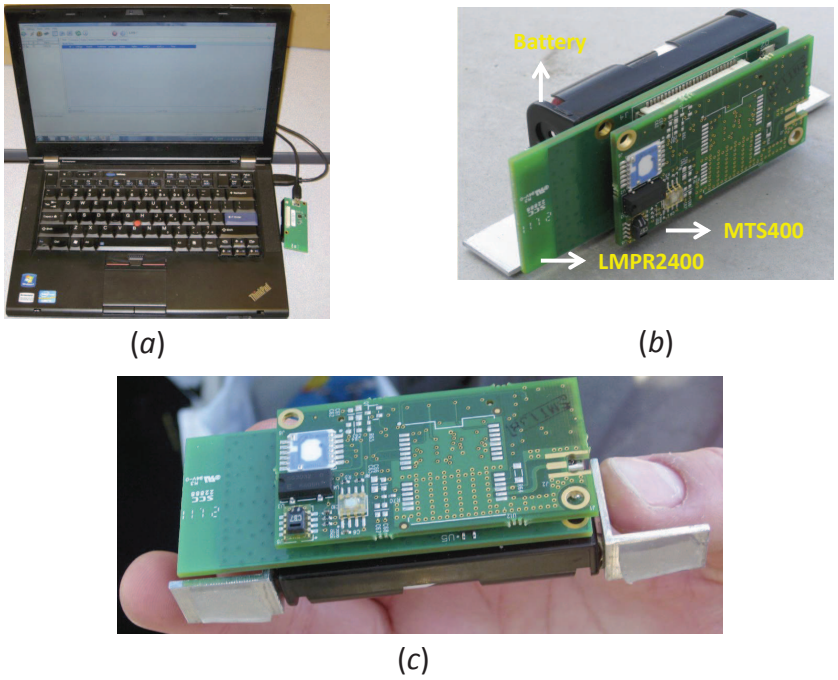

Figure 6.12: Wireless sensor kits (a) gateway (LPR2400), (b) sensor node (LPR2400+MTS400), (c) sensor with mounts

mented on the data. In this regard, the sample probability density function (PDF) of the selected SWPT coefficients of $x_1(t)$ and $x_2(t)$ are used. Fig. 6.13 shows the details of the identification using the information of PDF of $f_1^{4,v}$ and $f_2^{4,v}$. The second two columns and rows of Fig. 6.13 show the PDF of SWPT coefficients $f_i^{4,v}$ for $v = 0$ and 2 for $i = 1, 2$ respectively. In these sub-figures, κ and σ represent the kurtosis and standard deviation of the corresponding PDF respectively. It can be seen that the PDF of $f_i^{4,v}$ with $v = 0$ and 2 have the value of κ close to 3.0, which corresponds to belonging to a system mode. The absolute value of cross-correlation $\rho_{5,4}$ for those coefficients close to 1.0 implies a mono-component source, which can be considered as a modal response. The ratio of their standard deviation yields the mode shape coefficient and the sign of ρ determines the sign of the mode shape coefficients. In this fashion, the mixing coefficients can be estimated repeatedly using Eq. 4.17. For example, $f_1^{4,0}$ and $f_2^{4,0}$ have ρ value of +0.99 and standard

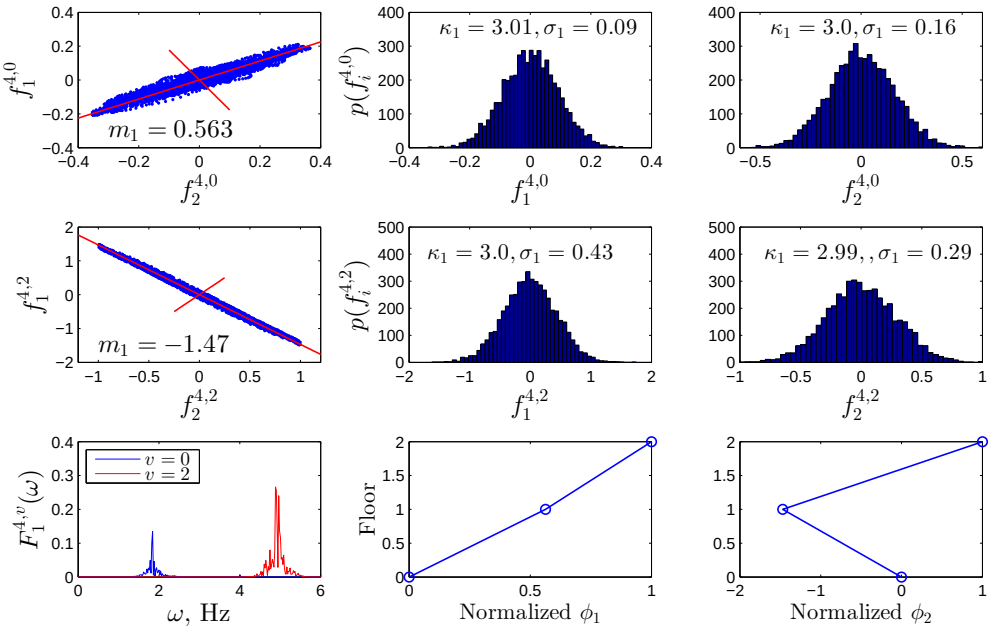

Figure 6.13: Details of identification using the sparse BSS method

deviation of 0.09 and 0.16 respectively, for which $\phi_{4,j}$ becomes $\frac{0.09}{0.16} = +0.563$. On the other hand, $f_1^{4,2}$ and $f_2^{4,2}$ have a ρ value of -1.0 and standard deviation of 0.43 and 0.29 respectively, for which $\phi_{4,j}$ is computed as $\frac{0.43}{0.29} = -1.47$. The identification results are compared with the SSI method [140] and tabulated in Table 6.7.

Table 6.7: Details of the identification results of the lab-scale experiment

Mode #	SSI		SBSS		MAC
	ω, Hz	$\xi(\%)$	ω, Hz	$\xi(\%)$	
1	1.84	2.38	1.84	2.46	1.0
2	4.87	2.5	4.88	2.46	0.99

6.4 Brossard bridge

6.4.1 Structural description of the bridge

Free vibration measurements of a pedestrian bridge located in Brossard, Quebec, are used to demonstrate the application of the proposed decentralized modal identification methods [115, 118]. MAADI (Most Advanced Aluminum Design and Inspection) Group from Quebec designed this 44 m long × 4 m wide aluminum pedestrian pony truss bridge (see Fig. 6.14) in Quebec. The bridge crosses Daigneault creek and connects a new subdivision

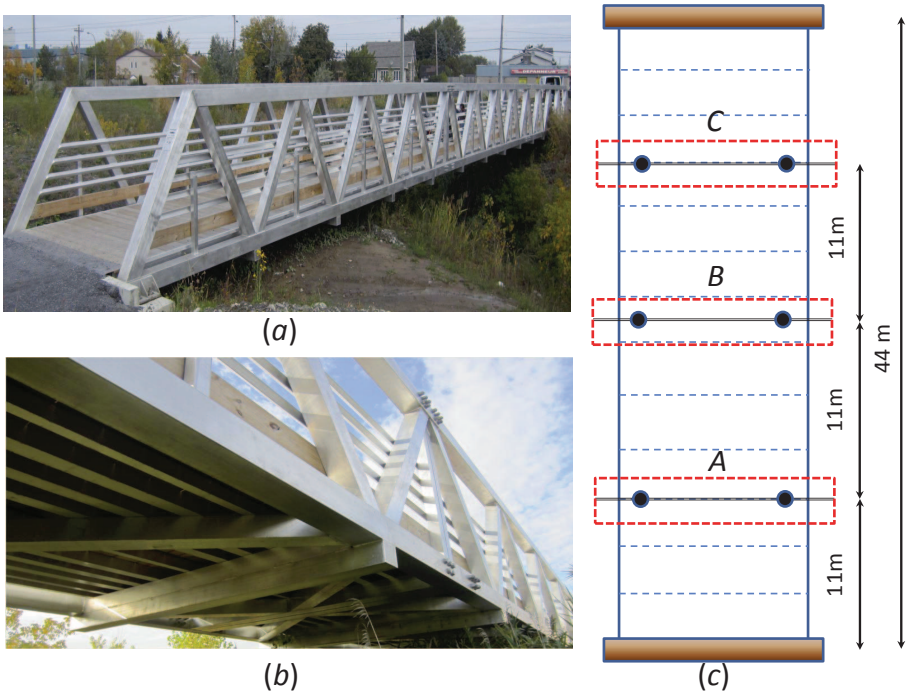

Figure 6.14: Bridge geometry: (a) side view, (b) bottom view, (c) sensor locations

from Rue Claudel to a major transportation and commercial area on Rue Grande Allee [134]. The truss extends approximately 2.8 m above the deck with a set of 254 mm square box sections at the top and bottom of the railing forming the main girders. The diagonal bracings are 152 mm box sections, and the lateral deck purlins are 203 mm box sections.

Eleven scantlings, ranging from 63-127 mm wide and 127 mm tall run along the length of the pressure-treated Southern yellow pine deck. The bridge is connected to a cast in-place concrete shallow footing with slotted bolted connections. During the fall of 2012, the structure was instrumented with both wired and wireless sensors (see Fig. 6.15) to evaluate its vibration performance.

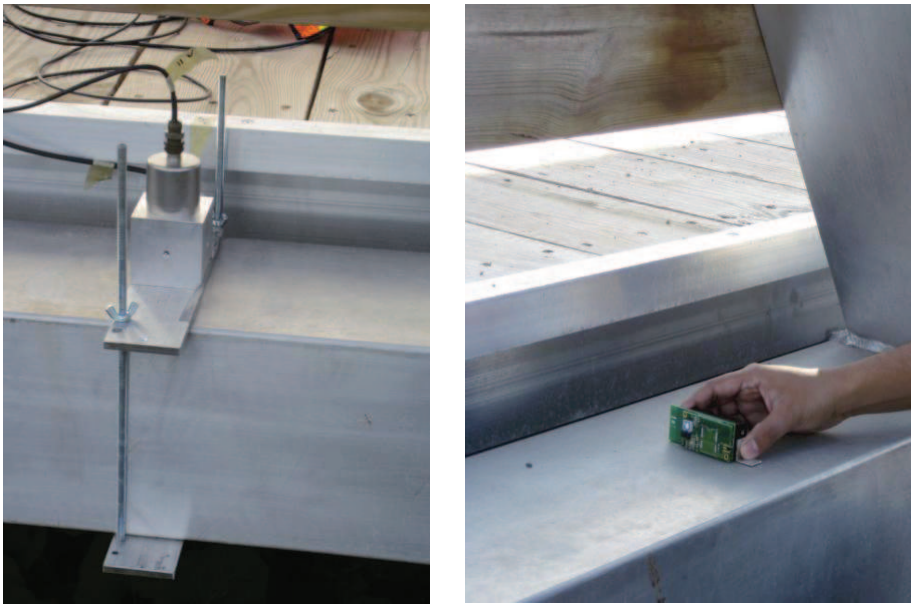

Figure 6.15: Sensor types (a) wired (PCB Piezotronics), (b) wireless (Lotus motes)

6.4.2 Centralized data processing using wired sensors

For this purpose, PCB Piezotronics high-sensitivity seismic accelerometers are used. The accelerometers have a frequency range of $0.07 - 300$ Hz, a sensitivity of 10 V/g, and measurement range of $0.5g$ ($g = 9.81m/s^2$). The sensor's signal output was continuously recorded at a sampling rate of 500 Hz. Acceleration data was collected using a 12-channel simultaneous data acquisition system with 16-bit ADC resolution. Total 12 sensors were

installed at total 6 locations (as shown in Fig. 6.14(c)) with two sensors at each node for measuring the vertical and lateral vibration. The sensors were installed on the top of the each of the bottom girders, thus approximately 4 m apart.

The free vibration data under heel-drop impact are first collected using 12 channels of sensors in centralized fashion and the system identification methods including second-order blind identification (SOBI) [13] and stochastic subspace identification (SSI) [140] are performed to estimate the modal parameters. Fig. 6.16(a) shows the Fourier transform of a typical vertical acceleration data. As shown in Fig. 6.16(b), SOBI results into 4 mono-component sources with frequencies 3.3, 5.9, 14.7, and 17.2 Hz respectively. However it generates two other sources where there are mode-mixing of two sources respectively as shown in Fig. 6.16(c). In fact, it is due to the presence of modes with low energy content. The wired measurements are then analyzed using stochastic subspace identification (SSI) method [140]. Fig. 6.17 shows the resulting stability diagram under various model orders and the modal frequencies are then selected based on the clustered data points of SSI results. Table 6.8 shows the details of the identification results from the SSI method and the SOBI method. It can be seen that the mono-component sources as obtained from SOBI match reasonably well with the frequencies obtained from SSI.

6.4.3 Decentralized system identification using wireless sensors

For the decentralized implementation of the proposed algorithm, Lotus wireless sensor nodes [89] are employed. Two Lotus motes from Memsic were installed on the bottom girders of the bridge (see Fig. 6.15(b)) at locations A, B and C of Fig. 6.14(b) respectively in three successive setups.

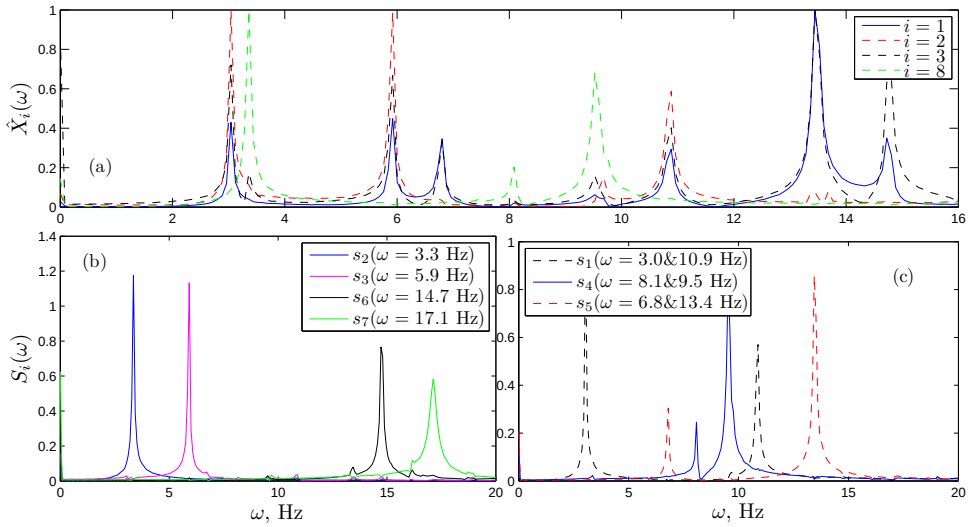

Figure 6.16: Typical vertical acceleration data: (a) FFT, and identification results using SOBI (b) separated sources, (c) typical mode mixing in the sources

Free vibration test

The free-vibration data was collected in each setup under identical loading condition namely heel-drop impact. The sensors acquired data for the motion in the same plane as the circuit board. The short dimension was assigned to the vertical direction and the long dimension was assigned to the lateral direction. Longitudinal response of the bridge was not deemed necessary. Fig. 6.18 shows typical free vibration data as collected by one of wireless sensor.

The proposed method (i.e., SWPT-PCA method) is then applied to the partial measurements. Two response measurements at the 1^{st} and the 4^{th} DOF are processed using SWPT up to scale level $s = 5$. $db5$ wavelet basis is chosen. The coefficients at the last scale level ($2^s = 32$) of decomposition are used to estimate the partial mixing matrix. Of these, the coefficients containing low-energy noisy components are discarded using a thresholding criterion based on RMS values [115]. The total number of coefficients with RMS values greater than μ_{RMS} are 11 in $x_1(t)$ and $x_4(t)$, respectively. In the next step,

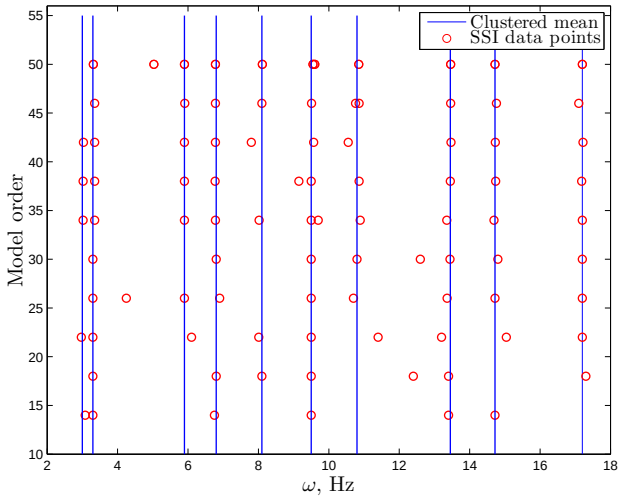

Figure 6.17: Stability diagram and modal frequency selection using SSI method

PCA is performed with the 11 SWPT coefficient pairs. A typical case of coefficient pairs and their Fourier spectra are shown in Fig. 6.19. For example, Fig. 6.19 shows the plots of $f_i^{5,0}(t)$ for $i = 1 - 4$. From the Fourier spectra, it can be observed that $f_i^{5,0}(t)$ is nearly mono-component. The principal directions and the variances of the major and minor PCs are shown in Fig. 6.19. The corresponding RCN value is 0.0008 for $f_i^{5,0}(t)$. Therefore, a low value of RCN ($\ll 1$) in $f_i^{5,0}(t)$ indicates a nearly mono-component signal, and hence it is an indicative of a structural mode. In fact, this is the first mode of the bridge with a modal frequency value of 3.0 hz. Using the principle direction, the slope of major principle axis is obtained as $m_1 = +1.47$, which is the first mode shape ordinate at this DOF respectively. If the number of desired target modes is N_t, then the coefficients with first N_t lowest RCN values can be selected as sources. In this example, $N_t = 10$ and thus the coefficients with first ten lowest RCN are selected as the sources. Fig. 6.20 and 6.21 show the identified sources using the SWPT-PCA method.

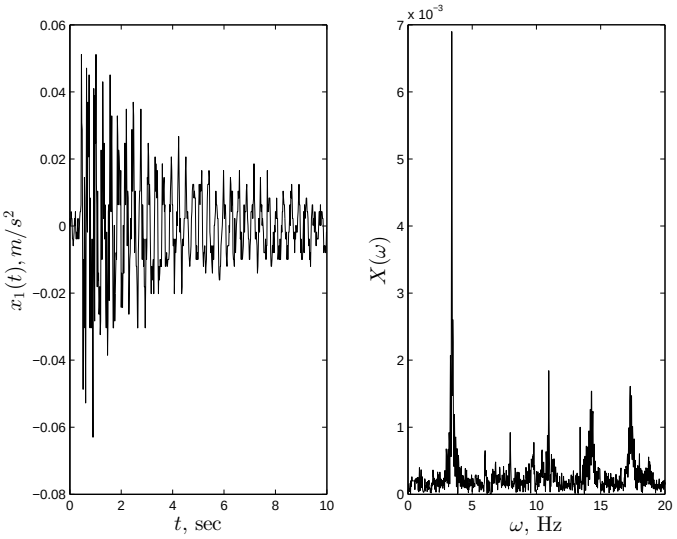

Figure 6.18: Typical free vibration data collected by wireless sensor and its Fourier transform

Presence of narrow-band excitation

Next, the suitability of sparse BSS method [118] in the presence of narrow-band excitation is pursued. For this purpose, a forced excitation was induced through continuous up-and-down jumps, for 60 seconds at the mid span of the bridge at each setup. Fig. 6.22 shows one typical forced vibration data. As shown in Fourier spectrum of the data, there is a presence of a frequency of 1.8 Hz which primarily occurred due to such forced vibration. The decentralized employing statistical characterization [118] is applied to delineate such excitation frequency from the structural frequency.

In order to identify the modal parameters from SWPT coefficients, the sample probability density of the selected SWPT coefficients of $x_1(t)$ and $x_4(t)$ are used. Fig. 6.23 shows the details of the identification using the information obtained form the PDF of $f_1^{5,v}$ and $f_4^{5,v}$. The first two columns of the Fig. 6.23 show the PDF of SWPT coefficients $f_i^{5,v}$ for $v = 0, 1$ and 8 for $i = 1$ and $i = 4$ respectively. The third column shows the Fourier spectra of the coefficients, where the cross-correlation (i.e., ρ) of the SWPT coefficients

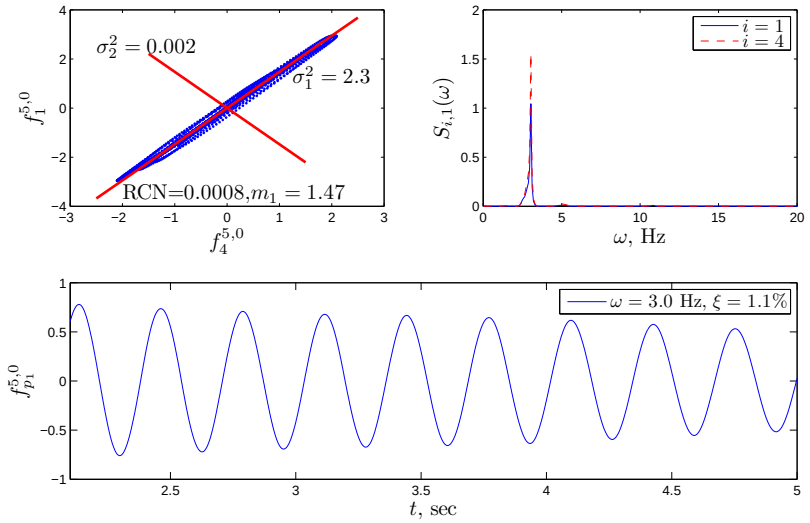

Figure 6.19: Identification results of S_1 using the SWPT-PCA method

and the resulting mode shape coefficients are reported. It can be seen that the PDF of $f_i^{5,v}$ with $v = 1$ and 8 have a value of κ close to 3.0, which corresponds to a system mode. The absolute value of cross-correlation $\rho_{1,4}$ for those coefficients is close to 1.0, implying a mono-component source, which can be considered as a modal response. The ratio of their standard deviations yields the mode shape coefficient and the sign of ρ determines the sign of the mode shape coefficients. In this fashion, the mixing coefficients can be estimated repeatedly using Eq. 4.17. For example, $f_1^{5,0}$ and $f_2^{5,0}$ have ρ value of +0.99 and standard deviation of 0.068 and 0.1, respectively, for which $\phi_{4,j}$ becomes $\frac{0.1}{0.068} = +1.47$. On the other hand, $f_1^{5,8}$ and $f_4^{5,8}$ have a ρ value of 1.0 and standard deviation of 0.03 and 0.026 respectively, for which $\phi_{4,j}$ is computed as $\frac{0.026}{0.03} = 0.86$. The PDF of $f_i^{8,0}$ has the value of $\kappa << 3.0$, which implies that the source is an excitation harmonic which is then discarded from further analysis. It can be seen that the coefficient $f_i^{8,0}$ accurately separates the excitation harmonic with a frequency of 1.8 Hz. The results are finally summarized for all coefficients containing the modal response in Table 6.8.

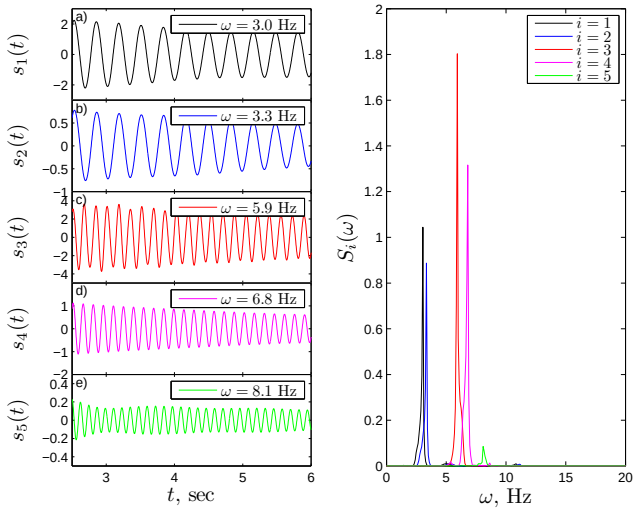

Figure 6.20: Identified sources ($s_1 - s_5$) using SWPT-PCA method

6.5 Summary

In this chapter, the proposed decentralized methods are validated using laboratory studies and full-scale examples. A full-scale validation was also undertaken on a pedestrian bridge located in Quebec, using wireless sensors. The accuracy of modal identification using the proposed decentralized algorithms favourably compare with those obtained from the centralized algorithms employing wired sensors.

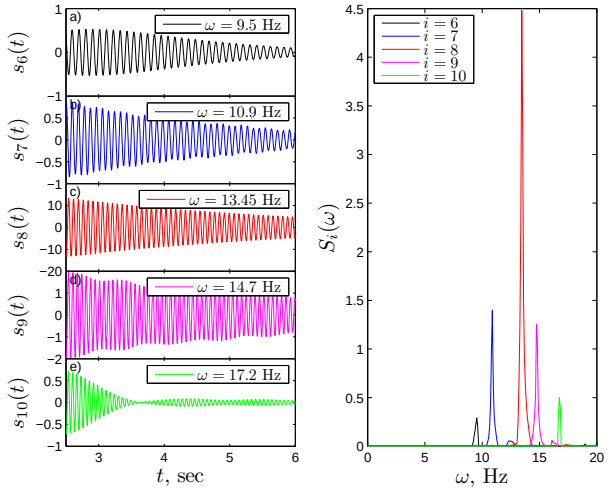

Figure 6.21: Identified sources ($s_6 - s_{10}$) using SWPT-PCA method

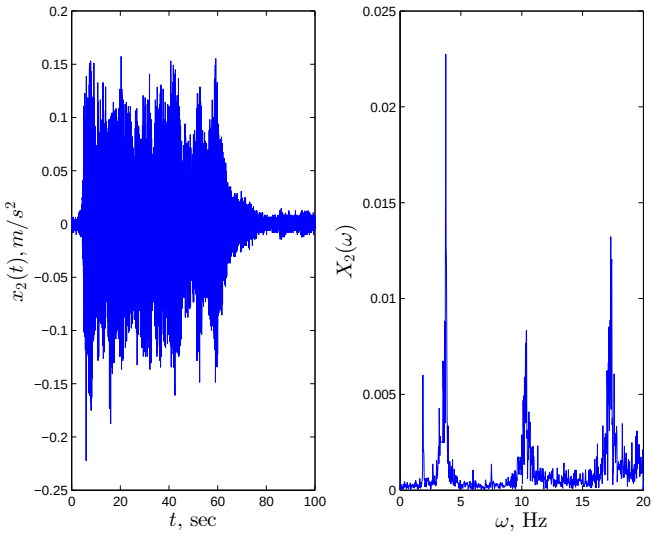

Figure 6.22: Forced vibration data (continuous ups-and-down jumping for 60 seconds) and its Fourier transform

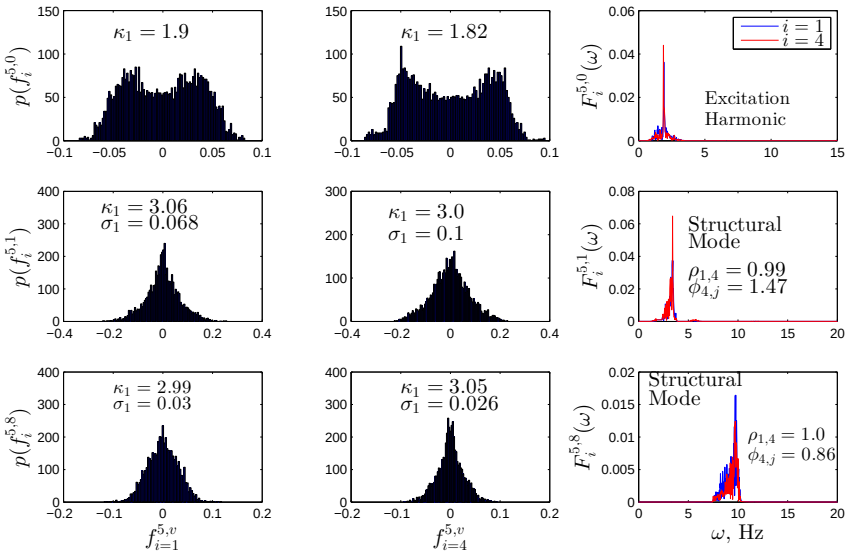

Figure 6.23: Identification results using sparse blind source separation under excitation harmonics

Table 6.8: Details of the identification results

Mode #	Centralized sensing system (using full (wired) measurements)				Decentralized sensing system (using partial (w/L) measurements)		
	SSI		SOBI		Sparse BSS		
	ω, Hz	ξ (%)	ω, Hz	ξ (%)	ω, Hz	ξ (%)	MAC
1	3.04	1.0	3.0	–	3.0	1.1	1.0
2	3.29	0.9	3.3	1.2	3.3	0.9	1.0
3	5.88	0.9	5.9	0.6	5.9	0.8	1.0
4	6.8	1.4	6.8	–	6.8	1.3	0.99
5	8.1	1.9	8.1	–	8.1	1.5	0.98
6	9.5	1.5	9.5	–	9.5	1.6	0.98
7	10.88	1.6	10.9	–	10.9	1.7	0.99
8	13.4	1.7	13.4	–	13.4	1.3	1.0
9	14.71	1.6	14.7	0.9	14.7	1.2	1.0
10	17.2	1.5	17.2	1.1	17.2	1.7	0.98

Chapter 7

Summary, conclusions and recommendations

7.1 Significant contributions

A suite of new sparse blind source separation algorithms have been developed in this thesis, with special emphasis on decentralized ambient modal identification and computationally efficient implementation. En-route, several milestones have been achieved. The key contributions of this research are briefly summarized as follows:

1. Novel decentralized algorithms to infer global structure mode information using measurements obtained using a small group of sensors at-a-time have been developed in this dissertation.

2. A new decentralized approach to deal with narrow band excitations was developed.

3. A novel methodology using PARAFAC decomposition was developed to make the algorithms computationally efficient.

4. The algorithms were demonstrated using both numerical and experimental studies, using both wired and wireless sensors.

5. Several peer-reviewed journal and conference articles (with some under review) have either directly resulted from this work, or have used many of the principles developed by the author in this thesis (see Appendix C).

7.2 Conclusions

Having highlighted the significant contributions of this dissertation, the central conclusions in this dissertation are summarized as follows:

1. A novel modal identification technique specifically suitable for decentralized processing is proposed. The main advantage of the proposed method is that only the data collected from a few sensors need to be processed at-a-time. The partial mixing coefficients so obtained in each step are dense in frequencies. There is no information feedback at each intermediate stage, which allows for relatively minimal user intervention and decentralized wireless implementation.

2. A decentralized ambient modal identification method that can satisfactorily delineate the modal sources when narrow band harmonics are present in the excitations was developed. The algorithm is based on the principle of sparse blind source separation using stationary wavelet packet transforms. In this method, prior information regarding the excitation harmonic frequency is not required, and is estimated along with the modal frequencies. The bootstrap approach allows the estimation of key statistics using limited measurements, which has potential in situations where repeating experiments is cumbersome. Due to the filter bank implementation of wavelet transforms, the proposed method is robust to measurement noise and other extraneous frequencies. Through numerical and experimental studies, it was shown that

the method works well when single or multiple harmonics are present, as long as the disturbance frequencies are well separated from the structural modes.

3. A novel decentralized ambient modal identification method is proposed that enhances the performance of sparse BSS using PARAFAC decomposition. In the proposed method, under-determined modal identification is solved within the framework of sparse BSS where the redundant stationary wavelet packet transform is employed to generate an over-complete dictionary of sparse bases. In order to reduce the computational effort, the tensor algebra tool, PARAFAC, is utilized, which allows us to use a higher scale level that that would be possible based on the fundamental frequency of interest and the sampling frequency. It is observed that the proposed PSBSS method successfully improves the upper bound of source separation of PARAFAC, and is relatively insensitive to the choice of sensor configuration, which makes it suitable for the decentralized modal identification. The proposed method is validated using a series of numerical simulations, followed by a full-scale study of the recorded measurements obtained from the UCLA factor building during an earthquake event. The results indicate that the proposed method is robust to noise, sensor configuration and requires significantly less computational overhead than in its native form, and hence has significant potential for ambient modal identification problems in decentralized applications for civil infrastructure.

4. The proposed decentralized methods are validated using a new wireless sensor module namely Lotus motes developed by Memsic. A full-scale validation is finally accomplished at a pedestrian bridge located in Montreal, Canada. The results show that the proposed algorithms are sufficiently robust and are capable of truly decentralized processing of measurements.

7.3 Recommendations for future work

There are several possible extensions of the current research to assess the performance of the decentralized modal identification in the domain of structural health monitoring.

1. During the course of current research, basic experimental framework for a new wireless sensor board, namely *Lotus*, was developed. Future work towards on-board processing (including embedded filter-bank implementation) and real-time decision making can be carried out within this framework. Various compressed sensing schemes that have thus far been tested in simple experiments can be extended within this framework for large applications. Finally, the basic ideas can be extended to online monitoring and diagnostic systems.

2. The proposed algorithm as derived in this dissertation is based on the assumption that the system has proportional damping. However this may not be valid for several practical situations such as soil-foundation-structure systems. Future studies could extend the decentralized modal identification to systems with non-proportional damping. Sparse blind source separation in conjunction with complex valued parallel factor decomposition can be employed in this regard.

3. Most of the BSS methods are attempted to perform modal identification for linear systems with no damage. Recently vibration based damage detection (VBDD), originating as an offshoot of structural health monitoring, has shown to be a powerful tool for damage diagnosis and prognosis, management and maintenance of modern civil infrastructure. Future research can be directed towards decentralized VBDD methods within the framework of wireless sensor networks. In this regard, both time and frequency domain sparsity of the response can be exploited to detect the damage signatures of the system.

4. In the current research, the primary objective was geared towards decentralized condition assessment of civil structures, e.g., buildings, towers and bridges. The basic concept of the proposed research can be further extended to machine health assessment, condition-based maintenance and to develop powerful fault diagnosis and prognosis tools.

APPENDICES

Appendix A

Second-order blind identification

The basic framework of second-order-blind-identification (SOBI) [13] is the simultaneous diagonalization of two covariance matrices $\mathbf{R_x}(0)$ and $\mathbf{R_x}(p)$ evaluated at the time-lag zero and p, respectively:

$$\begin{aligned} \mathbf{R_x}(0) &= E\left\{\mathbf{x}(n)\mathbf{x}^T(n)\right\} = \mathbf{A}\mathbf{R_s}(0)\mathbf{A}^T \\ \mathbf{R_x}(p) &= E\left\{\mathbf{x}(n)\mathbf{x}^T(n-p)\right\} = \mathbf{A}\mathbf{R_s}(p)\mathbf{A}^T \end{aligned} \tag{A.1}$$

where,

$$\mathbf{R_s}(p) = E\left\{\mathbf{s}(n)\mathbf{s}^T(n-p)\right\} \tag{A.2}$$

The following three steps set up the essence of SOBI: whitening, orthogonalization, and unitary transformation. Whitening is a linear transformation in which, $\mathbf{R_x}(0) = (1/N)(\sum_{n=1}^{N}\mathbf{x}(n)\mathbf{x}^T(n))$ is first diagonalized using singular value decomposition, $\mathbf{R_x}(0) = \mathbf{V_x}\mathbf{\Lambda_x}\mathbf{V_x}^T$ where $\mathbf{\Lambda_x}$ and $\mathbf{V_x}$ are the eigenvalues and eigenvectors of the co-variance matrix of $\mathbf{R_x}(0)$ respectively. Then, the standard whitening is realized by a linear transformation expressed as,

$$\bar{\mathbf{x}}(n) = \mathbf{Q}\mathbf{x}(n) = \mathbf{\Lambda_x}^{-\frac{1}{2}}\mathbf{V_x}^T\mathbf{x}(n) \tag{A.3}$$

Because of whitening, $\mathbf{R}_{\mathbf{x}}(p)$ becomes $\mathbf{R}_{\bar{\mathbf{x}}}(p)$, which is given by the equation,

$$\mathbf{R}_{\bar{\mathbf{x}}}(p) = (1/N)(\sum_{n=1}^{N} \bar{\mathbf{x}}(n)\bar{\mathbf{x}}^T(n-p)) = \mathbf{Q}\mathbf{R}_{\mathrm{x}}(p)\mathbf{Q}^T \tag{A.4}$$

Using the Eq. A.4 and Eq. A.1, we get

$$\mathbf{R}_{\bar{\mathbf{x}}}(p) = \mathbf{Q}\mathbf{A}\mathbf{R}_{\mathbf{s}}(p)\mathbf{A}^T\mathbf{Q}^T \tag{A.5}$$

The above equation states that by diagonalizing the whitened covariance matrix at a particular time-lag, the unitary matrix product $\mathbf{QA}$ can be determined, resulting in the mixing matrix, $\mathbf{A}$. This process of diagonalization is implemented numerically, and typically involves jointly diagonalizing several covariance matrices at a given lag p [47]. The second step, called orthogonalization, is applied to diagonalize the matrix $\mathbf{R}_{\bar{\mathbf{x}}}(p)$ whose eigen-value decomposition satisfies

$$\mathbf{V}_{\bar{\mathbf{x}}}\mathbf{R}_{\bar{\mathbf{x}}}(p)\mathbf{V}_{\bar{\mathbf{x}}}^T = \mathbf{\Lambda}_{\bar{\mathbf{x}}} \tag{A.6}$$

Since the diagonal matrix $\mathbf{\Lambda}_{\bar{\mathbf{x}}}$ has distinct eigen-values, it is easy to see that the product $\mathbf{QA}$ is a unitary matrix, and the mixing matrix can be estimated by the equation,

$$\hat{\mathbf{A}} = \mathbf{Q}^{-1}\mathbf{V}_{\bar{\mathbf{x}}} = \mathbf{V}_{\mathbf{x}}\mathbf{\Lambda}_{\mathbf{x}}^{1/2}\mathbf{V}_{\bar{\mathbf{x}}} \tag{A.7}$$

where $\hat{\mathbf{A}}$ is the estimated mixing matrix of $\mathbf{A}$. The problem now becomes one of unitary diagonalization of the correlation matrix $\mathbf{R}_{\bar{\mathbf{x}}}(p)$ at one or several non-zero time lags. The determination of the unitary matrix is carried out using a numerical procedure, commonly known as joint approximate diagonalization [13]. Denoting $\mathbf{V} = \mathbf{QA}$, $\mathbf{D} = \mathbf{V}^T\widetilde{\mathbf{R}}_{\bar{\mathbf{x}}}(p)\mathbf{V}$,

the problem is one of finding the minimum of the performance index J given by,

$$J(\mathbf{V},\mathbf{p}) = \sum_{p} \sum_{1 \le i \ne j \le n} \left| D_{ij}^{p} \right|^2 \tag{A.8}$$

Then, the unitary matrix $\mathbf{V}$ corresponding to minimum J over fixed h iterations is said to be an approximate joint diagonalizer [13]. Once $\hat{\mathbf{A}}$ is estimated, the sources $\hat{\mathbf{s}}$ can be estimated using the pseudo-inverse of Equation 3.3:

$$\hat{\mathbf{s}} = \hat{\mathbf{A}}^{-1}\mathbf{x} \tag{A.9}$$

Appendix B

Modified SOBI for modal identification under nonstationary excitation

The standard SOBI method operates under the assumption of stationary excitation, and therefore it is unable perform accurate modal identification when there is nonstationary excitation such as earthquake. The method described [112] here is applicable to the case when the the measurements and/or sources are second-order non-stationary, i.e., contain time-varying variances. In this method, unlike multiple non-overlapping windows used in MCC [44], the entire time sequence is successively trimmed by length s to construct several overlapping windows as shown in Fig. B.1. The covariance matrix for the p^{th} lag, for the k^{th} window (T_k), trimmed by length $(k-1)s$, is evaluated as [112]:

$$\hat{\mathbf{R}}_{\mathbf{x}}(T_k, p) = \frac{1}{(N - n_k)} \sum_{n=n_k+1}^{N} \mathbf{x}(n)\mathbf{x}^T(n-p) = \mathbf{A}\hat{\mathbf{R}}_{\mathbf{s}}(T_k, p)\mathbf{A}^T \tag{B.1}$$

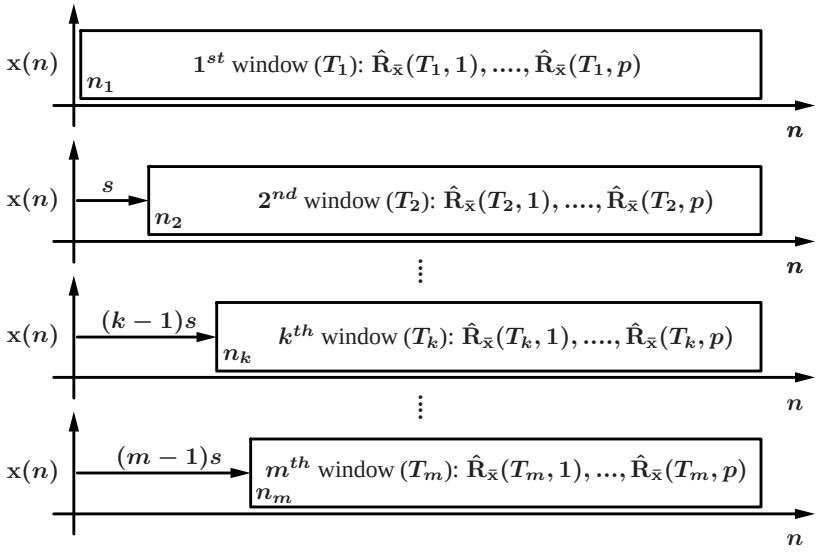

Figure B.1: Formation of multiple covariance matrices at a lag p

For a stationary signal, $\hat{\mathbf{R}}_{\mathbf{x}}(T_k,p)$ carry similar statistics regardless of T_k, whereas for a non-stationary signal, the statistics depends on T_k. Using a similar procedure as in Eq. A.3 and Eq. A.5, the whitened covariance matrix for T_k can be evaluated as:

$$\hat{\mathbf{R}}_{\bar{\mathbf{x}}}(T_k,p) \;=\; \mathbf{Q}\mathbf{A}\hat{\mathbf{R}}_{\mathbf{s}}(T_k,p)\mathbf{A}^T\mathbf{Q}^T \tag{B.2}$$

If the non-stationary sources are temporally correlated, then $\hat{\mathbf{R}}_{\mathbf{s}}(T_k,p)$ are nonsingular diagonal matrices [27]. The second step, called orthogonalization, is applied to diagonalize the matrix $\hat{\mathbf{R}}_{\bar{\mathbf{x}}}(T_k,p)$ and estimate the mixing matrix:

$$\hat{\mathbf{A}} = \mathbf{Q}^{-1}\mathbf{V}_{\bar{\mathbf{x}}} = \mathbf{V}_{\mathbf{x}}\mathbf{\Lambda}_{\mathbf{x}}^{1/2}\mathbf{V}_{\bar{\mathbf{x}}} \tag{B.3}$$

where $\hat{\mathbf{A}}$ is the estimated mixing matrix of $\mathbf{A}$. The problem now becomes one of unitary diagonalization of the correlation matrix $\hat{\mathbf{R}}_{\bar{\mathbf{x}}}(T_k,p)$ at one or several non-zero time lags. Eq. B.2 states that the whitened covariance matrix $\hat{\mathbf{R}}_{\bar{\mathbf{x}}}(T_k,p)$ at any non-zero time lag p is diagonalized by the unitary matrix $\mathbf{QA}$. The existence of the unitary matrix for any time

lag p is guaranteed by Eq. B.2, and the determination of the unitary matrix is carried out using a numerical procedure as explained next.

JAD for p time-lags for m windows

As seen in Eq. B.2, the problem of finding $\mathbf{A}$ is solved by unitarily diagonalizing $\hat{\mathbf{R}}_{\bar{\mathbf{x}}}(T_k, p)$. Due to estimation errors finding an exact diagonalizing unitary matrix may not be possible, and estimating $\mathbf{QA}$ is possible only in an approximate sense. Another issue is that the information of the proper choice of the lag parameter p is not available *a priori*. Hence, several values of time lags, $p = 1, 2, \cdots, l$ are chosen, and the matrices $\hat{\mathbf{R}}_{\bar{\mathbf{x}}}(T_k, p)$ are diagonalized for m trimmed windows. Based on the premise that the higher lags are more likely to contain new information for non-stationary sources [105], the covariance matrices with higher lags in each window are weighted higher using a parameter λ $(0 < \lambda \leq 1.0)$. This is accomplished by multiplying $\hat{\mathbf{R}}_{\bar{\mathbf{x}}}(T_k, p)$ with λ^{l-p} as shown below, where l is the maximum number of lags considered.

$$
\begin{aligned}
[\mathbf{M}]_{T_1} &= \left[\lambda^{l-1}\hat{\mathbf{R}}_{\bar{\mathbf{x}}}(T_1, p=1) \mid .... \mid \lambda^{l-i}\hat{\mathbf{R}}_{\bar{\mathbf{x}}}(T_1, p=i) \mid ... \mid \lambda^{0}\hat{\mathbf{R}}_{\bar{\mathbf{x}}}(T_1, p=l)\right] \qquad \text{(B.4)}\\
[\mathbf{M}]_{T_2} &= \left[\lambda^{l-1}\hat{\mathbf{R}}_{\bar{\mathbf{x}}}(T_2, p=1) \mid .... \mid \lambda^{l-i}\hat{\mathbf{R}}_{\bar{\mathbf{x}}}(T_2, p=i) \mid ... \mid \lambda^{0}\hat{\mathbf{R}}_{\bar{\mathbf{x}}}(T_2, p=l)\right]\\
\vdots[\mathbf{M}]_{T_k} &= \left[\lambda^{l-1}\hat{\mathbf{R}}_{\bar{\mathbf{x}}}(T_k, p=1) \mid .... \mid \lambda^{l-i}\hat{\mathbf{R}}_{\bar{\mathbf{x}}}(T_k, p=i) \mid ... \mid \lambda^{0}\hat{\mathbf{R}}_{\bar{\mathbf{x}}}(T_k, p=l)\right]\\
\vdots[\mathbf{M}]_{T_m} &= \left[\lambda^{l-1}\hat{\mathbf{R}}_{\bar{\mathbf{x}}}(T_m, p=1) \mid .... \mid \lambda^{l-i}\hat{\mathbf{R}}_{\bar{\mathbf{x}}}(T_m, p=i) \mid ... \mid \lambda^{0}\hat{\mathbf{R}}_{\bar{\mathbf{x}}}(T_m, p=l)\right]
\end{aligned}
$$

(B.5)

where, $[\mathbf{M}]_{T_k}$ represents a series of weighted multiple time-lagged covariance matrices stacked column-wise for the k^{th} window constructed by utilizing $N - (k-1)s$ data while trimming the first $(k-1)s$ data from total data length, N (as in Fig. B.1). The set of covariance matrices $[\mathbf{M}]_{T_1}$, $[\mathbf{M}]_{T_2}$, ..., $[\mathbf{M}]_{T_m}$ are stacked column-wise and jointly diago-

nalized as follows:

$$\left\langle \widetilde{\mathbf{R}}_{\bar{\mathbf{x}}} \right\rangle = \left\{ \underbrace{\begin{bmatrix} . & \cdots & \\ \vdots & \ddots & \\ & & \ddots \end{bmatrix}}_{[\mathbf{M}]_{T_1}} \underbrace{\begin{bmatrix} . & \cdots & \\ \vdots & \ddots & \\ & & \ddots \end{bmatrix}}_{[\mathbf{M}]_{T_2}} \cdots \underbrace{\begin{bmatrix} . & \cdots & \\ \vdots & \ddots & \\ & & \ddots \end{bmatrix}}_{[\mathbf{M}]_{T_k}} \cdots \underbrace{\begin{bmatrix} . & \cdots & \\ \vdots & \ddots & \\ & & \ddots \end{bmatrix}}_{[\mathbf{M}]_{T_m}} \right\}$$

Denoting $\mathbf{V} = \mathbf{QA},\ \mathbf{D} = \mathbf{V}^T \widetilde{\mathbf{R}}_{\bar{\mathbf{x}}}(T_k, p)\mathbf{V}$, the problem is one of finding the minimum of the performance index J given by,

$$J(\mathbf{V}) = \sum_{m=1}^{\frac{N}{s}} \sum_{p} \sum_{1 \le i \ne j \le n_s} |D_{ij}|^2 \tag{B.6}$$

Then, the unitary matrix $\mathbf{V}$ corresponding to minimum J over fixed h iterations is said to be an approximate joint diagonalizer [13].

Appendix C

List of publications

1. **Sadhu, A.**, and Narasimhan, S. (2013). "A decentralized blind source separation algorithm for ambient modal identification in presence of narrowband disturbances", *Journal of Structural Control and Health Monitoring*, Wiley, in press.

2. Tallavo, F., Cascante, G., **Sadhu, A.**, and Pandey, M. D. (2012). "New methodology for dynamic soil characterization using the free-decay response in resonant column testing", *Journal of Geotechnical and Geoenvironmental Engineering*, ASCE, accepted.

3. **Sadhu, A.**, Hazra, B., and Narasimhan, S. (2013). "Ambient modal identification of structures equipped with tuned mass dampers using parallel factor blind source separation", *Smart Structures and Systems*, Techno Press, accepted.

4. Kasra, G., **Sadhu, A.**, Walbridge, S., and Narasimhan, S. (2013). "Fatigue testing and structural health monitoring of retrofitted steel highway bridge web stiffeners", *Transportation Research Record*, Journal of Transportation Research Board.

5. **Sadhu, A.**, Hazra, B., and Narasimhan, S. (2012). "Blind identification of earthquake-excited structures", *Smart Materials and Structures*, IOPscience, 21(4).

6. Hazra, B., **Sadhu, A.**, Roffel, A. J., and Narasimhan, S. (2012). "Hybrid time-frequency blind source separation towards ambient system identification of structures", *Computer-aided Civil and Infrastructure Engineering*, Wiley, 27(5): 314–332.

7. Hazra, B., **Sadhu, A.**, Roffel, A. J., Paquet, P. E., and Narasimhan, S. (2012). "Underdetermined blind identification of structure by using the modified cross-correlation method", *Journal of Engineering Mechanics*, ASCE, 138(4): 327–337.

8. **Sadhu, A.**, Hazra, B., Narasimhan, S., and Pandey, M. D. (2011). "Decentralized modal identification using sparse blind source separation", *Smart Materials and Structures*, IOPscience, 20(12).

9. Hazra, B., **Sadhu, A.**, Lorenco, R., and Narasimhan, S. (2010). "Re-tuning tuned mass dampers using ambient vibration measurements", *Smart Materials and Structures*, IOPscience, 19(11).

10. **Sadhu, A.**, Hazra, B., and Narasimhan, S. (2012). "Decentralized modal identification of structures using parallel factor decomposition and sparse blind source separation", *Mechanical Systems and Signal Processing*, Elsevier, under revisions.

11. **Sadhu, A.**, Narasimhan, S., and Goldack, A. (2013). "Decentralized modal identification of pedestrian bridges using wireless sensor networks", *Journal of Bridge Engineering*, ASCE, under review.

12. **Sadhu, A.**, and Narasimhan, S. (2013). "Decentralized condition assessment of flexible bridges under pedestrian-induced narrowband disturbances". *Proceedings of Engineering Mechanics Institute Conference (ASCE)*, Evanston, USA, Aug 4–7.

13. Sychterz, A., **Sadhu, A.**, Narasimhan, S., and Walbridge, S. (2013). "Full-scale modal testing of the Daigneault creek bridge". *CSCE 2013 annual conference*, Montreal, QC, Canada, May 29 – Jun 1.

14. Kasra, G., **Sadhu, A.**, Walbridge, S., and Narasimhan, S. (2013). "Fatigue testing and structural health monitoring of retrofitted steel highway bridge web stiffeners", *The 92nd Annual Meeting of Transportation Research Board (TRB)*, Washington, USA, Jan 13–17.

15. **Sadhu, A.**, and Narasimhan, S. (2012). "Modern and cost-effective structural health assessment of civil infrastructure", *Alexander von Humboldt Colloquium*, Toronto, ON, Canada, Nov 2–4.

16. **Sadhu, A.**, and Narasimhan, S. (2012). "Sparse blind source separation: a powerful tool for ambient system identification of structures", *The 7th International Workshop on Advanced Smart Materials and Smart Structures Technology (ANCRiSST)*, IISC, India, Jul 27–28.

17. **Sadhu, A.**, Hu, B. and Narasimhan, S. (2012). "Blind source separation towards decentralized modal identification using compressive sampling", *Proceedings of 11th IEEE International Conference on Information Sciences, Signal Processing and their Applications (ISSPA)*, pp: 1147–1152, Montreal, QC, Canada, Jul 3–5.

18. **Sadhu, A.**, and Narasimhan, S. (2012). "Blind source separation of convolutive mixtures towards modal identification", *Proceedings of 30th International Modal Analysis Conference (IMAC)*, Jacksonville, FL, USA, Jan 30 – Feb 2.

19. **Sadhu, A.**, Hazra, B., and Narasimhan, S. (2011). "Decentralized modal identification using wavelet transform", *Proceedings of Engineering Mechanics Institute Conference (ASCE/ASME)*, Boston, USA, Jun 2–4.

20. Hazra, B., **Sadhu, A.**, and Narasimhan, S. (2010). "Re-tuning tuned mass dampers using ambient vibration measurements", *Proceedings of Engineering Mechanics Institute Conference (ASCE/ASME)*, Los Angeles, CA, USA, Aug 8–11.

Bibliography

[1] F. Abazarsa, S. F. Ghahari, F. Nateghi, and E. Taciroglu. Response-only modal identification of structures using limited sensors. *Structural Control and Health Monitoring*, page doi: 10.1002/stc.1513, 2012.

[2] F. Abrard and Y. Deville. A time-frequency blind signal separation method applicable to underdetermined mixtures of dependent sources. *Signal Processing*, 85:1389–1403, 2005.

[3] A. Aissa-El-Bey, N. Linh-Trung, K. Abed-Meraim, A. Belouchrani, and Y. Grenier. Underdetermined blind separation of non-disjoint sources in the time-frequency domain. *IEEE Transactions on Signal Processing*, 55(3):897–907, 2007.

[4] R.J. Allemang and D.L. Brown. A unified matrix polynomial approach to modal identification. *Journal of Sound and Vibration*, 211(3):301–322, 1998.

[5] P. Andersen, R. Brincker, and P. H. Kirkegaard. Theory of covariance equivalent armav models of civil engineering structures. *Proceeding of the 14th International Modal Analysis Conference*, 1996.

[6] P. Andersen, R. Brincker, C. Ventura, and R. Cantieni. Mode estimation of civil structures subject to ambient and harmonic excitation. *Proceeding of the 26th International Modal Analysis Conference (IMAC)*, 2008.

[7] J. Antoni. Blind separation of vibration components: Principles and demonstrations. *Mechanical Systems and Signal Processing*, 19:1166–1180, 2005.

[8] J. Antoni, L. Garibaldi, S. Marchesiello, and M. Sidhamed. New separation techniques for output-only modal analysis. *Shock and Vibration*, pages 227–242, 2004.

[9] J. C. Asmussen. *Modal analysis based on the random decrement technique - application to civil enginnering strcutures*. PhD Thesis, Alborg university, Denmark, 1997.

[10] S. K. Au, C. Papadimitriou, and J. L. Beck. Reliability of uncertain dynamical systems with multiple design points. *Structural Safety*, 21:113–133, 1999.

[11] H. Bachmann. Case studies of structures with man-induced vibrations. *ASCE, Journal of Structural Engineering*, 118:631–647, 1992.

[12] A. J. Bell and T. J. Sejnowski. An information-maximization approach to blind separation and blind deconvolution. *Neural Computation*, 7(6):1129–1159, 1995.

[13] A. Belouchrani, K. Abed-Meraim, J.F. Cardoso, and E. Moulines. A blind source separation technique using second-order statistics. *IEEE Transactions on signal processing*, 45(2):434–444, 1997.

[14] S. Bittanti and M. Lovera. Bootstrap-based estimates of uncertainty in subspace identification methods. *Automatica*, 36:1605–1615, 2000.

[15] P. Bofill and M. Zibulevsky. Underdetermined blind source separation using sparse representation. *Signal Processing*, 81:2353–2362, 2001.

[16] G. E. I Box, G. M. Jenkins, and G. C. Reinsel. *Time Series Analysis: Forecasting and Control*. John Wiely and Sons, Hoboken, New Jersey, 2008.

[17] R. Brincker, L. Zhang, and P. Anderson. Modal identification of output-only systems using frequency domain decomposition. *Smart Materials and Structures*, 10(3):441–445, 2001.

[18] R. Brincker, Lingmi. Zhang, and Palle. Anderson. Indicator for separation of structural and harmonic modes in output-only modal testing. *Proceeding of the 18th International Modal Analysis Conference*, 2000.

[19] Rune. Brincker, Carlos. E. Ventura, and Palle. Anderson. Damping estimation by frequency domain decomposition. In *Proceedings of SPIE, the International Society for Optical Engineering*, volume 4359, pages 698–703, 2001.

[20] R. Bro. Parafac. tutorial and applications. *Chemomemcs and Intelligent Laboratory Systems*, 38:149–171, 1997.

[21] J. M. W. Brownjohn. Ambient vibration studies for system identification of tall buildings. *Earthquake Engineering and Structural Dynamics*, 32(1):71–95, 2003.

[22] J. Caffrey, R. Govindan, E. Johnson, B. Krishnamachari, S. Masri, and G. Sukhatme. Networked sensing for structural health monitoring. In *Proceedings of 4th international workshop on structural control, New York, NY, June 10-11*, pages 57–66, 2004.

[23] J. M. Caicedo, S. J. Dyke, and E. A. Johnson. Natural excitation technique and eigensystem realization algorithm for phase i of the iasc-asce benchmark problem: Simulated data. *J. Engrg. Mech.*, 130(1):49–60, Jan 2004.

[24] J. D. Carroll and J. J. Chang. Analysis of individual differences in multidimensional scalling via an n-way generalization of eckart-young decomposition. *Psychometrika*, 35:283–319, 1970.

[25] S. H. Chao and C. H. Loh. Output-only dynamic system identification using blind source seperation technique. In *5th World Conference on Structural Control and Monitoring*, page CDROM, 12-14 July, 2010, Tokyo, Japan, 2010.

[26] S. Cho, C. B. Yun, J. P. Lynch, A. T. Zimmerman, Spencer Jr. B. F., and T. Nagayama. Smart wireless sensor technology for structural health monitoring of civil structures. *Steel Structures*, 8:267–275, 2008.

[27] S. Choi and A. Cichocki. Blind separation of nonstationary and temporally correlated sources from noisy mixtures. *IEEE Workshop on Neural Networks for Signal Processing (NNSP2000)*, pages 405–414, 2000.

[28] A. Cichocki and S. Amari. *Adaptive blind signal and image processing*. John Wiley and Sons, Ltd., Wiley (West Sussex), UK, 2003.

[29] R. R. Coifman and D. Donoho. Translation-invariant denoising. *Wavelet and Statistics*, pages 125–150, 1995.

[30] R. R. Coifman and M. V. Wickerhauser. Entropy-based algorithms for best basis selection. *IEEE Transaction of Information Theory*, 38(2):713–718, 1992.

[31] P. Comon. Independent component analysis: a new concept? *Signal Processing*, 36:287–314, 1994.

[32] C. Devriendt, G. D. Sitter, S. Vanlanduit, and P. Guillaume. Operational modal analysis in the presence of harmonic excitations by the use of transmissibility measurements. *Mechanical Systems and Signal Processing*, 23:621–635, 2009.

[33] D. L. Donoho and M. Elad. Maximal sparsity representation via l1 minimization. *Proc. Nat. Acad. Sci.*, 100:2197–2202, 2003.

[34] B. Efron and R. Tibshirani. *An Introduction to the Bootstrap*. Chapman and Hall, New York, 1993.

[35] J. E. Fowler. The redundant discrete Wavelet transform and additive noise. *Signal Processing Letters*, 12(9):629 – 632, September 2005.

[36] T. S. Fu, A. Ghosh, E. A. Johnson, and B. Krishnamachari. Energy-efficient deployment strategies in structural health monitoring using wireless sensor networks. *Struct. Control Health Monit.*, page doi: 10.1002/stc.1510, 2012.

[37] D. L. Fugal. *Conceptual Wavelets in Digital Signal Processing.* Space and Signal Technicals Publishing, San Diego, California, 2009.

[38] Y. Fujino, B. M. Pacheco, S. I. Nakamura, and P. Warnitchai. Synchronization of human walking observed during lateral vibration of a congested pedestrian bridge. *Earthquake Engineering and Structural Dynamics*, 22(9):741–758, 1993.

[39] Y. Gao, B. F. Spencer Jr, and M. Ruiz-Sandoval. Distributed computing strategy for structural health monitoring. *Structural control and health monitoring*, 13:488–507, 2006.

[40] R. Ghanem and F. Romeo. A wavelet based approach for the identification of linear time-varying dynamical systems. *Journal of Sound and Vibration*, 234(4):555–576, 2000.

[41] J. C. Goswami and A. K. Chan. *Fundamentals of Wavelets: Theory, Algorithms and Apllications.* John Wiley and Sons, Inc., 1999.

[42] P. Hall. *The Bootstrap and Edgeworth Expansion.* Springer-Verlag New York Inc., 1992.

[43] R. A. Harshman. Foundations of the parafac procedure: Models and conditions for an explanatory multi-model factor analysis. *UCLA working papers in Phonetics*, 16:1–84, 1970.

[44] B. Hazra and S. Narasimhan. Wavelet-based blind identification of the UCLA Factor building using ambient and earthquake responses. *Smart Materials and Structures*, 19(2):025005, 2010.

[45] B. Hazra, A. J. Roffel, S. Narasimhan, and M. D. Pandey. Modified cross-correlation method for the blind identification of structures. *Journal of Engineering Mechanics*, 136(7):889–897, 2010.

[46] B. Hazra, A. Sadhu, R. Lourenco, and S. Narasimhan. Retuning tuned mass dampers using ambient vibration response. *Smart Materials and Structures*, 19(11):115002, 2010.

[47] B. Hazra, A. Sadhu, A. J. Roffel, and S. Narasimhan. Hybrid time-frequency blind source separation towards ambient system identification of structures. *Computer Aided Civil and Infrastructure Engineering*, 27(5):314–332, 2012.

[48] B. Hazra, A. Sadhu, A. J. Roffel, P. E. Paquet, and S. Narasimhan. Underdetermined blind identification of structure by using the modified cross-correlation method. *Journal of Engineering Mechanics, ASCE*, 138(4), 2012.

[49] A. Hera and Z. Hou. Application of wavelet approach for asce structural health monitoring benchmark studies. *J. Engrg. Mech*, 130(1):96–104, 2004.

[50] N. E. Huang et al. The empirical mode decomposition for the Hilbert spectrum for nonlinear and non-stationary time series analysis. *Proceedings of Royal Society of London Series*, pages 903–95, 1998.

[51] M. V. Hulle. Clustering approach to square and non-square blind source separation. *In IEEE Workshop on Neural Networks for Signal Processing*, pages 315–323, 1999.

[52] Karhunen J. Hyvarinen, A. and E. Oja. *Independent Component Analysis*. John Wiley, New York, 2001.

[53] S.R. Ibrahim and E.C. Mikulcik. A time domain modal vibration test technique. *Shock and Vibration Bulletin*, 43(4):21–37, 1973.

[54] L. S. Igor, L. Pirmez, E. T. Lemos, F. C. Delicato, L. V. Pinto, N. Souza, and A. Y. Zomaya. A localized algorithm for structural health monitoring using wireless sensor networks. *Informaion Fusion*, page doi:10.1016/j.inffus.2012.02.002, 2012.

[55] E. T. Ingolfsson and C. T. Georgakis. A stochastic load model for pedestrian-induced lateral forces on footbridges. *Engineering Structures*, 33(12):34543470, 2011.

[56] G. P. Jaman. Implementation of a heterogeneous sensor network for structural health monitoring. *PhD Thesis*, 2007.

[57] G.H. James, T.G. Carne, and J.P. Lauffer. The natural excitation technique (NExT) for modal parameter extraction from operating structures. *Modal Analysis*, 10(4):260–277, 1995.

[58] H. Jo, S. H. Sim, T. Nagayama, and B. F. Spencer. Development and application of high-sensitivity wireless smart sensors for decentralized stochastic modal identification. *Journal of Engineering Mechanics, ASCE*, 136(6):683–694, 2012.

[59] I. T. Jollife. *Principal Component Analysis*. Springer, New York, 1986.

[60] A. Jourjine, S. Rickard, and O. Yilmaz. Blind separation of disjoint orthogonal signals: Demixing n sources from 2 mixtures. *Proc. ICASSP2000, June 5-9, 2000, Istanbul, Turkey*, 5:2985–2988, 2000.

[61] J.N. Juang and R.S. Pappa. An eigen system realization algorithm for modal parameter identification and model reduction. *Journal of Guidance, Control and Dynamics*, 8(5):620–627, 1985.

[62] G. Kerschen, F. Poncelet, and J.C.. Golinval. Physical interpretation of independent component analysis in structural dynamics. *Mechanical Systems and Signal Processing*, 21:1561–1575, 2007.

[63] T. Kijewski and A. Kareem. On the reliability of a class of system identification techniques: insights from bootstrap theory. *Structural Safety*, 24:261–280, 2002.

[64] T. Kijewski and A. Kareem. Wavelet transforms for system identification in civil engineering. *Computer-Aided Civil and Infrastructure Engineering*, 18(5):339–355, 2003.

[65] S. Kim and C. D. Yoo. Underdetermined blind source separation based on subspace representation. *IEEE Transactions on Signal Processing*, 57(7):2604–2614, 2009.

[66] P. Kisilev, M. Zibulevsky, and Y.Z.. Yehoshua. A multiscale framework for blind separation of linearly mixed signals. *Journal of Machine Learning Research*, 4:1339–1365, 2003.

[67] M. D. Kohler, M. P. Davis, and E. Safak. Earthquake and ambient vibration monitoring of the steel-frame UCLA Factor building. *Earthquake Spectra*, 21(3):1–22, 2005.

[68] J. B. Kruskal. Three-way arrays: rank and uniqueness of trilinear decompositions with applications to arithmatic compexity and statistics. *Linear Algebra and its application*, 18:95–138, 1977.

[69] J. Lardies and S. Gouttebroze. Identification of modal parameters using the wavelet transform. *International Journal of Mechanical Science*, 44:2263–2283, 2002.

[70] L. D. Lathauwer. Signal processing based on multilinear algebra. *Doctoral thesis, Catholic University, Leuven*, 1997.

[71] L. D. Lathauwer and J. Castaing. Blind identification of underdetermined mixtures by simultaneous matrix diagonalization. *IEEE Transactions on Signal Processing*, 56(3):1096–1105, 2008.

[72] F. Li, Li. Xiong, X. Liu, and X. Wu. Data transfer protocol in bridge structural health monitor system using wireless sensor network. *Proceedings of the 6th World Congress on Intelligent Control and Automation, June 21 - 23, 2006, Dalian, China*, pages 5102–5105, 2006.

[73] Y. Li, A. Cichocki, and S. Amari. Sparse component analysis for blind source seperation with less sensors than sources. *4th International Symposium on Independent Component Analysis and Blind Signal Separation (ICA2003)*, pages 89–94, 2003.

[74] C. C. Lin, J. F. Wang, and J.M. Ueng. Vibration control identification of seismically excited m.d.o.f. structure-ptmd systems. *Journal of Sound and Vibration*, 240(1):87–115, 2001.

[75] J. K. Lin, D. G. Grier, and J. D. Cowan. Feature extraction approach to blind source separation. *In IEEE Workshop on Neural Networks for Signal Processing (NNSP)*, pages 398–405, 1997.

[76] L. E. Linderman, K. A. Mechitov, and B. F. Spencer. Tinyos-based real-time wireless data acquisition framework for structural health monitoring and control. *Struct. Control Health Monit.*, page doi: 10.1002/stc.1514, 2012.

[77] K. C. Lu, Y. Wang, J. P. Lynch, P. Y. Lin, C. H. Loh, and K. H. Law. Application of wireless sensors for structural health monitoring and control. *The 18th KKCNN Symposium on Civil Engineering*, 2005.

[78] J. P. Lynch. An overview of wireless structural health monitoring for civil structures. *Philosophical Transcations of the Royal Society*, 365:345–372, 2007.

[79] J. P. Lynch, K. H. Law, E. G. Straser, A. S. Kiremidjian, and T. W. Kenny. The development of a wireless modular health monitoring system for civil structures. In *Proceeding of the MCEER Mitigation of earthquake Disaster by Advanced Tech. (MEDAT-2) Workshop*, Las Vegas, USA, Nov. 30, 2000.

[80] J. P. Lynch and K. Loh. A summary review of wireless sensors and sensor networks structural health monitoring. *Shock and Vibration Digest*, 38(2):91–128, 2006.

[81] J. P. Lynch, A. Sundararajan, K. H. Law, A. S. Kiremidjian, E. Carryer, H. Sohn, and C. R. Farrar. Field validation of a wireless structural monitoring system on the alamosa canyon bridge. In *SPIE's 10th Annual International Symposium on Smart Structures and Materials*, pages 267–278, San Diego, CA, USA, March 2-6, 2003.

[82] J. P. Lynch, A. Sundararajan, K. H. Law, and Carryer E. Kiremidjian, A. S. Embedding damage detection algorithms in a wireless sensing unit for operational power efficiency. *Smart Materials and Structures*, 13(4):800–810, 2004.

[83] F. Magalhaes, E. Caetano, and A. Cunha. Challenges in the application of stochastic modal identification methods to a cable-stayed bridge. *Journal of Bridge Engineering, ASCE*, 12(6):746–754, November 2007.

[84] N. M. M. Maia and J. M. M. Silva. *Theoretical and experimental modal analysis.* Research Studies Press, UK, 1997.

[85] S. G. Mallat. *A Wavelet tour of signal processing.* Academic Press, San Diego, 1998.

[86] Inc. Memsic. *Mote Processor Radio & Mote Interface Boards User Manual.* Memsic, CA, USA, 2010.

[87] Inc. Memsic. *Xmesh user manual.* Memsic, CA, USA, 2010.

[88] Inc. Memsic. *MTS/MDA Sensor Board Users Manual.* Memsic, CA, USA, 2012.

[89] Inc. Memsic. *Wireless sensor networks: LotusView+MoteConfig Preliminary user manual*. Memsic, CA, USA, 2012.

[90] S. V. Modak, C. Rawal, and T. K. Kundra. Harmonics elimination algorithm for operational modal analysis using random decrement technique. *Mechanical Systems and Signal Processing*, 24:922–944, 2010.

[91] P. Mohanty and D. J. Rixen. Modified sstd method to account for harmonic excitations during operational modal analysis. *Mechanism and Machine theory*, 39:1247–1255, 2004.

[92] P. Mohanty and D. J. Rixen. Operational modal analysis in the presence of harmonic excitation. *Journal of Sound and Vibration*, 270:93–109, 2004.

[93] T. Nagayama, S. H. Sim, Y. Miyamori, and B. F. Spencer, Jr. Issues in structural health monitoring employing smart sensors. *Smart Structures and Systems*, 3(3):299–320, 2007.

[94] K. K. Nair, A. S. Kiremidjian, and K. H. Law. Time series-based damage detection and localization algorithm with application to the asce benchmark structure. *Journal of Sound and Vibration*, 291:349–368, 2006.

[95] G.P. Nason and B.W. Silverman. The stationary Wavelet transform and some statistical applications. *Lecture Notes in Statistics*, Feb 1995.

[96] R. D. Nayeri, S. F. Masri, R.G. Ghanem, and R. L. Nigbor. A novel approach for the structural identification and monitoring of a full-scale 17-story building based on ambient vibration measurements. *Smart Materials and Structures*, 17(2):1–19, April 2008.

[97] D. E. Newland. *Introduction to random vibrations and spectral analysis*. Longman Group LTD., New York, 1975.

[98] D. E. Newland. Vibration of the london millennium bridge: cause and cure. *International Journal of accoustic vibration*, 8(1):9–14, 2003.

[99] Y. Nitta, T. Nagayama, B. F. Jr. Spencer, and A. Nishitani. Rapid damage assessment for the structures utilizing smart sensor mica2 mote. *Proceedings of 5th int. workshop on structural health monitoring*, pages 283–290, 2005.

[100] P. D. O'Grady, B. A. Pearlmutter, and S. T. Rickard. Survey of sparse and non-sparse methods in source separation. *International Journal of Imaging Systems and Technology, Special Issue: Blind Source Separation and Deconvolution in Imaging and Image Processing*, 15(1):18–33, 2005.

[101] L. Omlor and M. A. Giese. Anechoic blind source separation using wigner marginals. *Journal of Machine Learing Research*, 12:1111–1148, 2011.

[102] S. N. Pakzad, Kim S. Fenves, G. L., and D. E. Culler. Design and implementation of scalable wireless sensor network for structural monitoring. *ASCE Journal of infrastructure systems*, 14(1):89–101, 2008.

[103] S. M. Pandit and S. M. Wu. *Time Series and System Analysis with applications*. John Wiley and Sons, New York, 1983.

[104] C. Papadimitriou and G. Lombaert. The effect of prediction error correlation on optimal sensor placement in structural dynamics. *Mechanical Systems and Signal Processing*, 28:105–127, 2012.

[105] L. Parra and P. Sajda. Blind source separation via generalized eigenvalue decomposition. *J. Mach. Learn. Res*, 4:1261–1269, 2003.

[106] B. Peeters, B. Cornelis, K. Janssens, and H. V. Auweraer. Removing disturbing harmonics in operational modal analysis. *IOMAC, Copenhagen, Denmark*, 2007.

[107] J. C. Pesquet, H. Krim, and H. Carfantan. Time-invariant orthonormal wavelet representations. *IEEE Transactions in Signal Processing*, 44(8):1964 – 1970, 1996.

[108] R. Pintelon, B. Peeters, and P. Guillaume. Continuous-time operational modal analysis in the presence of harmonic disturbances. *Mechanical System and Signal Processing*, 22:1017–1035, 2008.

[109] F. Poncelet, G. Kerschen, J. C. Golinval, and D. Verhelst. Output-only modal analysis using blind source separation technique. *Mecahnical Systems and Signal Processing*, 21:2335–2358, 2007.

[110] C. Rainieri, G. Fabbrocino, G. Manfredi, and M. Dolce. Robust output-only modal identification and monitoring of buildings in the presence of dynamic interactions for rapid post-earthquake emergency management. *Engineering Structures*, 34:436–446, 2012.

[111] M.H. Richardson and D.L. Formenti. Parameter estimation from frequency response measurements using rational fraction polynomials. *Proceedings of 1st IMAC Conference, Orlando, Florida*, pages 1–15, 1982.

[112] A. Sadhu, B. Hazra, and S. Narasimhan. Blind identification of earthquake-excited structures. *Smart Materials and Structures*, 21(4):045019, 2012.

[113] A. Sadhu, B. Hazra, and S. Narasimhan. Ambient modal identification of structures equipped with tuned mass dampers using parallel factor blind source separation. *Smart Structures and Systems, accepted*, 2013.

[114] A. Sadhu, B. Hazra, and S. Narasimhan. Decentralized modal identification of structures using parallel factor decomposition and sparse blind source separation. *Mechanical Systems and Signal Processing, under revisions*, 2013.

[115] A. Sadhu, B. Hazra, S. Narasimhan, and M. D. Pandey. Decentralized modal identification using sparse blind source separation. *Smart Materials and Structures*, 20(12):125009, 2011.

[116] A. Sadhu, B. Hu, and S. Narasimhan. Blind source separation towards decentralized modal identification using compressive sampling. In *Proceedings of the* 11^{th} *International IEEE Conference on Information Science, Signal Processing and their Applications: Special Sessions, Montreal, Canada*, pages 1184–1189, DOI: 978-1-4673-0382-8-12, 2012.

[117] A. Sadhu and S. Narasimhan. Blind source separation of convolutive mixtures towards modal identification. In *Conference Proceedings of the Society for Experimental Mechanics Series, Volume 26*, pages 209–220, 2012.

[118] A. Sadhu and S. Narasimhan. A decentralized blind source separation algorithm for ambient modal identification in the presence of narrowband disturbances. *Structural Control and Health Monitoring*, page DOI: 10.1002/stc.1558, 2013.

[119] A. Sadhu, S. Narasimhan, and A. Goldack. Decentralized modal identification of a flexible pedestrian bridge using wireless sensors. *Journal of Bridge Engineering, under review*, 2013.

[120] C. Serviere and P. Fabry. Blind source separation of noisy harmonic signals for rotating machine diagnosis. *Journal of Sound and Vibration*, 272, 2004.

[121] S. H. Sim, J. F. Carbonell-Marquez, Spencer Jr. B. F., and H. Jo. Decentralized random decrement technique for efficient data aggregation and system identification in wireless smart sensor networks. *Probabilistic Engineering Mechanics*, 26:81–91, 2011.

[122] S. H. Sim, B. F. Spencer, M. Zhang, and H. Xie. Automated decentralized modal analysis using smart sensors. *Structural Control and Health Monitoring*, 17(8):872–894, 2009.

[123] D. Skolnik, Y. Lei, E. Yu, and J. Wallace. Identification, model updating, and response prediction of an instruemented 15-story steel-frame building. *Earthquake Spectra*, 22(3):781–802, 2006.

[124] A. Smilde, R. Bro, and P. Geladi. *Multi-way Analysis with Applications in the Chemical Sciences*. John Wiley and Sons, Ltd, West Sussex, UK, 2004.

[125] F. R. Spitznogle and A. H. Quazi. Representation and analysis of time-limited signals using a complex exponential algorithm. *J. Acoust. Soc. Am.*, 47:1150–1155, 1970.

[126] J. Starck, F. Murtagh, and J. M. Fadili. *Sparse Image and Signal Processing: Wavelet, Curvelets, Morphological Diversity*. Cambridge University Press, New York, USA, 2010.

[127] W. J. Staszewski. Identification of damping in mdof systems using time-scale decomposition. *Journal of Sound and Vibration*, 203(2):283–305, 1997.

[128] W. J. Staszewski and A. N. Robertson. Time-frequency and time-scale analyses for structural heal monitoring. *Philosophical Transction of The Royal Society*, 365:449–477, 2007.

[129] A. Stegeman, T. Berge, and D. Lathauwer. Sufficient conditions for uniqueness in candecomp/parafac and indscal with random component matrices. *Psychometrika*, 71(2):219–229, 2006.

[130] E. G. Straser and A. S. Kiremidjian. A modular, wirless damage monitoring system for structures. *Report No. 128, John A Blume Earthquake Engineering Center, Department of Civil and Environmental Engineering*, 1998.

[131] Z. Sun and C. C. Chang. Structural damage assessment based on wavelet packet transform. *J. of Struc. Eng.*, 128(10):1354–1361, 2002.

[132] B. Sundararaman, U. Buy, and A. D. Kshemkalyani. Clock synchronization for wireless sensor networks: A survey. *Ad Hoc Networks*, 3:281–323, 2005.

[133] R.A. Swartz, D. Jung, J.P. Lynch, Y. Wang, and M Flynn. Design of a wireless sensor for scalable distributed in-network computation in a structural health monitoring system. *Proc. Int. Workshop on Structural Health Monitoring*, 2005.

[134] A. Sychterz, A. Sadhu, S. Narasimhan, and S. Walbridge. Results from modal testing of the daigneault creek bridge. In *CSCE general conference*, Montreal, Quebec, 2013.

[135] F. Tallavo, G. Cascante, A. Sadhu, and M. D. Pandey. New methodology for dynamic soil characterization using the free-decay response in resonant column testing. *Journal of Geotechnical and Geoenvironmental Engineering*, page press, 2013.

[136] N. A. Tanner, J. R. Wait, C. R. Farrar, and H. Sohn. Structural health monitoring using modular wireless sensors. *Journal of Intelligent Material Systems and Structures*, 14:43–56, 2003.

[137] TinyOS. *version 1.1.15*. Available from: http://www.tinyos.net., 2005.

[138] G. Tomasi and R. Bro. A comparison of algorithms for fitting the parafac model. *Computational Statistics & Data Analysis*, 50:1700–1734, 2006.

[139] P. VanOverschee and B. De Moor. N4sid: numerical algorithms for state space subspace system identification. *Proceedings of the IFAC World Congress*, pages 361–364, 1993.

[140] P. VanOverschee and B. De Moor. *Subspace identification for linear systems: Theory, Implementation, Applications*. Dordrecht, Netherlands, 1996.

[141] Y. Wang, J. P. Lynch, and K. H. Law. A wireless structural health monitoring system with multithreaded sensing devices: design and validation. *Structure and Infrastructure Engineering*, 3(2):103–120, 2007.

[142] M.V. Wickerhauser. *Adapted Wavelet Analysis from Theory to Software*. A. K. Peters, Ltd., Wellesley, Massachusetts, 1994.

[143] J. Wu, S. Yuan, X. Zhao, Y. Yin, and W. Ye. A wireless sensor network node designed for exploring a structural health monitoring application. *Smart Materials and Structures*, 16:1898–1906, 2007.

[144] Z. Wu and N. E. Huang. Ensemble empirical mode decomposition: A noise assisted data analysis method. *Technical Report 193*, pages 1898–1906, 2005.

[145] Y. J. Yan, L. Cheng, Z. Y. Wu, and L. H. Yam. Wavelet transform-based modal parameter identification considering uncertainty. *Journal of Sound and Vibration*, 291:285–301, 2006.

[146] J. N. Yang, Y. Lei, S. Lin, and N. Huang. Identification of natural frequencies and dampings of in-situ tall buildings using ambient wind vibration data. *Journal of Engineering Mechanics*, 130(5):570–577, 2004.

[147] J. N. Yang, Y. Lei, S. Pan, and N. Huang. System identification of linear structures based on Hilbert Huang spectral analysis. part 1: normal modes. *Earthquake Engng Struct. Dyn.*, 32(9):1443–1467, 2003.

[148] Y. Yang and S. Nagarajaiah. Blind identification of damage in time-varying system using independent component analysis with wavelet transform. *Mechanical Systems and Signal Processing*, page doi: 10.1016/j.ymssp.2012.08.029, 2012.

[149] Y. Yang and S. Nagarajaiah. Time-frequency blind source separation using independent component analysis for output-only modal identification of highly-damped

structures. *Journal of Structural Engineering*, pages doi: 10.1061/(ASCE)ST.1943–541X.0000621, 2012.

[150] O. Yilmaz and S. Rickard. Blind separation of speech mixtures via time-frequency masking. *IEEE Transactions on Signal Processing*, 52(7):1830–1847, 2004.

[151] S. Yuan, X. Lai, X. Zhao, X. Xu, and L. Zhang. Distributed structural health monitoring system based on smart wireless sensor and multi-agent technology. *Smart Materials and Structures*, 15:1–8, 2006.

[152] S. Yuan, D. Liang, L. Shi, X. Zhao, J. Wu, G. Li, and L. Qiu. Recent progress on distributed structural health monitoring research at nuaa. *Journal of Intelligent Material Systems and Structures*, 19:373–386, March 2008.

[153] L. Zhang, H. Kanda, L. Brown, D, and J. Allemang, R. Frequency domain poly reference method for modal analysis. *Journal of Applied Mechanics, ASME*, 106(85), 1985.

[154] Li. Zhang, C. H. He, and P. Wang. Harmonic elimination using independent component analysis. *Automation Congress, WAC 2008. World*, pages 1–4, 2008.

[155] Wanliang. Zhou and David. Chelidze. Blind source separation based vibration mode identification. *Mechanical Systems and Signal Processing*, 21:3072–3087, 2007.

[156] D. Zhu, X. Yi, Y. Wang, K. Lee, and J. Guo. A mobile sensing system for structural health montoring: design and validation. *Smart Materials and Structures*, 19, 2010.

[157] M. Zibulevsky, P. Kisilev, Y. Y. Zeevi, and B. A. Pearlmutter. Blind source separation via multinode sparse representation. *In Advances in Neural Information Processing Systems*, 14:1049–1056, 2002.

[158] M. Zibulevsky and B.A. Pearlmutter. Blind source separation by sparse decomposition. *Neural Computations*, 13(4):863–883, 2001.

[159] A. T. Zimmerman and J. P. Lynch. A parallel simulated annealing architecture for model updating in wireless sensor networks. *IEEE sensors journal*, 9(11):1503–1510, 2009.

[160] A. T. Zimmerman, M. Shiraishi, R. A. Swartz, and J. P. Lynch. Automated modal parameter estimation by parallel processing within wireless monitoring systems. *Journal of Infrastructure System*, 22:102–113, 2008.

[161] A. M. Zoubir and D. R. Iskander. *Bootstrap Techniques for Signal Processing*. Cambridge University Press, Cambridge, UK, 2004.